Master thesis and internship[BR]- Master's thesis : Plasma sheath modeling with a high order Discontinuous Galerkin Method[BR]- Integration internship

Auteur : Custinne, François
Promoteur(s) : Hillewaert, Koen
Faculté : Faculté des Sciences appliquées
Diplôme : Master en ingénieur civil en aérospatiale, à finalité spécialisée en "aerospace engineering"
Année académique : 2020-2021
URI/URL : http://hdl.handle.net/2268.2/13123

Plasma sheath modeling with a high order Discontinuous Galerkin Method

Master's thesis carried out to obtain the degree of Master of Science in Aerospace Engineering

François Custinne 20150710

University of Liège - School of Engineering and Computer Science

Academical year
2020 - 2021

Acknowledgements

Tout d'abord, j'aimerais remercier ma famille, en commençant par mes parents qui m'ont soutenu durant toute la durée de mes études ainsi que ma petite amie, Wendy, qui m'a soutenu (et supporté) durant toute la durée de ce projet.

J'aimerais aussi remercier toute l'équipe DG de l'université de Liège qui m'a accueilli comme un membre a part entière de leur équipe. Je les rermercie pour leur patience et leur disponibilité. Un merci tout particulier est addressé à Giuseppe Gangemi, Nayan Levaux et Amaury Bilocq.

Enfin, je remercie tout particulirèment mes promoteurs Koen Hilleweart et Thierry Magin qui ont su m'aiguiller efficacement durant toute la durée de ce projet. Je les remercie aussi pour leur bienveillance et leur disponibilité à toute épreuve.

First, I would like to thank my family, starting from my parents whose support was constant during the whole duration of my education. As well as my girlfriend, Wendy, whose daily support and encourangement helps me to achieve this project.

I would also tank the whole DG team of the university of Liege who has welcomed me has part of their members. I thank them for their patience and their disponibility. A special thanks is addressed to Giuseppe Gangemi, Nayan Levaux and Amaury Bilocq.

Finally, I would thank particularly my two supervisors, Koen Hillewaert and Thierry Magin whose sharp advices permits me to propose this work. I thank them for their kindness and their unfailing availability.

Contents

Introduction

Since the beginning of the 20th century, research in low-temperature plasmas has grown into a major field of plasma science. In particular, confined plasmas are of great interest for a large range of technological applications: from domestic with lightning and plasma displays panels (PDPs) [7], to electric space propulsion [34, 45] (*e.g.* the Hall thruster in Fig. 1) and, more recently, medicine [51]. This vast domain of application gives rise to many numerical models whose specificities are adapted to current needs. From the literature, two main approaches are used: the first one is the kinetic approach, also referred as particle methods, which consist of describing the plasma at the level of the particle. This means that the motion of every particle is tracked at each time. Another approach are the fluid models that describe the average motion of the particles and are based on the resolution of velocity-moment of the Boltzmann equation. The former is the most fundamental approach with very accurate results, but has a very high numerical cost. In opposition, the latter is less precise but exhibits more reasonable computational time. Hybrid models combining the fluid and the kinetic description have also shown cheaper alternatives for low-temperature plasma modelling [46, 37].

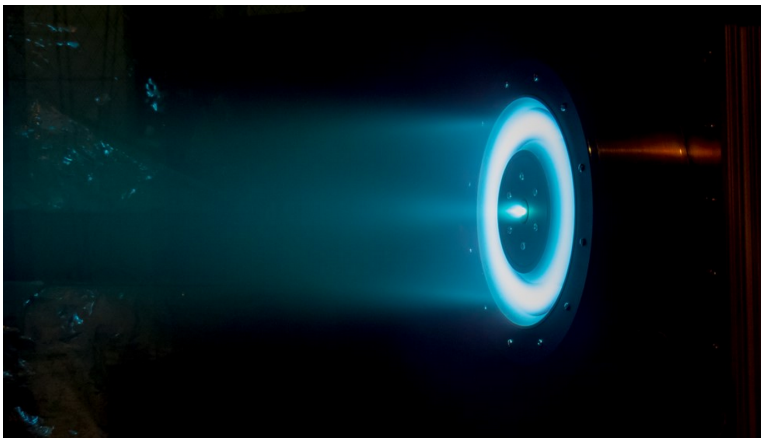

Fig. 1: H9 Hall thruster (*Credit:* Univeristy of Michigan, USA)[1]

The main difficulties in plasma modelling is the very large mass disparity between electrons and the other species that compose the ionised gas. This intrinsic multiscale property makes the numerical problem very stiff. On the other hand, this mass ratio plays a fundamental role in the plasma behaviour. In particular, in low collisional plasma in which it leads to a large disparity in the motions of electrons and ions. The latter

conducts to many physical phenomena such as: the two stream instabilities, the plasma sheath or the electron drift instability appearing in magnetised plasma.

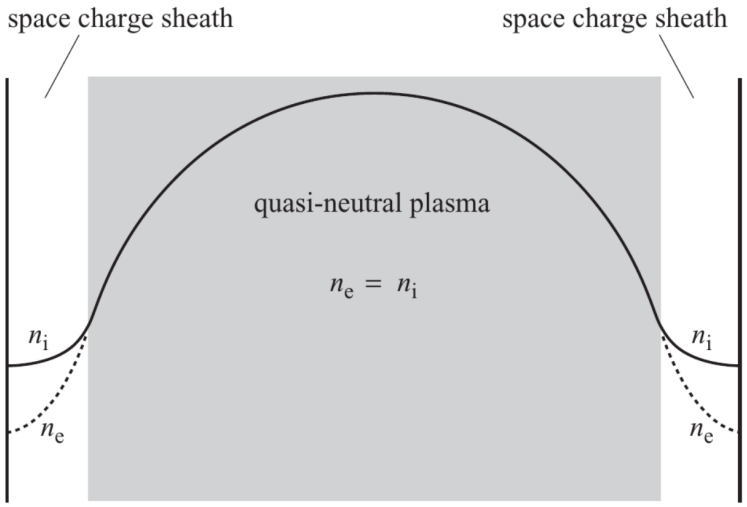

Fig. 2: Schematics of a typical discharge in which the sheath appear [14]

This project aims to simulate and study two of these common features: the first one being the two-stream instabilities of a quasi-neutral mixture in a periodic domain. The second one is the plasma sheath, a charge boundary layer in the vicinity of the walls in which charge neutrality does not apply, as shown in Fig. 2. In both configurations, disparate temporal and spatial scales are encountered, justifying the use of highly accurate numerical algorithm to capture the multiple scales.

In this work, the numerical simulation of a two-fluid low-temperature plasma with the use of Discontinuous Galerkin finite element Methods (DG-FEM) is presented. For this purpose, the coupled resolution of the electrons and ions transports equations with a Poisson's equation for the electrical potential is carried out through a fully-implicit strategy. This choice permits to overcome the strict stability constraints coming from the electrons/ions mass disparity that affect explicit schemes.

Within the current state-of-the art, numerous numerical methods have been proposed to simulate the two-fluid equations [48, 47, 69, 68, 27, 26, 25, 56]. In particular, specific methods have been developed to face the main difficulties that arise in plasma modelling. First, one may quote *Asymptotic Preserving* (AP) schemes [25, 29, 28], with the recent breakthrough proposed by Alvarez Laguna *et al.*[2], which preserve the quasi-neutral asymptotic limit without any need on the resolution of the intrinsic multiscale definition of low temperature plasma [44]. In parallel to that, the very low mass ratio involved between the electron and the other species yields in a very low Mach regime for the electron. To face that, AUSM$^+$-up method [48, 47] has been proposed as an alternative to classical preconditions methods [70]. Finally, it has been shown that the low temperature conditions introduce unsimilar difficulties in the management of the source terms which

can be dominant (w.r.t the pressure terms). A proposed solution is the use of well balanced schemes [53, 6].

Throughout this description, only a few have been performed using DG-FEM [68, 69, 56], and even less address fully coupled solving of the Euler-Poisson system of equations. This work with its fully coupled resolution continues the one started by N. Corthouts [24] during his M.Sc thesis In this writing, he intended to solve only the particles equations and has derived an approximate expression for the potential.

This work is organised in three parts: one dealing with the plasma physics, one for the numerical methods and one presenting the results. In the first part, a brief description of the plasma physics is provided, the multi-fluid model is then derived and from the Boltzmann's equation. The transport equations associated to electrons and ions are obtained as well as the Poisson's equation for the electrical potential. The application to the current two-fluid configuration is presented with the definition of the different problems cover here. The structure of the two-fluid equation is studied to highlight the characteristics.

In the second part, the DG-FEM is described and applied to the current configuration. The strategy used to couple the diffusive and convective part of the problem is also presented. The time integration using a fourth-order six-stages Explicit first stage, Single Diagonally Implicit Runge-Kutta (ESDIRK) is then described with special consideration made to the potential coupling and the ionisation contribution.

The last part corresponds to the presentation of the obtained results. First, a preliminary work done onto the unidimensional Burgers equation is done presenting common features of nonlinear schemes. Then, the results obtained for a two-stream periodic perturbation configuration are presented. A comparison of the results obtained with explicit and fully implicit time integrator is made. Finally, the results obtained for a plasma confined in a cylinder with equipotential walls is presented and compared to state of the art solution, as the one proposed by Alvarez Laguna *et al.* [2].

Part I

Plasma physics

Chapter 1

Plasma physics and multi-fluid model

This chapter presents the physics associated to low-temperature plasma. Its common features such as the electrons/ions mass disparity, the sheath formation and the Debye length are introduced here. From that, the multi-fluid model is derived from the statistical description made in the Boltzmann's equation to the fluid electrons/ions transport equations. These last are closed using a Poisson equation for the potential.

1.1 Physics of plasma

The behaviour of plasmas and its interaction with walls are well described by Chabert & Braithwaite [14]. This section briefly introduce their main features. Let us consider a plasma mixture composed of only single-charged particles of ions and electrons in a background gas of neutral particles at rest of density much larger than those of the charged species. The latter induces a weakly ionised plasma. The thermal velocity of these charged particles are expressed as follow:

$$v_{th,e} = \sqrt{\frac{\mathrm{k_B} T_e}{m_e}} \quad \text{and} \quad v_{th,i} = \sqrt{\frac{\mathrm{k_B} T_i}{m_i}} \tag{1.1}$$

where $v_{th,\alpha}$ is the mean velocity of the particle α, T_α is its temperature, m_α is its mass and $\mathrm{k_B}$ is the Boltzmann constant. Because of the huge mass disparity between the ions and electrons, *i.e.* $m_i \gg m_e$, one has

$$|v_{th,e}| \gg |v_{th,i}| \tag{1.2}$$

This means that electrons have much more mobility than ions. One the one hand, this huge disparity lead mainly to numerical models that are very stiff to resolved. On the other hand, it introduces particular features in the case of bounded plasma, *e.g.* the sheath problem.

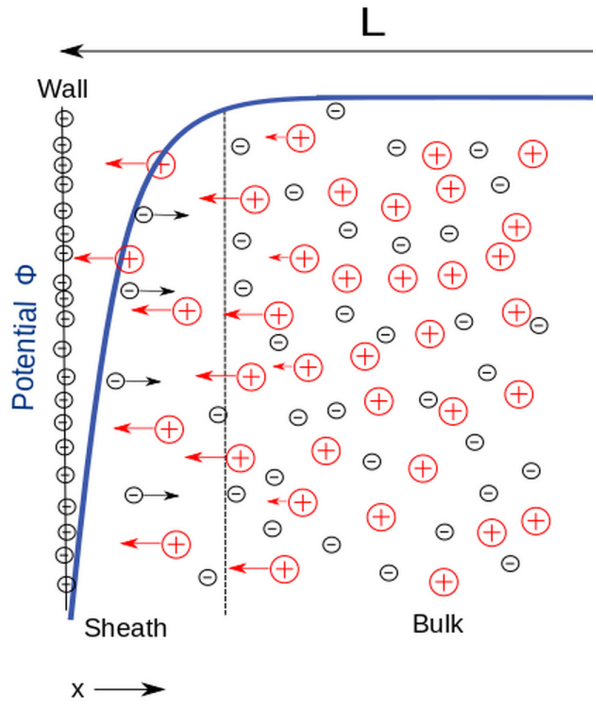

Fig. 2: Schematics of the formation of the scheath

Let us introduce the features attached to this sheath and consider a plasma binary mixture confined in an tank with equipotential walls (or floating walls) and a unidimensional problem. A more detailed description of the sheath problem used for this work is presented in section 2.3. At the beginning of the experiment, the tank is composed of a quasi-neutral mixture of electrons and ions. This means that they have comparable number densities, *i.e.* $n_e \sim n_i$. The presence of the floating walls then induces a mean flux of electrons $\Gamma_e = n_e v_{th,e}$ and ions $\Gamma_i = n_i v_{th,i}$ at the boundaries. Because of Eq. (1.2), one has

$$|\Gamma_e| \gg |\Gamma_i| \tag{1.3}$$

and so an higher number of electrons impacts the boundary charging it negatively. This process hence creates a negative charge region close to the wall called the *sheath* in which the quasi-neutrality is no more respected. A schematics of this sheath formation is available in Fig. 2.

This region extends over several λ_D from the walls with λ_D called the *Debye length*:

$$\lambda_D = \sqrt{\frac{\epsilon_0 \mathrm{k_B} T_e}{n_0 e^2}} \tag{1.4}$$

with ϵ_0 being the dielectric permittivity of the vacuum, T_e the electron temperature and n_0 the reference number density (usually associated to the initial electron number density, *i.e.* $n_0 \sim n_{e0}$). This parameter plays a key role in the size of the sheath as it quantifies the distance over which significant charge separation occurs. Values around $\lambda_D \sim 10^{-4}$m yields huge constraints onto the spatial resolution of the problem near the walls. The Debye length can also be expressed as the ratio between the electron thermal velocity

$v_{th,e}$ and the electron plasma frequency ω_{p_e}

$$\lambda_D = \frac{v_{th,e}}{\omega_{p_e}} \tag{1.5}$$

where the latter also plays an important role in the numerical stability of the problem. This last phenomenon is explained in more detailed in section 5.1.

Now that physics of the sheath is well defined, their governing equations can be discussed. These are developed in the following sections.

1.2 Boltzmann's Equation

As introduced in the previous sections, a plasma is a mixture of charged particles. Because of the huge number of particle involved (*e.g.* $n_0 \sim 10^{16}$ m^3 for a typical gas discharge [14]), a statistical approach is preferred. The evolution of the plasma system is thereby described by the mean of a distribution function $f_\alpha(\boldsymbol{x}, \boldsymbol{v}, t)$ (a positive function in the six-dimensional phase space $(\boldsymbol{x}, \boldsymbol{v})$) for the particle α. The evolution of f_α is governed by the Boltzmann's equation [17]:

$$\frac{\partial f_\alpha}{\partial t} + \boldsymbol{v}\partial_{\boldsymbol{x}} f_\alpha + \partial_{\boldsymbol{v}} \left(\frac{\mathbf{F}_\alpha}{m_\alpha} f_\alpha \right) = C_\alpha + I_\alpha \tag{1.6}$$

where $\mathbf{F}_\alpha(\boldsymbol{x}, t)$ is the total exerted force on a particle α at a position $\boldsymbol{x}$ and m_α is the particle mass. $\partial_{\boldsymbol{x}}$ and $\partial_{\boldsymbol{v}}$ denote respectively the divergence operators with respect to the position and velocity of the particle. For a particle carrying a charge e, subjected to a local electric field $\mathbf{E}$ and in the absence of any magnetic field $\mathbf{B}$, the force term $\mathbf{F}_\alpha = e\left[\mathbf{E} + \boldsymbol{v} \times \mathbf{B}\right]$ reduces to

$$\mathbf{F}_\alpha = e\mathbf{E} \tag{1.7}$$

The right hand side of Eq. (1.6) takes into account the effect of particle interactions denoted by the elastic collision between the particles C_α and the particles ionisation I_α. In the present work, the effect of these elastic particle collisions is assumed to be negligible compared to the ionisation one. Boltzmann's equation for collisionless plasma becomes

$$\frac{\partial f_\alpha}{\partial t} + \boldsymbol{v} \cdot \nabla_{\boldsymbol{x}} f_\alpha + \frac{e\mathbf{E}}{m_\alpha} \cdot \nabla_{\boldsymbol{v}} f_\alpha = I_\alpha \tag{1.8}$$

This last equation will be the base of the plasma fluid description presented in the next section.

1.3 Multi-fluid model

The Multi-fluid description of the plasma is derived from the Boltzmann's equation (1.8). Before diving into the derivation of the multi-fluid transport equations, let's make some assumptions:

- The plasma mixture is assumed to be isothermal, meaning that their temperatures remain constant, *i.e.* $T_\alpha(\boldsymbol{x}, t) = T_\alpha$;
- Isotropic plasma and constant particle masses, *i.e.* $m_\alpha(t) = m_\alpha$, are also considered;
- The right hand side of Eq. 1.8 accounting to ionisation processes is neglected to facilitate the derivation. This will be taken into account at the end of the development.

The Multi-fluid model is then obtained following the methodology of Braginskii [11]. It introduces first the number density

$$n_\alpha(\boldsymbol{x}, t) = \int_3 f_\alpha(\boldsymbol{x}, \boldsymbol{v}, t) d\boldsymbol{v} \tag{1.9}$$

and the mean velocity

$$\boldsymbol{V}_\alpha(\boldsymbol{x}, t) = \langle \boldsymbol{v}_\alpha(\boldsymbol{x}, t) \rangle = \frac{1}{n_\alpha} \int_3 \boldsymbol{v}\, f_\alpha(\boldsymbol{x}, \boldsymbol{v}, t) d\boldsymbol{v}. \tag{1.10}$$

These are two macroscopic quantities determined from the first two moments of the particle distribution function f_α. The density and momentum transport equations are then obtained respectively from the zeroth and first velocity moments of the Boltzmann's equation (1.8), they are[1]

$$\begin{aligned} \partial_t n_\alpha + \partial_{\boldsymbol{x}} \left(n_\alpha \boldsymbol{V} \right) &= 0 \\ \partial_t \left(m_\alpha n_\alpha \boldsymbol{V}_\alpha \right) + \partial_{\boldsymbol{x}} \left(m_\alpha n_\alpha \langle \boldsymbol{v}\boldsymbol{v} \rangle \right) - e_\alpha n_\alpha \mathbf{E} &= 0 \end{aligned} \tag{1.11}$$

By defining the perturbation velocity $\boldsymbol{v}' = \boldsymbol{v} - \boldsymbol{V}$ whose average is zero, one has

$$\begin{aligned} \langle v_i v_j \rangle &= \left\langle \left(V_i + v_i' \right) \left(V_j + v_j' \right) \right\rangle \\ &= \langle V_i V_j \rangle + \left\langle v_i' v_j' \right\rangle \end{aligned} \tag{1.12}$$

If the plasma is isotropic,

$$\left\langle v_i' v_j' \right\rangle = 0, \quad \forall\, i \neq j \tag{1.13}$$

and if only one direction gives non-zero component of the average velocity, then

$$\begin{aligned} \langle v_i v_j \rangle &= 0, \quad \forall\, i \neq j \\ \langle v_i v_j \rangle &= {V_i}^2 + \left\langle {v_i'}^2 \right\rangle, \quad \forall\, i = j \end{aligned} \tag{1.14}$$

For a motion in the x direction, Eq. (1.11) can be written in the form

$$\begin{aligned} \partial_t n_\alpha + \partial_x \left(n_\alpha V_\alpha \right) &= 0 \\ \partial_t \left(m_\alpha n_\alpha V_\alpha \right) + \partial_x \left(m_\alpha n_\alpha \left\langle {v_x}^2 \right\rangle \right) &= e_\alpha n_\alpha E_x \end{aligned} \tag{1.15}$$

[1]Because the fluid is assumed isothermal, *i.e.* species's temperature remains constant, the energy equation is neglected in this development.

where V_α and E_x represents the average velocity and the electric field in the x direction. The macroscopic temperature of particle T_α can then be obtained from the expression of the microscopic kinetic and temperature energy

$$\frac{m_\alpha \left\langle {v_x}'^2 \right\rangle}{2} = \frac{\mathrm{k_B} T_\alpha}{2} \tag{1.16}$$

where ${v_x}' = v_x - V_\alpha$ is the velocity fluctuation in the x direction and $\mathrm{k_B}$ is the Boltzmann constant. Recalling that $\langle {v_x}' \rangle = 0$, it gives

$$\begin{aligned} \left\langle {v_x}^2 \right\rangle &= \left\langle (V_\alpha + {v_x}')^2 \right\rangle \\ &= {V_\alpha}^2 + \left\langle {v_x}'^2 \right\rangle \\ &= {V_\alpha}^2 + \frac{\mathrm{k_B} T_\alpha}{m_\alpha} \end{aligned} \tag{1.17}$$

Substituting Eq. (1.17) in Eq. (1.15) and given that the electric potential ϕ follows the relation $E_x = -\partial_x \phi$, one get

$$\begin{aligned} \partial_t n_\alpha + \partial_x \left(n_\alpha V_\alpha \right) &= 0 \\ \partial_t \left(n_\alpha V_\alpha \right) + \partial_x \left(n_\alpha {V_\alpha}^2 + \frac{n_\alpha \mathrm{k_B} T_\alpha}{m_\alpha} \right) &= \frac{e_\alpha n_\alpha}{m_\alpha} \partial_x \phi \end{aligned} \tag{1.18}$$

One may note that Eq. (1.18) is not sufficient to completely solve the system as there is no equation for ϕ. An additional one in then added to close the system. It takes the form of a Poisson equation for the electric potential

$$\partial_{xx} \phi = \frac{\rho}{\epsilon_0} \tag{1.19}$$

where

$$\rho = \sum_{\alpha=1}^{N} n_\alpha e_\alpha \tag{1.20}$$

is the electric charge density of a plasma mixture composed of N different species and ϵ_0 is the dielectric permittivity of the vacuum.

Finally, the ionisation effect from the right hand side of the Boltzmann's Equation is taken into account. Since this phenomenon impacts only the amount of particles in the discharge, it is mostly felt by the number density of each particle. As a result, the ionisation rate is expected to appear only in the right hand side of the density transport equation.

Therefore, taking into account the ionisation and the Poisson equation, the isothermal Multi-fluid model for a particle α can be written in a general way following

$$\begin{aligned} \partial_t n_\alpha + \partial_x \left(n_\alpha V_\alpha \right) &= J_\alpha \\ \partial_t \left(n_\alpha V_\alpha \right) + \partial_x \left(n_\alpha {V_\alpha}^2 + \frac{n_\alpha \mathrm{k_B} T_\alpha}{m_\alpha} \right) &= \frac{e_\alpha n_\alpha}{m_\alpha} \partial_x \phi \\ \partial_{xx} \phi &= -\sum_{\alpha=1}^{N} \frac{n_\alpha e_\alpha}{\epsilon_0} \end{aligned} \tag{1.21}$$

where J_α represents the particle's ionisation phenomena. This equation will be particularise to the current single-charged electrons and ions configuration in the following chapter.

Chapter 2

Application to a binary mixture configuration

Now that the Multi-Fluid model has been derived, it has to be applied to the current configurations which considered a binary mixture of electrons and ions. Eq. (1.21) then reduces to a so-called Two-Fluid model discussed here. Then, a more precise description of these configurations used in this work is presented alongside the boundary conditions involved in the plasma sheath. Finally, the non-dimensional version of the Two-fluid model is derived revealing its three key parameters, namely: the electron-to-ion mass ratio, the ion-to-electron temperature ratio and the non-dimensional Debye length.

2.1 Two-Fluid model

The Two-fluid model coupled with a Poisson equation, also know as the two-fluid Euler-Poisson equations, has been proven to be a useful tool for the simulation of isothermal collisionless plasma and is then used in the current work. It consists of particularising Eq. (1.21) when only two species are considered. The first one are the electrons carrying a charge $-e$ and the second one are ions with a charge e, where $e = 1.602176634 \cdot 10^{-19}$ C represents the elementary charge. The two-fluid Euler-Poisson equations then read

$$\begin{aligned}
&\partial_t n_e + \partial_x \left(n_e u_e\right) && = n_e\, \nu \\
&\partial_t n_i + \partial_x \left(n_i u_i\right) && = n_e\, \nu \\
&\partial_t \left(n_e u_e\right) + \partial_x \left(n_e {u_e}^2 + \frac{p_e}{m_e}\right) && = \frac{n_e\, e}{m_e} \partial_x \phi \\
&\partial_t \left(n_i u_i\right) + \partial_x \left(n_i {u_i}^2 + \frac{p_i}{m_i}\right) && = -\frac{n_i\, e}{m_e} \partial_x \phi \\
&\partial_{xx} \phi && = \frac{n_e - n_i}{\epsilon_0} e
\end{aligned} \tag{2.1}$$

where the subscripts e and i represent quantities attached to electrons and ions, n_e and n_i are then the number densities u_e and u_i are the velocities, $p_e = n_e \mathrm{k_B} T_e$ and $p_i = n_i \mathrm{k_B} T_i$ are the local pressures assumed to follow the perfect gas law, m_e and m_i are the masses,

e is the positive elementary charge, ϕ is the electric potential and ϵ_0 is the dielectric permittivity of the vacuum. One may notice the same ionisation $J_{e,i} = n_e\nu$, with ν the ionisation rate, is encountered by both species. Indeed, when an electron is created through ionisation an ion is also created so that they both have the same expression.

In this work, the complete two-fluid Euler-Poisson system of equations given in Eq. (2.1) will be solved numerically. This system will be used to resolve two different problems: the first one being two-stream periodic perturbations and the second one dealing with the plasma sheath problem. A description of these is available in the following section. During the simulation because of the huge constraint coming from the electrons/ions disparity, an implicit time marching will be implemented.

Despite the more flexibility in term of numerical stability, the implicit time stepping allows us to integrate the evolution equations for the particles together with the Poisson equation for the potential. Indeed, the latter is not an evolution equation, but a relation that needs to be satisfied at each instant in time - including the sub-timesteps of the Runge-Kutta time integrator. The equations resulting from the implicit time integration of the particle equations on the one hand, and the Poisson system on the other, are therefore combined in a single Newton iteration at each sub-timestep.

2.2 Definition of the two-stream perturbation problem

This first problem consists of the propagation of a two-stream instabilities in a low-temperature collisionless isothermal plasma [27, 26] and will serve as a validation of the project implementation. This instability occurs in a uniform mixture of density n_0 and where there is a relative velocity $\boldsymbol{u}_0$ between the electrons and the ions [18]. In this problem, thermal plasma is considered. This means that electrons and ions possess the same temperature, *i.e.* $T_e = T_i$. In addition, ions that are 10^4 heavier than the electrons are considered as well as periodic boundary conditions. A resume of the specifications associated to the two-stream instability covered here is available in table 2.1 [2].

Two-stream instability					
normalised reference density	n_0	1	Electron-to-ion mass ratio	$\varepsilon = {}^{m_e}/_{m_i}$	10^{-4}
normalised reference velocity	u_0	1	Ion-to-electron temperature ratio	$\kappa = {}^{T_i}/_{T_e}$	1
domain length	L	1	normalised Debye length	$\lambda = {}^{\lambda_D}/_{L}$	10^{-4}

Table 2.1: Characteristics parameters of the two-stream instability problem [2].

The specificity of this test case is that it neglects the ionisation phenomena inside the mixture, *i.e.* $\nu \approx 0$. This leads to a right hand side that accounts only for the particles/potential interaction. In addition to that, an analytical solution to this problem is

available [27, 25]. The latter takes the form of a sine wave of frequency ω and wavelength k that is convected in the direction of the velocity u_0. Mathematically, it has the expression (see Appendix C for a detailed derivation)

$$\boldsymbol{u}(x,t) = \boldsymbol{u}_0(x) + \tilde{\boldsymbol{u}}\sin\left(kx - \omega t\right) \tag{2.2}$$

with $\boldsymbol{u}_0$ the steady value and $\tilde{\boldsymbol{u}}$ the perturbation amplitudes. The tilde is here to emphasise the perturbed value. Assuming a fixed wavelength $k = 2\pi$, the value of ω is retrieved from the characteristics equations of the electrons/ions transport system that takes the form of a fourth-order dispersion relation [14] (see Appendix C.1 for a derivation)

$$F(k,\omega) \equiv \alpha_4\omega^4 + \alpha_3\omega^3 + \alpha_2\omega^2 + \alpha_1\omega + \alpha_0 = 0 \tag{2.3}$$

with

$$\begin{gathered}\alpha_4 = \varepsilon\chi, \qquad \alpha_3 = -2\varepsilon\chi k u_0, \qquad \alpha_2 = \left(\varepsilon k^2\chi\left(u_0^2 - \kappa\right) - \varepsilon n_0 - k^2\chi - n_0\right) \\ \alpha_1 = 2\left(k^2\kappa\chi + n_0\right)\varepsilon k u_0 \quad \text{and} \quad \alpha_0 = -\varepsilon k^2 u_0^2 n_0 - \varepsilon\chi k^4\kappa u_0^2 + k^4\kappa\chi + k^2 n_0\left(\kappa + 1\right)\end{gathered} \tag{2.4}$$

Then, if Eq. (2.3) admits four real roots, it has been shown that the obtained ω will lead to a stable solution.

2.3 Definition of the plasma sheath problem

As briefly introduced in section 1.1, the sheath problem that studied here consists of a binary mixture plasma trapped inside a cylinder with equipotential walls of infinite height and a radius equals to unity (in non-dimensional units), commonly refer as a *discharge*. The problem is also considered unidimensional, with x representing the position of a particle along the cylinder diameter. This problem is has been well described by Chabert & Braithwaite [14]. A resume of the specifications for discharge composed of Argon+ is available in table 2.2.

Dimensionnal quantities				Dimensionless quantities		
reference number density	n_0	10^{16}	m^{-3}	Electron-to-ion mass ratio	$\varepsilon = {}^{m_e}/_{m_i}$	1.36×10^{-5}
Ion mass	m_i	40	u	Ion-to-electron temperature ratio	κ	0.025
Ion temperature	T_i	0.05	eV	Normalized Debye length	$\lambda = {}^{\lambda_D}/_{L}$	3.5×10^{-3}
Electron temperature	T_e	2	eV	Normalized ionization rate	$\tilde{\nu}^{iz}$	0.0139
Bohm velocity	u_B	2187.87	ms^{-1}	Normalised square of the electron Debye length	$\chi = \lambda^2$	
Electron plasma period	ω_p^{-1}	1.77×10^{-10}	s	Normalized plasma period	$\tilde{\omega}_p^{-1} = {}^{\omega_p^{-1}u_B}/_{L}$	1.29×10^{-5}

Table 2.2: Characteristics value of an Argon+ RF Discharge [14].

For this problem a quasi-neutral plasma of density $n_e = n_i = n_0$ is considered at the beginning. After a certain time, because of the huge disparity in mass, and hence in mobility, a region of depleted electrons grows in the vicinity of the walls. In this sheath, the quasi-neutrality is no more respected and lead to a very steep gradient of the potential between this region and the central region, called *bulk*.

The purpose of this work is therefore to find a steady state to this sheath formation as it has been done by Alvarez Laguna *et al.* [2] with its AP-scheme. An illustration of the steady state solutions coming from his work is depicted in Fig. 2.1. One can noticed the violation of the quasi-neutrality in the sheath and the steep gradient of the potential.

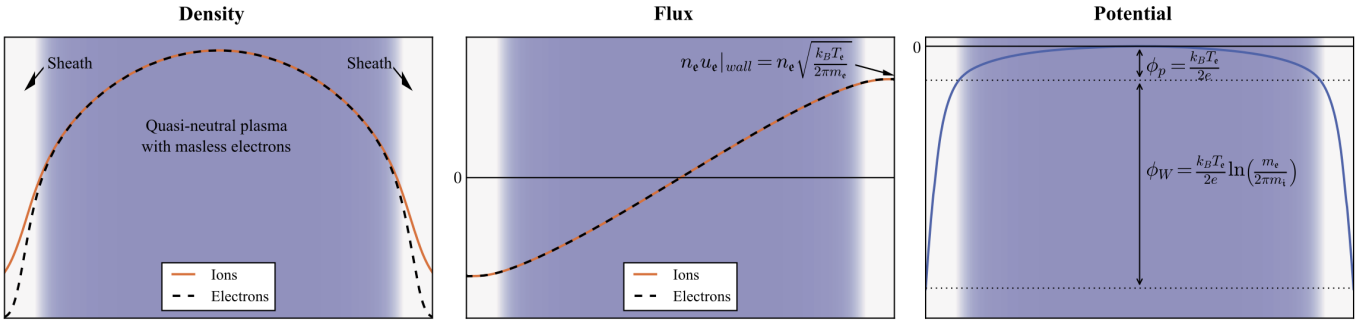

Fig. 2.1: Solution of a low temperature Argon+ plasma trapped in a RF discharge found with a fluid model [2, 65].

2.3.1 Boundary conditions

In the near wall this region, the plasma is characterised by a depletion of electron and is no longer quasi-neutral. Although the sheath can be describe following the Child-Langmuir law [20, 50], the boundary conditions are set following the theory developed by Rieman *et al.* [65].

A Maxwellian distribution function for the electron is assumed and that all the electrons are absorbed by the wall [36]. If there is no secondary emission, the flux of electrons collected by the walls is analog to Γ_e in Eq. (1.3), hence

$$n_e u_e|_{left} = -\, n_e u_e|_{right} = -n_e\sqrt{\frac{\mathrm{k_B} T_e}{2\pi m_e}} \tag{2.5}$$

On the other hand, a common practice is to consider that the charged heavy ions must satisfy what is called the Bohm criterion. This condition states that the ions must enter the sheath at velocity higher than its own speed of sound [8] which is commonly called the "Bohm speed" and reads

$$u_B = \sqrt{\frac{\mathrm{k_B} T_e}{m_i}} \tag{2.6}$$

As a consequence, the ions are supersonic when entering the sheath, and leaving the domain [60]. For this reason, Neumann boundary conditions with zero gradients at the walls are used for the ions quantities n_i and $n_i u_i$. This means that their inner values are imposed at the boundaries.

In order to find a steady state flux of ions exiting the domain, particular attention has to be paid onto the definition of the ionisation frequency ν. In addition to that, Riemann *et al.*[65] has revealed that the ν is an eigenvalue of the problem. This means that there is only one value of ν that permits to find a steady state solution. Alvarez Laguna *et al.*[2] proposed an iterative procedure to obtain this value of ν that guarantee the solution to reach a steady state which, for a domain length L, is given by

$$\nu(t) = \frac{|n_i u_i(x=0,t)| + |n_i u_i(x=L,t)|}{\int_0^L n_e(x,t)\,dx} \tag{2.7}$$

Finally, the boundary conditions associated with the potential has to be defined. Since the potential is referrenced at the wall, one has

$$\phi(x=0) = \phi(x=L) = 0 \tag{2.8}$$

2.4 Non-dimensional equations

A non-dimensional form of the Two-fluid Euler-Poisson equations given in (2.1) can be obtained by introducing some reference quantities: $n_0 \equiv n_{e0} \equiv n_{i0}$, the reference number density common to both electrons and ions, $L_0 = l$, the reference length, T_e, the electrons temperature and m_i, the ions mass. The other reference quantities are then obtained from the previous ones: the reference velocities is based on the Bohm speed $u_0 \equiv u_B = \sqrt{\frac{\mathrm{k_B}T_e}{m_i}}$ and the characteristics time $t_0 = \frac{L_0}{u_B}$ is obtained from the reference length and velocity. The electric potential is also scaled by $\phi_0 = \frac{\mathrm{k_B}T_e}{e}$. Note that the electric potential is scaled by the electron temperature expressed in eV for low-temperature plasma [14]. It gives the following non-dimensional quantities

$$\tilde{n}_e = \frac{n_e}{n_0}, \quad \tilde{n}_i = \frac{n_i}{n_0}, \quad \tilde{u}_e = \frac{u_e}{u_0}, \quad \tilde{u}_i = \frac{u_i}{u_0}, \quad \tilde{x} = \frac{x}{L_0}, \quad \tilde{t} = \frac{t}{t_0} \quad \text{and} \quad \tilde{\phi} = \frac{\phi}{\phi_0}. \tag{2.9}$$

where the quantities with $\tilde{(\cdot)}$ are non-dimensional. This "tilde" is dropped in the following chapter in order to avoid clutter.

While for most of the term the treatment is classical and straightforward, a particular attention is made on some terms as they are specific to the current problem. In these terms, the remaining dimensional quantities will be highlighted in an other colour to make the derivation clearer.

For the local pressure term assumed to follow prefect gas law, the scaling is

$$\begin{aligned}
\partial_x\left(\frac{p_e}{m_e}\right) &= \partial_x\left(\frac{n_e \mathrm{k_B} T_e}{m_e}\right) = \partial_x\left(\frac{n_e \mathrm{k_B} T_e}{\varepsilon m_i}\right) = \frac{1}{L_0}\partial_{\tilde{x}}\left(n_0\, {u_B}^2 \varepsilon^{-1}\tilde{n}_e\right) = \frac{n_0 u_B}{t_0}\partial_{\tilde{x}}\left(\varepsilon^{-1}\tilde{n}_e\right) \\
\partial_x\left(\frac{p_i}{m_i}\right) &= \partial_x\left(\frac{n_i \mathrm{k_B} T_i}{m_i}\right) = \partial_x\left(\frac{n_i \mathrm{k_B} \kappa T_e}{m_i}\right) = \frac{1}{L_0}\partial_{\tilde{x}}\left(n_0\, {u_B}^2 \kappa\tilde{n}_i\right) = \frac{n_0 u_B}{t_0}\partial_{\tilde{x}}\left(\kappa\tilde{n}_i\right)
\end{aligned} \tag{2.10}$$

The electric forcing term becomes :

$$\begin{aligned}
&\frac{n_e\, e}{m_e}\partial_x\phi = \frac{n_e\, e}{\varepsilon m_i}\partial_x\phi = \frac{n_0\, e}{m_i L_0}\varepsilon^{-1}\tilde{n}_e\partial_{\tilde{x}}\left(\frac{\mathrm{k_B}T_e}{e}\tilde{\phi}\right) = \frac{n_0\, {u_B}^2}{L_0}\varepsilon^{-1}\tilde{n}_e\partial_{\tilde{x}}\tilde{\phi} = \frac{n_0\, u_B}{t_0}\varepsilon^{-1}\tilde{n}_e\partial_{\tilde{x}}\tilde{\phi}\\
&-\frac{n_i\, e}{m_i}\partial_x\phi = -\frac{n_0\, e}{m_i L_0}\tilde{n}_i\partial_{\tilde{x}}\left(\frac{\mathrm{k_B}T_e}{e}\tilde{\phi}\right) = -\frac{n_0\, {u_B}^2}{L_0}\tilde{n}_i\partial_{\tilde{x}}\tilde{\phi} = -\frac{n_0\, u_B}{t_0}\tilde{n}_i\partial_{\tilde{x}}\tilde{\phi}
\end{aligned} \tag{2.11}$$

The non-dimensional ionisation term can be easily obtained from the adimensional ionisation frequency $\tilde{\nu} = \nu\, t_0$, giving

$$n_e\nu = \frac{n_0}{t_0}\tilde{n}_e\tilde{\nu} \tag{2.12}$$

Finally, the Poisson equation is nondimensionalised following

$$\partial_{xx}\phi = \frac{n_e - n_i}{\epsilon_0}e \tag{2.13}$$

$$\Leftrightarrow \frac{1}{{L_0}^2}\partial_{\tilde{x}\tilde{x}}\left(\frac{\mathrm{k_B}T_e}{e}\tilde{\phi}\right) = \frac{n_0\, e}{\epsilon_0}\left(\tilde{n}_e - \tilde{n}_i\right) \tag{2.14}$$

$$\Leftrightarrow \partial_{\tilde{x}\tilde{x}}\tilde{\phi} = \frac{n_0\, e^2\, {L_0}^2}{\mathrm{k_B}T_e}\left(\tilde{n}_e - \tilde{n}_i\right) \tag{2.15}$$

$$\Leftrightarrow \partial_{\tilde{x}\tilde{x}} = \chi^{-1}\left(\tilde{n}_e - \tilde{n}_i\right) \tag{2.16}$$

Following these results, the non-dimensional expression of Eq. (2.1) reads

$$\begin{aligned}
&\partial_{\tilde{t}}\tilde{n}_e + \partial_{\tilde{x}}\left(\tilde{n}_e\tilde{u}_e\right) && = \tilde{n}_e\,\tilde{\nu}\\
&\partial_{\tilde{t}}\tilde{n}_i + \partial_{\tilde{x}}\left(\tilde{n}_i\tilde{u}_i\right) && = \tilde{n}_e\,\tilde{\nu}\\
&\partial_{\tilde{t}}\left(\tilde{n}_e\tilde{u}_e\right) + \partial_{\tilde{x}}\left(\tilde{n}_e\tilde{u}_e^2 + \tilde{n}_e\varepsilon^{-1}\right) && = \tilde{n}_e\varepsilon^{-1}\partial_{\tilde{x}}\tilde{\phi}\\
&\partial_{\tilde{t}}\left(\tilde{n}_i\tilde{u}_i\right) + \partial_{\tilde{x}}\left(\tilde{n}_i\tilde{u}_i^2 + \tilde{n}_i\kappa\right) && = -\tilde{n}_i\partial_{\tilde{x}}\tilde{\phi}\\
&\partial_{\tilde{x}\tilde{x}}\tilde{\phi} && = \chi^{-1}\left(\tilde{n}_e - \tilde{n}_i\right)
\end{aligned} \tag{2.17}$$

One can notice the appearance of three non-dimensional parameters defined as:

1. $\varepsilon = \dfrac{m_e}{m_i}$, the electron-to-ion mass ratio;
2. $\kappa = \dfrac{T_i}{T_e}$, the ion-to-electron temperature ratio;
3. $\chi = \dfrac{{\lambda_D}^2}{{L_0}^2} = \dfrac{\mathrm{k_B}T_e}{n_0\, e^2 {L_0}^2}$, the squared non-dimensional Debye-length.

Those non-dimensional parameters plays an important role in the numerical behaviour of the system. The first two quantities, ε and κ, play a role in the definition of the system's propagation speed as shown in section 3.2, while χ, appearing in the Poisson's equation, has an impact in the evaluation of the non-dimensional electric potential $\tilde{\phi}(x)$ [2].

We can now reformulate the boundary conditions introduced in the section before in scaled quantities. The normalised electron flux passing through the boundaries becomes

$$n_e u_e|_{left} = - n_e u_e|_{right} = -\frac{\tilde{n}_e}{\sqrt{2\pi\varepsilon}} \tag{2.18}$$

Similarly, for the non-dimensional potential, one has

$$\tilde{\phi}_{left} = \tilde{\phi}_{right} = 0 \tag{2.19}$$

Chapter 3

Structure of the equations

In this chapter, the mathematical structure of the Two-fluid model proposed in Eq. (2.1) is studied, highlighting the contributions of two different subsystems namely, the fluid one and the electrostatic equation. The eigenvalues and eigenvectors of the hyperbolic scheme are then computed as well as the characteristic velocities of the system. Finally, a discussion of the characteristics entering and leaving the domain is presented, since they have a strong impact on the implementation of the boundary conditions.

3.1 Hyperbolic and elliptic equations

The normalised two-fluid Euler-Poisson equations used to describe plasma sheath problem are the following:

$$\begin{aligned}
&\partial_t n_e + \partial_x \left(n_e u_e\right) && = n_e\, \nu \\
&\partial_t n_i + \partial_x \left(n_i u_i\right) && = n_e\, \nu \\
&\partial_t \left(n_e u_e\right) + \partial_x \left(n_e {u_e}^2 + n_e \varepsilon^{-1}\right) && = n_e \varepsilon^{-1} \partial_x \phi \\
&\partial_t \left(n_i u_i\right) + \partial_x \left(n_i {u_i}^2 + n_i \kappa\right) && = -\, n_i \partial_x \phi \\
&\partial_{xx} \phi && = \chi^{-1} \left(n_e - n_i\right)
\end{aligned} \tag{3.1}$$

This system of equations can be split into two subsystems: a hyperbolic one, which consists of the first four equations of Eq. (3.1) and an elliptic one, composed of Poisson's equation for the electric potential. Because of their structures, these two subsystems exhibit totally different behaviours. As an example, the hyperbolic schemes presents characteristics lines in the domains. This means that the simulation depends of finite propagation speeds that must be determined. This will be done in the next section.

On the other hand, for the elliptic subsystem

$$\partial_{xx} \phi = \chi^{-1} \left(n_e - n_i\right) \tag{3.2}$$

no real characteristics can be found since Eq. (3.2) is characterised by infinite speed of propagation of a perturbation. In this case, a solution at given position in the domain would depend on the whole domain including the boundaries. The only condition to find a definite solution to Eq. (3.2) is then to impose a set of boundary conditions.

3.2 Eigenvalues and eigenvectors of the hyperbolic equations

Let us consider here the first four equations of Eq. (3.1)

$$\begin{aligned}
\partial_t n_e + \partial_x \left(n_e u_e\right) &= n_e\, \nu \\
\partial_t n_i + \partial_x \left(n_i u_i\right) &= n_e\, \nu \\
\partial_t \left(n_e u_e\right) + \partial_x \left(n_e {u_e}^2 + n_e \varepsilon^{-1}\right) &= n_e \varepsilon^{-1} \partial_x \phi \\
\partial_t \left(n_i u_i\right) + \partial_x \left(n_i {u_i}^2 + n_i \kappa\right) &= -\, n_i \partial_x \phi
\end{aligned} \tag{3.3}$$

This set of equation can be rewritten in conservative form as

$$\partial_t \boldsymbol{u} + \partial_x \boldsymbol{F} = \boldsymbol{S} \tag{3.4}$$

with the conservative variable vector

$$\begin{aligned}
\boldsymbol{u} &= \begin{pmatrix} n_e & n_i & n_e u_e & n_i u_i \end{pmatrix}^T \\
\boldsymbol{F} &= \begin{pmatrix} n_e u_e & n_i u_i & n_e {u_e}^2 + n_e \varepsilon^{-1} & n_i {u_i}^2 + n_i \kappa \end{pmatrix}^T \\
\boldsymbol{S} &= \begin{pmatrix} n_e \nu & n_e \nu & \varepsilon^{-1} n_e \partial_x \phi & -n_i \end{pmatrix}^T
\end{aligned} \tag{3.5}$$

denote respectively the unknowns vector $\boldsymbol{u}$, the fluxes vector $\boldsymbol{F}$ and the source term vector $\boldsymbol{S}$. Alternatively, Eq. (6.4) can also be written as

$$\partial_t \boldsymbol{u} + \boldsymbol{A} \partial_x \boldsymbol{u} = \boldsymbol{S} \tag{3.6}$$

with

$$\boldsymbol{A} = \frac{\partial \boldsymbol{F}}{\partial \boldsymbol{u}} = \begin{pmatrix} 0 & 0 & 1 & 0 \\ 0 & 0 & 0 & 1 \\ \varepsilon^{-1} - {u_e}^2 & 0 & 2u_e & 0 \\ 0 & \kappa - {u_i}^2 & 0 & 2u_i \end{pmatrix} \tag{3.7}$$

The matrix $\boldsymbol{A}$ admits a set of real and non degenerate eigenvalues

$$\begin{aligned}
\lambda_0 &= u_e - \sqrt{\varepsilon^{-1}} \\
\lambda_1 &= u_e + \sqrt{\varepsilon^{-1}} \\
\lambda_2 &= u_i - \sqrt{\kappa} \\
\lambda_3 &= u_i + \sqrt{\kappa}
\end{aligned} \tag{3.8}$$

which represent the propagation speeds of the information in the system. The system eigenvectors are then

$$\begin{aligned}
\boldsymbol{v}_0 &= \begin{pmatrix} 1 & 0 & \lambda_0 & 0 \end{pmatrix} \\
\boldsymbol{v}_1 &= \begin{pmatrix} 1 & 0 & \lambda_1 & 0 \end{pmatrix} \\
\boldsymbol{v}_2 &= \begin{pmatrix} 0 & 1 & 0 & \lambda_2 \end{pmatrix} \\
\boldsymbol{v}_3 &= \begin{pmatrix} 0 & 1 & 0 & \lambda_3 \end{pmatrix}
\end{aligned} \tag{3.9}$$

From Eq. (3.8), one can extract the normalised speed of sound of the electrons $c_e = \sqrt{\varepsilon^{-1}}$ and ions $c_i = \sqrt{\kappa}$. In the case of Argon+ plasma, they equal [14]

$$c_e = \sqrt{\varepsilon^{-1}} \simeq 271 \qquad c_i = \sqrt{\kappa} \simeq 0.16 \tag{3.10}$$

For the sheath, this strong velocity disparity between the electrons and ions is very constraining to the numerical simulation. Indeed, the numerical scheme must be able to capture phenomena that happen at very different speeds. This coupled with steep gradient encountered in the presheath and the sheath, results in a very stiff problem to solve. Those difficulties will be summarised in section 5.1 speaking about the stability of the numerical schemes.

3.2.1 Boundary conditions and characteristics lines

A quick analysis of the characteristics behaviour at the frontier of the domain will permit to correctly set the different boundary conditions. As explained in section 2.3.1, in the case of the sheath problem ions are supersonic when they enter the sheath and are expected to be supersonic when they collide with the walls. As a consequence, the characteristics associated to λ_2 and λ_3 are pointing outward the domain. In other words, the ions take the information from inside the discharge and convect it outside. For this reason, there is no need of specifying a boundary condition for the ions.

Conversely, from Eq. (2.18), one find an electron velocity at the boundary that ranges

$$\sqrt{\frac{1}{2\pi\varepsilon}} \simeq 108 < \sqrt{\varepsilon^{-1}} \tag{3.11}$$

It means that the electrons are subsonic when they collide with the wall. The characteristics associated to λ_0 and λ_1 are always organised as one pointing inside the domain and the other point outside. The electrons takes thereby the information from both outside and inside the domain. Since at each boundary only one characteristics enters the domain, one has to specify only one boundary condition per walls for the electrons.

This quick analysis permits to correctly set the boundary conditions of the sheath problem. However, if the numerical flux is a true upwind scheme, it will not consider the values at the boundaries if the particle is supersonic.

Part II

Numerical methods

Chapter 4

Discontinuous Galerkin Finite Element Method

This Chapter presents the Discontinuous Galerkin finite element method (DG-FEM) and its application to the current plasma model. This method uses discontinuous interpolation in combination with a Galerkin variational formulation. The main property of DG-FEM is the *broken trial space*. The solution is fully regular inside the element, but not necessarily continuous across elements. In contrast to most finite element method in which the solution has to be at least C^0 across elements.

Since 1973, this methods has developed a vast domain of application [63, 21] although it starts being used more frequently over the recent years. Indeed, working with DG-FEM has several advantages:

- the capability to provide a consistently high order of accuracy in terms of interpolation and spectral properties, almost independent of (unstructured) mesh quality;
- the element boundary flux formulation allows for a straightforward and fully precise implementation of boundary conditions without local modification of the method;
- the lack of continuity introduces extra flexibility in the local choice of interpolation order and the use of non-standard shape functions. (*e.g.* Multi-order DG-FEM).

The Chapter is organised as follows. First, the DG method is presented in a general manner and applied to a very general conservative law. Then, the discretisation is applied to the current plasma system of equations, with a discussion of proper numerical fluxes, the internal penalty method and the computation of the source term. Finally, a description of ForDGe, the DG-FEM solver used for this work, is made.

4.1 Application to a conservative system

Let us consider the general conservative system [39]

$$\partial_t \boldsymbol{u}(x,t) + \partial_x \boldsymbol{F}(\boldsymbol{u},x,t) + \partial_x \boldsymbol{D}(\boldsymbol{u},\partial_x \boldsymbol{u},x,t) = \boldsymbol{S}(\boldsymbol{u},x,t) \quad x \in \Omega,\, t \in \mathbb{R}^+ \tag{4.1}$$

with Ω being the unidimensional domain, x the position on Ω, and t the temporal variable. $\boldsymbol{u}$ is the state vector of conserved variables, $\boldsymbol{F}$ is the convective flux vector, $\boldsymbol{D}$ is the diffusive flux vector and $\boldsymbol{S}$ represents the source term vector.

Moreover, the diffusive flux $\boldsymbol{D}$ can be expressed in the following manner [39] (Einstein notation has been adopted, *i.e.* summation occurs on repeated indices)

$$D_m^k = -\mathcal{D}_{kl}^{mn} \frac{\partial u_n}{\partial x^l} \tag{4.2}$$

where $\mathcal{D}$ is the Jacobian matrix of $\boldsymbol{D}$ with respect to the solution gradient, with m and n the indices over the variables, and k and l on the coordinate directions. A particular attention will be addressed to this contribution.

4.1.1 Galerkin variational formulation

In order to express a general form of the Galerkin Variational formulation, a generic flux $\boldsymbol{G} = \boldsymbol{F} + \boldsymbol{D}$ is considered here so that Eq. (4.1) is reformulated as

$$\partial_t \boldsymbol{u}(x,t) + \partial_x \boldsymbol{G}(\boldsymbol{u}, \partial_x \boldsymbol{u}, x, t) = \boldsymbol{S}(\boldsymbol{u}, x, t) \quad x \in \Omega,\, t \in \mathbb{R}^+ \tag{4.3}$$

A weak form of Eq. (4.3) can be obtained by multiplying both members by $\phi(x)$, $\phi \in C_1(\Omega)$ and integrating over the whole domain Ω. After integration by parts, it gives the following "weak form"

$$\int_\Omega \left(\partial_t \boldsymbol{u} - \boldsymbol{S}\right) \varphi \, dV - \int_\Omega \boldsymbol{G}\, \partial_x \varphi \, dV + \oint_{\partial\Omega} \boldsymbol{G} \cdot \boldsymbol{n}\, \varphi \, dS = 0 \tag{4.4}$$

where $\boldsymbol{n}$ is the normal of the face boundary $\partial\Omega$ pointing outward of the element.

Let us consider now that the domain Ω is partitioned in $\mathcal{N}$ non-overlapping elements with Ω_e corresponding to an element. The frontier $\partial\Omega_e$ is then the union of the faces f of the element. Mathematically, it means that

$$\partial\Omega_e = \bigcup_f I_f \tag{4.5}$$

where I_f represents the interfaces between two elements or between one element and the boundary of the domain. As a result, Eq. (4.4) becomes

$$\sum_e \int_\Omega \left(\partial_t \boldsymbol{u} - \boldsymbol{S}\right) \varphi \, dV - \sum_e \left(\int_e \boldsymbol{G}\, \partial_x \varphi \, dV + \sum_{f \in \partial\Omega_e} \boldsymbol{G} \cdot \boldsymbol{n}\, \varphi \, dS \right) = 0 \tag{4.6}$$

where the subscript e stands for an element and f the element's faces. The last term involves inter-element flux which depends on the value of $\boldsymbol{u}$ and φ at the two sides of the boundary such as

$$\sum_{f \in \partial\Omega_e} \boldsymbol{G} \cdot \boldsymbol{n}\, \varphi \, dS = \sum_f \int_f \varphi \boldsymbol{G} \cdot \boldsymbol{n} dS \tag{4.7}$$

$$= \sum_f \int_f \left(\varphi^+ \boldsymbol{G}^+ \cdot \boldsymbol{n}^+ + \varphi^- \boldsymbol{G}^- \cdot \boldsymbol{n}^-\right) dS \tag{4.8}$$

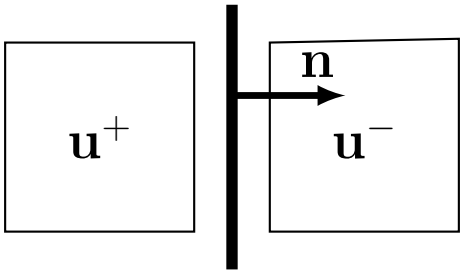

Fig. 4.1: Schematics of the convention used for suffixes + and − carried by the solution when approaching the interface (represented by the thick line).

The + and − are here to distinguish the values at both side of an interface, depending on the element from which the interface is approached. As illustrated in Fig. 4.1, the sign + corresponds to the elements of which its exterior normal corresponds to that of the oriented face, while −corresponds to the other (*i.e.* $\boldsymbol{n}^+ = \boldsymbol{n}$ and $\boldsymbol{n}^- = -\boldsymbol{n}$). The general Galerkin variational formulation is hence

$$\sum_e \int_\Omega \left(\partial_t \boldsymbol{u} - \boldsymbol{S}\right) \varphi \, dV - \sum_e \int_e \boldsymbol{G} \, \partial_x \varphi \, dV + \sum_f \int_f \gamma \left(\boldsymbol{u}^+, \boldsymbol{u}^-; \varphi^+, \varphi^-; \boldsymbol{n}\right) dS = 0 \quad (4.9)$$

where the first term accounts for the temporal derivative of the elemental solution and its source term $\boldsymbol{S}$, the middle term is related to the element's volume flux $\boldsymbol{G}$ and the last one to the interface flux γ. A particular attention will be paid onto the definition of the last flux γ since this term has no general expression. Moreover, its formulation depends strongly on the subsystem that is considered, either the hyperbolic one, nor the elliptic.

4.1.2 Convective variational formulation

It has been found that the discretisation of the convective part of Eq. (4.9) is stabilised by using the approximate Riemann solvers $\mathcal{F}^*$, previously developed for the finite volume method as the basis for the interface flux [39, 21]:

$$\gamma^{\boldsymbol{F}} \left(\boldsymbol{u}^+, \boldsymbol{u}^-; \varphi^+, 0; \boldsymbol{n}\right) = \varphi^+ \mathcal{F}^* \left(\boldsymbol{u}^+, \boldsymbol{u}^-; \boldsymbol{n}\right) \quad (4.10)$$

This choice satisfies all of the requirements for a stable and convergent numerical method [30, 39]:

1. **Conservativity:** The conservation principle of Eq. (4.4) has to be retrieved at the discrete level. This is translated by the fact that the flux balance should be closed at the level of the interface, requiring:

$$\mathcal{F}^* \left(\boldsymbol{u}^+, \boldsymbol{u}^-; \boldsymbol{n}\right) = -\mathcal{F}^* \left(\boldsymbol{u}^-, \boldsymbol{u}^+; -\boldsymbol{n}\right) \quad (4.11)$$

2. **Consistency:** The numerical flux is said to be consistent if the residual equation[1]

$$V_i \partial_t \boldsymbol{u} = - \sum_{j \cap i \neq \emptyset} \int_{f_{ij}} \mathcal{F}^* \left(\boldsymbol{u}^+, \boldsymbol{u}^-; \boldsymbol{n}\right) dS \quad (4.12)$$

[1]For the sake of simplicity, the normal of the face f_{ij} is pointing outward of the cell i into the cell j in this example.

evaluated with the actual solution $\boldsymbol{u}$ is zero. The true solution is the same on either side of the face such that we find the requirement

$$\mathcal{F}^*\Big(\boldsymbol{u}, \boldsymbol{u}; \boldsymbol{n}\Big) = \boldsymbol{f}(\boldsymbol{u}) \cdot \boldsymbol{n} \tag{4.13}$$

3. **Stability:** the numerical flux should be chosen such that the solution is unique. One exmaple of stable flux is the "E-flux" (standing for "Entropy-consistent flux"). A numerical flux is then a E-flux if, $\forall \boldsymbol{v} \in \left\{\theta \boldsymbol{u}^- + (1-\theta)\boldsymbol{u}^+\right\}, \theta \in [0,1]$, one has

$$\Big(\mathcal{F}^*\Big(\boldsymbol{u}^-, \boldsymbol{u}^+; \boldsymbol{n}\Big) - \boldsymbol{f}(\boldsymbol{v})\Big)\Big(\boldsymbol{u}^+ - \boldsymbol{u}^-\Big) \geq 0 \tag{4.14}$$

This stability criterion guarantees that the entropy of the system does not grow. Since the mathematical definition of the entropy corresponds to an energy of the solution, it must decrease with time or at least remains a constant

4.1.3 Diffusive variational formulation

An *Interior Penalty Method* (IPM) is used for the discretisation of the viscous term of Eq. (4.1). This method provides compact evaluation of the residual and hence simplifies greatly the evaluation of the Jacobian [39]. On the other hand, IP methods depends on a tunable, seemingly arbitrary parameter. Sharp estimates for this parameter were developed in the thesis of Hillewaert [39].

IP methods can be constructed starting from the reinterpretation of DG methods as elementwise FEM problems, which strive for a continuous solution across boundaries by imposing the solution in the neighbouring elements as a Dirichlet condition on the element boundary.

To illustrate this, let considered a simple linear elliptic problem of a scalar u on a domain Ω with Dirichlet boundary conditions on $\partial\Omega$

$$\begin{aligned} \frac{\partial u}{\partial t} + \nabla \cdot (-\mathcal{D} \cdot \nabla u) = 0 \quad \forall x \in \Omega \\ u = u^* \quad \forall x \in \partial\Omega \end{aligned} \tag{4.15}$$

for which an approximate finite element solution u is sought using the Galerkin variational formulation:

$$\int_\Omega \varphi \frac{\partial u}{\partial t}\, dV + \int_\Omega \nabla\varphi \cdot (\mathcal{D} \cdot \nabla u)\, dV - \oint_{\partial\Omega} \varphi\, (\mathcal{D} \cdot \nabla u) \cdot \boldsymbol{n}\, dS = 0, \quad \forall \varphi \in C_1(\Omega) \tag{4.16}$$

A common approach would be to impose *strongly* the value of u at $\partial\Omega$. This is relatively easy to implement and has the intuitive advantage to use the exact the solutions at those locations where it is a priori known. However, this may not be very well suited in case the boundary condition data are noisy, as illustrated by the red line in Fig. 4.2. One would prefer an approach analogue to the green line that minimises the average interpolation error between u and u^*.

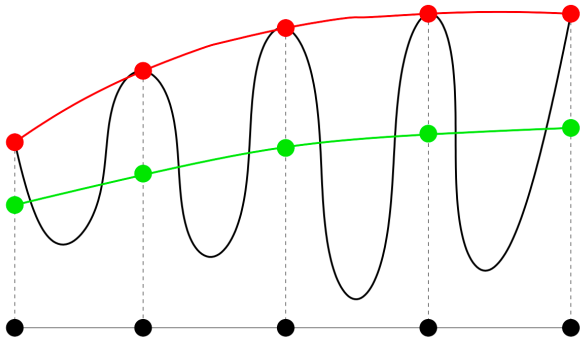

Fig. 4.2: Strong (red) and weak imposition (green) of Dirichlet boundary conditions. The strong imposition may lead to large error and potentially very rapidly varying values. The weak one would be preferred as it proposes much smoother values with also a lower global error [39].

The idea is then to penalise the difference $u-u^*$ through an additional term DP, called *Galerkin penalty term* such that

$$\int_\Omega \varphi \frac{\partial u}{\partial t}\, dV + \int_\Omega \nabla\varphi \cdot (\mathcal{D}\cdot\nabla u)\, dV - \underbrace{\int_{\partial\Omega} \sigma\varphi\,(u-u^*)\, dS}_{DP} - \underbrace{\int_{\partial\Omega} \varphi\mathcal{D}\nabla u\cdot\boldsymbol{n}\, dS}_{DD} - \theta \underbrace{\int_{\partial\Omega} (u-u^*)\,\mathcal{D}\nabla\varphi\cdot\boldsymbol{n}\, dS}_{DT} = 0 \quad (4.17)$$

where the *penalty parameter* σ is chosen such that the positive contribution of the penalty term dominates the boundary flux term. The term DD denotes the boundary flux term and is retained here for consistency[1]. The last term DT is an additional consistency term. Finally, θ is an arbitrary parameters, that can take three value depending on the type of IPM [39]:

- $\theta = 1$ for *symmetric interior penalty* (SIPDG) method, which exhibits optimal convergence.
- $\theta = -1$ for *non-symmetric interior penalty* (NIPDG) method, which elimitates the destabilising effect of the interface terms, and hence only require $\sigma > 0$.
- $\theta = 0$ for *incomplete interior penalty* (IIPDG) method, which only has the advantage of simplicity. one has to impose a value for σ that is bigger than a critical value σ_c.

Sharp optimal parameters for the "arbitrary" parameter σ were proposed in [39].

[1]In the "strongly" case, the value of u was imposed at the boundary, meaning that the method did not solve for the solution on this boundary, hence $\varphi = 0$. Now in the "weak" form, it is not the case so that this term has to be taken into account.

Therefore, for the current system of conservative equations (Eq. (4.9)), the expression of the diffusive interface flux $\gamma^{\boldsymbol{D}}$ is obtained based on these penalty terms

$$\gamma^{\boldsymbol{D}}\Big(\boldsymbol{u}^+, \boldsymbol{u}^-; \varphi^+, \varphi^-; \boldsymbol{n}\Big) = \sigma[[\varphi]] \cdot [[\boldsymbol{u}]] + [[\varphi]] \cdot \{\{\boldsymbol{D}\}\} + \theta[[\boldsymbol{u}]] \cdot \{\{\boldsymbol{D}\}\} \tag{4.18}$$

where the operators $\{\{\cdot\}\}$ and $[[\cdot]]$ represents respectively the average and the jump operator (see Appendix A for more details of these operators).

4.1.4 Shape functions and residual equation

In this section, the choose of the linearly independent function φ_i (called *shape functions*) is presented. Let us consider a set $C^0_\infty(\Omega)$ of function that are infinitely continuously differentiable on an element Ω_e and whose support is this element, and φ_i be a basis function of $C^0_\infty(\Omega_e)$. Then $\varphi \in C_1\Omega$ and Galerkin variational formulation given in Eq. (4.9)is still valid for any φ_i and reads

$$\sum_e \int_\Omega \left(\partial_t \boldsymbol{u} - \boldsymbol{S}\right) \varphi_i \, dV - \sum_e \int_e \boldsymbol{G}\, \partial_x \varphi_i \, dV + \sum_f \int_f \gamma \left(\boldsymbol{u}^+, \boldsymbol{u}^-; \varphi_i^+, \varphi_i^-; \boldsymbol{n}\right) dS = 0 \tag{4.19}$$

The basis test function chosen here are the Gauss-Lobatto-Legendre (GLL) polynomials. This means that shape functions $\varphi_j(x)$ consist of based on Lagrange interpolants based upon the Lobatto-Legendre quadrature rule control points. An illustration of these GLL polynomials for order 5 and 7 is available in Fig. 4.3. In literature, it is shown that this choice provides a much higher robustness for higher orders of interpolation. As a results,

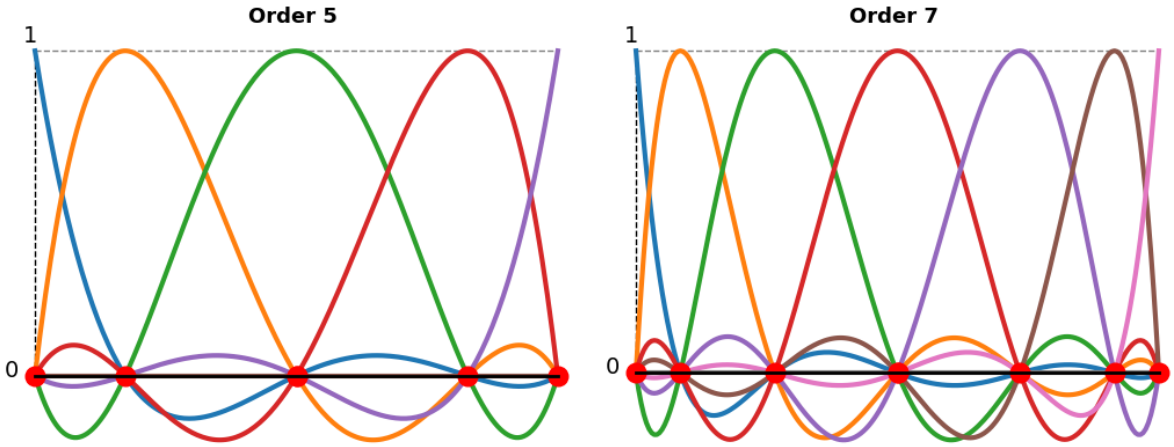

Fig. 4.3: Illustration of the Gauss-Lobatto-Legendre test function of order 5 (on the left) and order 7 (on the right). One can see that all of these polynomials pass by the same control points (denoted by the red dots). In addition to that, they equal 1 only once above of these points.

the approximate solutions coming from these projections can be expressed following:

$$\boldsymbol{u}_h(x) \equiv \sum_{j=1}^{N} \boldsymbol{u}_j \varphi_j(x) \tag{4.20}$$

and then the approximated contributions are found by evaluating their expression with the approximated solution and its gradient

$$\boldsymbol{F}_h(x) \equiv \boldsymbol{F}(u_h(x)) \quad \boldsymbol{D}_h(x) \equiv \boldsymbol{D}(u_h(x), \nabla u_h(x)) \quad \boldsymbol{S}_h(x) \equiv \boldsymbol{S}(u_h(x), \nabla u_h(x)) \tag{4.21}$$

where the subscript h is chosen here to emphasise the difference between the approximated and the true solution. It will be omitted in the next parts of the reports to avoid clutter. This gives rise to the final discretised equations

$$\begin{aligned} \sum_e \int_e \varphi_i \varphi_j \partial_t \boldsymbol{u}_j dV - \sum \int_e \partial_x \varphi_i \left(\boldsymbol{F}_h + \boldsymbol{D}_h\right) dV + \sum_e \int_e \varphi_i \boldsymbol{S}_h dV \\ + \sum_f \int_f \gamma \left(\boldsymbol{u}^+, \boldsymbol{u}^-; \varphi_i^+, \varphi_i^-; \boldsymbol{n}\right) \, dS \end{aligned} \tag{4.22}$$

with e the elements and f the interfaces in the mesh. Since a shape function φ_i is supported on a single element, this further simplifies to the semi-discrete form

$$M_{ij} \partial_t \boldsymbol{u}_j = R_i \tag{4.23}$$

with M_{ij} the mass matrix defined as

$$M_{ij} = \int_e \varphi_i \varphi_j dV \tag{4.24}$$

with e the common element on which both φ_i and φ_j are defined, and $\boldsymbol{R}_i$ the (steady) residual associated to shape function φ_i:

$$\boldsymbol{R}_i = \sum \int_e \partial_x \varphi_i \left(\boldsymbol{F}_h + \boldsymbol{D}_h\right) dV - \sum_e \int_e \varphi_i \boldsymbol{S}_h dV - \sum_f \int_f \gamma \left(\boldsymbol{u}^+, \boldsymbol{u}^-; \varphi_i^+, \varphi_i^-; \boldsymbol{n}\right) \, dS \tag{4.25}$$

This expression can be reformulated as a set of ordinary differential equations for each of the unknowns, by inverting the mass matrix:

$$\partial_t \boldsymbol{u}_i = M_{ij}^{-1} \boldsymbol{R}_j \tag{4.26}$$

The fact that the mass matrix is defined per element allows for its exact inversion. This is one of the advantages of DGM since this inversion is a prerequisite for fully accurate time integration. This equation will be integrated in time using the time integrator discussed in Chapter 5

4.2 Application to the plasma equations

Now that the general formulation of DGM has been established, let us apply this method to the current system of plasma equations. First, the construction of the numerical flux is developed. Then, a presentation of the current application of internal penalty terms is provided. In the last section, a small discussion on the implementation of the ionisation frequency is depicted.

4.2.1 Mapping

In this section, the different terms presented in Eq. (4.1) are particularised here to the isothermal plasma system of equations. Recalling the isothermal plasma system to be discretised

$$\begin{aligned}
&\partial_t n_e + \partial_x \left(n_e u_e\right) && = n_e\, \nu \\
&\partial_t n_i + \partial_x \left(n_i u_i\right) && = n_e\, \nu \\
&\partial_t \left(n_e u_e\right) + \partial_x \left(n_e {u_e}^2 + \varepsilon^{-1} n_e\right) && = \varepsilon^{-1} n_e \partial_x \phi \\
&\partial_t \left(n_i u_i\right) + \partial_x \left(n_i {u_i}^2 + \kappa n_i\right) && = -\, n_i \partial_x \phi \\
&\partial_{xx} \phi && = \chi^{-1} \left(n_e - n_i\right)
\end{aligned} \tag{4.27}$$

one obtains for an element i and unknowns $\boldsymbol{u}_i = \begin{pmatrix} n_e & n_i & n_e u_e & n_i u_i & \phi \end{pmatrix}^T$

$$\boldsymbol{F}_i = \begin{pmatrix} n_e u_e \\ n_i u_i \\ n_e {u_e}^2 + n_e \varepsilon^{-1} \\ n_i {u_i}^2 + n_i \kappa \\ 0 \end{pmatrix} \quad \boldsymbol{D}_i = \begin{pmatrix} 0 \\ 0 \\ 0 \\ 0 \\ \partial_x \phi \end{pmatrix} \quad \boldsymbol{S}_i = \begin{pmatrix} n_e \nu \\ n_e \nu \\ n_e \varepsilon^{-1} \partial_x \phi \\ -n_i \partial_x \phi \\ \chi^{-1} \left(n_e - n_i\right) \end{pmatrix} \tag{4.28}$$

4.2.2 Numerical fluxes

The numerical fluxes $\mathcal{F}^*$ used for this work is the Roe numerical flux [66]. It's construction is developed in this section.

Recalling Eq. (3.4), the hyperbolic part of the plasma equations can be reformulate as

$$\partial_t \boldsymbol{u} + \boldsymbol{A} \partial_x \boldsymbol{u} = \boldsymbol{S} \tag{4.29}$$

where $\boldsymbol{A} = \frac{\partial \boldsymbol{F}}{\partial \boldsymbol{u}}$. The Roe methods is based onto the approximation of the matrix $\boldsymbol{A}(\boldsymbol{u})$ by [1] $\boldsymbol{A}_h(\boldsymbol{u}_L, \boldsymbol{u}_R)$ whose construction has to ensure [52]:

1. *conservativity* with $\boldsymbol{A}_h(\boldsymbol{u}_L, \boldsymbol{u}_R) \left[\boldsymbol{u}_L - \boldsymbol{u}_R\right] = \boldsymbol{F}(\boldsymbol{u}_L) - \boldsymbol{F}(\boldsymbol{u}_R)$
2. *hyperbolicity* of the system with a $\boldsymbol{A}_h$ that has real eigenvalues,
3. *consistency* with $\boldsymbol{A}(\boldsymbol{u}_L, u_R)$ that tends to $\frac{\partial \boldsymbol{F}}{\partial \boldsymbol{u}}(\boldsymbol{u})$ when $\boldsymbol{u}_L, \boldsymbol{u}_R \to \boldsymbol{u}$

It gives a numerical flux that has the expression

$$\mathcal{F}^*(\boldsymbol{u}_L, \boldsymbol{u}_R) = \frac{\boldsymbol{F}(\boldsymbol{u}_L) + \boldsymbol{F}(\boldsymbol{u}_R)}{2} + \left|\boldsymbol{A}_h(\boldsymbol{u}_l, \boldsymbol{u}_r)\right| \left(\boldsymbol{u}_r - \boldsymbol{u}_l\right) \tag{4.30}$$

where the matrix $\left|\boldsymbol{A}_h(\boldsymbol{u}_L, \boldsymbol{u}_R)\right|$ has the same eigenvectors as $\boldsymbol{A}_h$ and has eigenvalues that are the absolute values of the eigenvalues of $\boldsymbol{A}_h$.

[1] For the sake of simplicity, the convention used in section 4.1.1 regarding the value at both side of the interface is replaced by $(\cdot)_{Left}$ and $(\cdot)_{Right}$ in the present section.

Then, if $\bar{\lambda}_i$ and $\bar{\boldsymbol{v}}_i$ are respectively the eigenvalues and eigenvectors of $\boldsymbol{A}_h(\boldsymbol{u}_L, \boldsymbol{u}_R)$, Eq. (4.30) becomes

$$\mathcal{F}^*(\boldsymbol{u}_L, \boldsymbol{u}_R) = \frac{\boldsymbol{F}(\boldsymbol{u}_L) + \boldsymbol{F}(\boldsymbol{u}_R)}{2} - \frac{1}{2}\sum_\alpha a_\alpha \left|\bar{\lambda}_\alpha\right| \bar{\boldsymbol{v}}_\alpha \tag{4.31}$$

The idea proposed by Roe [66] is then to compute $\bar{\lambda}$ and $\bar{\boldsymbol{v}}_i$ as the eigenvalues of the matrix $\boldsymbol{A}_h(\bar{\boldsymbol{u}})$ evaluated at an average states $\bar{\boldsymbol{u}}$, called *Roe's average*.

Following Eq. (3.7), the matrix $\boldsymbol{A}_h(\bar{\boldsymbol{u}})$ is then

$$\boldsymbol{A}_h = \begin{pmatrix} 0 & 0 & 1 & 0 \\ 0 & 0 & 0 & 1 \\ \varepsilon^{-1} - \bar{u}_e^2 & 0 & 2\bar{u}_e & 0 \\ 0 & \kappa - \bar{u}_i^2 & 0 & 2\bar{u}_i \end{pmatrix} \tag{4.32}$$

with

$$\bar{u}_e = \frac{\frac{n_e u_{eL}}{\sqrt{n_{eL}}} + \frac{n_e u_{eR}}{\sqrt{n_{eR}}}}{\sqrt{n_{eL}} + \sqrt{n_{eR}}} \quad \text{and} \quad \bar{u}_i = \frac{\frac{n_i u_{iL}}{\sqrt{n_{iL}}} + \frac{n_i u_{iR}}{\sqrt{n_{iR}}}}{\sqrt{n_{iL}} + \sqrt{n_{iR}}} \tag{4.33}$$

the electron and ions Roe averaged velocities. Analogue eigenvalues and eigenvectors than those found in Eq. (3.8) and (3.9) are retrieved from $\boldsymbol{A}_h$. The eigenvalues are

$$\begin{aligned} \bar{\lambda}_0 &= \bar{u}_e - \sqrt{\varepsilon^{-1}} \\ \bar{\lambda}_1 &= \bar{u}_e + \sqrt{\varepsilon^{-1}} \\ \bar{\lambda}_2 &= \bar{u}_i - \sqrt{\kappa} \\ \bar{\lambda}_3 &= \bar{u}_i + \sqrt{\kappa} \end{aligned} \tag{4.34}$$

for the eigenvectors

$$\begin{aligned} \bar{\boldsymbol{v}}_0 &= \begin{pmatrix} 1 & 0 & \bar{\lambda}_0 & 0 \end{pmatrix} \\ \bar{\boldsymbol{v}}_1 &= \begin{pmatrix} 1 & 0 & \bar{\lambda}_1 & 0 \end{pmatrix} \\ \bar{\boldsymbol{v}}_2 &= \begin{pmatrix} 0 & 1 & 0 & \bar{\lambda}_2 \end{pmatrix} \\ \bar{\boldsymbol{v}}_3 &= \begin{pmatrix} 0 & 1 & 0 & \bar{\lambda}_3 \end{pmatrix} \end{aligned} \tag{4.35}$$

Knowing Eq. (4.30) and (4.31), the jump factors a_α are computed from

$$\frac{1}{2}\sum_\alpha a_\alpha \bar{\boldsymbol{v}}_\alpha = (\boldsymbol{u}_L - \boldsymbol{u}_R) \tag{4.36}$$

so that for each quantities

$$\begin{aligned} a_0 &= \frac{(n_{eR} n_{eL})\,\bar{\lambda}_1 - (n_e u_{eR} - n_e u_{eL})}{2\sqrt{\varepsilon^{-1}}} \\ a_1 &= -\frac{(n_{eR} n_{eL})\,\bar{\lambda}_0 - (n_e u_{eR} - n_e u_{eL})}{2\sqrt{\varepsilon^{-1}}} \\ a_2 &= \frac{(n_{iR} n_{iL})\,\bar{\lambda}_3 - (n_i u_{iR} - n_i u_{iL})}{2\sqrt{\kappa}} \\ a_3 &= -\frac{(n_{iR} n_{iL})\,\bar{\lambda}_1 - (n_i u_{iR} - n_i u_{iL})}{2\sqrt{\kappa}} \end{aligned} \tag{4.37}$$

Injecting Eq. (4.34), (4.35) and (4.37) in Eq. (4.31), gives therefore the following Numerical flux for the plasma convective part

$$\mathcal{F}^* = \frac{\boldsymbol{F}(\boldsymbol{u}_L) + \boldsymbol{F}(\boldsymbol{u}_R)}{2} - \begin{pmatrix} \frac{a_0 \left|\bar{\lambda}_0\right| + a_1 \left|\bar{\lambda}_1\right|}{2} \\ \frac{a_2 \left|\bar{\lambda}_2\right| + a_3 \left|\bar{\lambda}_3\right|}{2} \\ \frac{a_0 \left|\bar{\lambda}_0\right| \bar{\lambda}_0 + a_1 \left|\bar{\lambda}_1\right| \bar{\lambda}_1}{2} \\ \frac{a_2 \left|\bar{\lambda}_2\right| \bar{\lambda}_2 + a_3 \left|\bar{\lambda}_3\right| \bar{\lambda}_3}{2} \end{pmatrix} \tag{4.38}$$

4.2.2.1 Harten entropy fix

It has been shown that the Roe numerical flux may give the wrong answer when velocities approach the sonic point, *i.e.* $|\bar{u}_\alpha| \approx c_\alpha$ [59]. At this point, the Roe lienarisation may lead to solution that is not entropy stable (*i.e.* Eq. (4.14) that is not fulfilled). One solutions is then to add an entropy fix to the numerical flux implementation. Due of its simplicity, an Harten entropy fix [38] is chosen for the current implementation. This fix consists of using a modified eigenvalues $q^H(\bar{\lambda}_\alpha)$ in Eq. (4.31) instead of $\bar{\lambda}_\alpha$, such that

$$q^H(\bar{\lambda}_\alpha) = \begin{cases} \dfrac{(\bar{\lambda}_\alpha)^2}{4\epsilon_k} + \epsilon_k & \text{if } \left|\bar{\lambda}_\alpha\right| < 2\epsilon_k \\ \left|\bar{\lambda}_\alpha\right| & \text{if } \left|\bar{\lambda}_\alpha\right| \geq 2\epsilon_k \end{cases} \tag{4.39}$$

where the parameter ϵ_k is a positive constant value, which Harten suggests to be chosen in the interval $\left(0\,,\,\frac{1}{2}\right)$ [59, 38]. This small fix will ensure that the Roe flux always satisfies Eq. (4.14).

4.2.3 Penalty terms

As presented in section 4.1.3, an internal Penalty method is used for the evaluation of the diffusive interface flux $\gamma^{\boldsymbol{D}}$. In this case, an incomplete interior penalty method (IIPM) (*i.e.* $\theta = 0$) is considered with the choose of σ such that

$$\sigma = \begin{cases} \dfrac{1.001}{2} & \text{if the diffusive tensor } \mathcal{D} \text{ is symmetric} \\ 1.001 & \text{otherwise} \end{cases} \tag{4.40}$$

Consequently, it gives a diffusive interface flux that is expressed as

$$\gamma^d = \sigma[[\varphi]] \cdot [[\boldsymbol{u}]] + [[\varphi]] \cdot \{\{\boldsymbol{D}\}\} \tag{4.41}$$

However, a particular attention has to be paid onto the application of this Galerkin penalty term. Indeed, Eq. (4.28) shows that the diffusive flux $\boldsymbol{D}$ has a non-zero value only for the last equation. For this reason, the penalty will be activated only for the last unknown of each element, and deactivated for the others.

4.2.4 Source term computation

A particular attention has also been paid onto the computation of the Source term $\boldsymbol{S}$. The latter is split in two contributions: a first one accounting for the ionisation processes $\boldsymbol{S}_\nu$ and a second one that refers to the potential interactions between the species momenta and the Poisson's equation $\boldsymbol{S}_\phi$. Mathematically, this means $\boldsymbol{S} = \boldsymbol{S}_\nu + \boldsymbol{S}_\phi$ such that

$$\boldsymbol{S}_\nu = \begin{pmatrix} n_e\nu \\ n_e\nu \\ 0 \\ 0 \\ 0 \end{pmatrix} \quad \text{and} \quad \boldsymbol{S}_\phi = \begin{pmatrix} 0 \\ 0 \\ n_e\varepsilon^{-1}\partial_x\phi \\ -n_i\partial_x\phi \\ \chi^{-1}\left(n_e - n_i\right) \end{pmatrix} \tag{4.42}$$

This split architecture has been used in order to compute the ionisation contribution only when it is necessary. As an example, in the two-stream perturbation test case this term is deactivated since it neglects ionisation effects.

The ionisation frequency ν is computed following Eq. (2.7) where the integral of electron density over the domain has been computed using the Gauss quadrature rule

$$\int_0^L n_e \, dx \approx \left(J_e^G\right)^{-1} \sum_{j=1}^{p} \sum_{i=1}^{\mathcal{N}} w_j n_{ei} \tag{4.43}$$

for a domain composed of $\mathcal{N}$ elements of order p. J_e^G is the geometrical jacobian of an element.

4.3 ForDGe solver

This section describes the DG-FEM solver, called ForDGe, used to solve the plasma equations given in Eq. (2.17). ForDGe is a cartesian adaptive DGM solver. The specificity of this solver is that an immersed approach is used for the geometrical discretisation which eases substantially the mesh generation on complex geometry. Still under development in the Aerospace departmement of the University of Liège, the aims of ForDGe are to provide highly accurate solutions to generic complex physics in complex and evolving geometry (*i.e.* in 3D printing, in topology optimisation).

ForDGe is implemented using C++ programming language and allow multi-thread resolution with the use of OpenMP library. Its architecture is organised around 5 main classes:

- *FMesh class*: This first class regroups all the in formations related to the mesh such as the number of dimension, the domain size in each dimension, the number of elements as well as their interpolation order. It stores these information for each element and reorganise data for efficient interface computation.
- *FConservationLaw class*: As shown in Fig. 4.4, it defines the template in which all the conservation law that are implemented. The derived classes then integrate all

the information in relation to the physics and the types of the considered variables as well as the definition of the fluxes, the initial conditions and the boundary conditions. It also integrates the computation of post-process parameters (*e.g.* pressure, kinetic energy, etc.). In the frame of this work, the *FPlasmaCLaw* and the *FBurgerCLaw* have been implemented. This allows to define all of the finite element and integration operations independently of the specific physics.

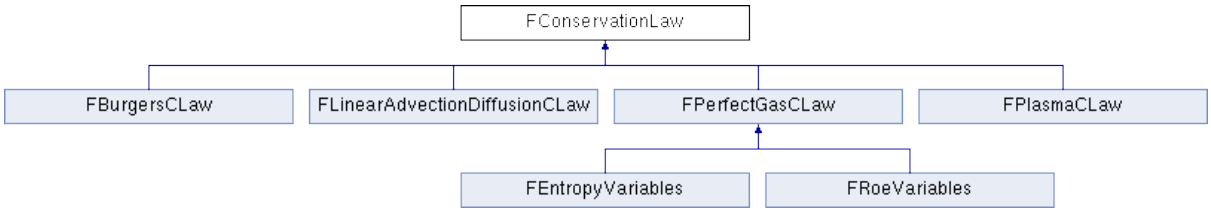

Fig. 4.4: Architecture of the *FConservationLaw* class which accounts for the physics of a given conservation law. For this work, the *FBurgersClaw* and *FPlasmaCLaw* classes have been implemented.

- *FDGBase class*: This third class deals with the DG aspect of the discretisation. It is the basis for all operations that involve the finite element discretisation, including post-processing. Its main function is to support the assembly, and therefore it provides the main functionality to compute the different contributions to the residual. Fig. 4.5 illustrates the different contributions that are considered for the computation of this residual. It is also the class that integrate the IPM strategy presented in section 4.2.3 and make the collocation from the quadrature points to the interpolation ones.

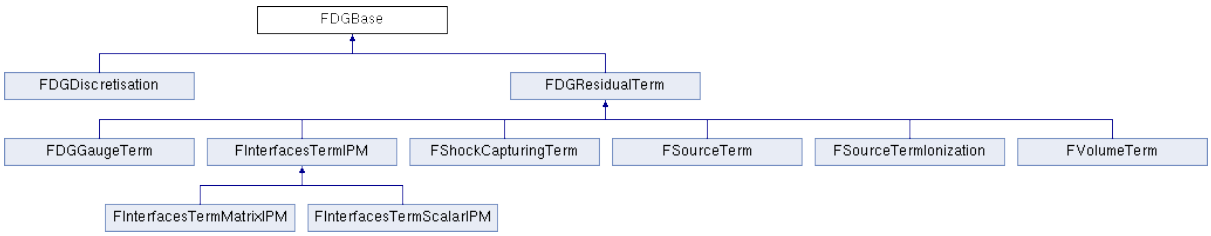

Fig. 4.5: Architecture of the *FDGBase* class which incorporate the DGM formulation in ForDGe. The contribution of *FSourceTerm*, *FSourceTermIonization* and *FDGGaugeTerm* are specific to this work while the shock capturing one is used for another physics.

- The *FIterator* class provides a generic interface for methods that solve a particular steady set of equations, either in the case of steady state solutions, or resulting from the implicit systems that need to be solved during time integration.
- *FTimeIntegrator class*: Finally comes the class that make the time integration of the discretise equation (4.26). At the present states, It allows explicit and implicit time integration. The former based on the fourth-order Runge Kutta (RK4) methods

and latter based on ESDIRK64 or RORK implicit methods[1].

Next to this classes, optimised data structures are available that exploit the structure of the DGM solution by reinterpreting in matrix form as discussed in [39], in view of optimising assembly. In the same vein, a dedicated sparse matrix is implemented.

[1]ESDIRK64 stands for *fourth-order six-stages Explicit first stage, Single Diagonally Implicit Runge-Kutta* and RORK for *Rosenbrock-Runge–Kutta*. For this work, the ESDIRK64 method is used as describe in the next chapter.

Chapter 5

Time discretisation

This chapter presents the time discretisation of the system. In the current work, a *fourth-order Explicit Step, Single Diagonally Implicit Runge-Kutta* (ESDIRK64) scheme is used to carry out the time integration of the coupled Euler-Poisson system. This type of Runge-Kutta (RK) implicit iterator has demonstrated an accuracy that are well suited to match the spatial accuracy of DG methods and exceeds that obtained with classical *Backward Differentiation Formulas* (BDF) methods [3].

It has been shown in the previous chapters that the physics of plasma introduces stringent constraints to the simulation. The stability of the numerical scheme is thereby firstly discussed. By supposing a fixed time step throughout the simulation, this allows us to find a condition on the definition of the time step. Then, the RK family of integrator is presented in a more general before diving into the description of the ESDIRK64 scheme.

5.1 Stability of the numerical scheme

As already mentioned, a fixed time step is used for all the simulation. This parameter plays a key role in the (linear) stability of the explicit time discretisation. In the case of plasma, this stability is mainly restricted by a Courant–Friedrichs–Lewy (CFL) condition that takes into account the scale of the convective characteristic speeds and a condition accounting for the characteristics time scale of the source term [25, 28]. If Δt and Δx denote respectively the time step and the element size, the CFL number is given by

$$CFL = \frac{\Delta t \ |\lambda_{\max}|}{\Delta x} < 1 \tag{5.1}$$

with $|\lambda_{\max}| = \max(\lambda_0, \lambda_1, \lambda_2\lambda_3)$ the maximum propagation speed. Since $\varepsilon \ll \kappa$, a more restrictive CFL condition is found for the electrons than the ions and then $|\lambda_{\max}| = (\lambda_0, \lambda_1)$ in general. In the context of DG methods, Eq. (5.1) is reformulated to take into account the order p of the interpolants. It gives the following condition to the time step [22]

$$CFL = \frac{\Delta t \ |\lambda_{\max}|}{\frac{\Delta x}{2p+1}} < 1 \tag{5.2}$$

Additional constraints come from the source term definition. The first one related to the electrostatic force contribution imposes a stability condition onto the the resolution of the electron plasma period [29]. Mathematically, this means that

$$\Delta t \omega_{p_e} < 1 \tag{5.3}$$

with $\omega_p = \sqrt{\frac{n_e}{\chi \varepsilon}}$. The second constraint comes from the ionisation term that imposes that Δt should be able to capture the characteristic ionisation time. Hence,

$$\Delta t \, \nu < 1 \tag{5.4}$$

From these conditions, the stability of the temporal scheme is ensured if

$$\max\left(CFL\,,\, \Delta t \omega_{p_e}\,,\, \Delta t \nu\right) < 1 \tag{5.5}$$

It has been shown that if Δx does not resolve the Debye length, the most restrictive constraint is the resolution of the electron plasma period [2]. On the other hand, if the Debye length is resolved, one only has to fulfill the convective CFL condition to satisfy $t < \omega_{p_e}^{-1}$. As a consequence, the maximum time step that is allowed ranges

$$\Delta t \simeq \begin{cases} 10^{-6} & \text{in the case of the two-stream perturbation problem} \\ 3.7 \times 10^{-5} & \text{in the case of the plasma sheath problem} \end{cases} \tag{5.6}$$

Although formally the CFL condition determines the linear stability of explicit time integrators, it is also likely to govern the non-linear stability of the implicit time integrators - which are linearly inconditionally stable - since the time integration needs to follow the physics in order to avoid running into unrealistic conditions.

5.2 Runge-kutta integrator

In a general way, the implementation of Runge-Kutta schemes is relatively easy. It starts from the expression of Eq. (4.26)

$$\partial_t u_i = M_{ij}^{-1} \boldsymbol{R}(\boldsymbol{u}_j) \tag{5.7}$$

where $\boldsymbol{R}(\boldsymbol{u}_j)$ is called the residual vector. To avoid clutter, the subscript j is omitted in the rest of the development.

The RK methods integrates Eq. (5.7) from time t_n to t_{n+1} with s intermediate stages following [71]

$$\begin{aligned} \hat{\boldsymbol{u}}^k &= \boldsymbol{u}^n + \Delta t \sum_{j=1}^{s} a_{ij} \partial_t \hat{\boldsymbol{u}}^k = \boldsymbol{u}^n + \Delta t \sum_{j=1}^{s} a_{ij} \boldsymbol{M}^{-1} \boldsymbol{R}(\hat{\boldsymbol{u}}^j)\,, \qquad k = 1, \ldots, s \\ \boldsymbol{u}^{n+1} &= \boldsymbol{u}^n + \Delta t \sum_{j=1}^{k} b_j \boldsymbol{M}^{-1} \boldsymbol{R}(\hat{\boldsymbol{u}}^j) \end{aligned} \tag{5.8}$$

where $\hat{\boldsymbol{u}}^j$ and $\partial_t \hat{\boldsymbol{u}}^j$ represent the approximate solution and time derivative at stage j. The coefficient a_{ij} and bj, called *Butcher coefficients*, are organised in the Butcher tableau $\mathcal{B}$:

$$\mathcal{B} = \begin{array}{c|c} \mathbf{c}^T & \mathbf{A} \\ \hline 0 & \mathbf{b} \end{array} \quad \Rightarrow \quad \begin{array}{c|cccc} 0 & a_{11} & a_{1,2} & \cdots & a_{1s} \\ c_2 & a_{21} & a_{22} & \cdots & a_{2s} \\ \vdots & \vdots & & \ddots & \cdots \\ c_s & a_{s,1} & a_{s,2} & \cdots & a_{s,s} \\ \hline 0 & b_1 & b_2 & \cdots & b_s \end{array} \tag{5.9}$$

In the case of explicit time integration, one hase to considered only the terms a_{ij} that are strictly below the diagonal. A particularisation to the fourth-order explicit RK methods is available in Appendix B. Conversely, for implicit solving, all the values of the Butcher tableau are taken into account. In addition, implicit schemes offer better stability than the explicit ones making those adequate to address stiff problem.

5.3 Single Diagonally Implicit Runge–Kutta methods

The methods used for the time integration of $\boldsymbol{u}$ in this work is the *fourth-order six-stage Explicit first stage, Single Diagonally Implicit Runge-Kutta* (ESDIRK64) scheme. Starting from

$$\partial_t u_i = M_{ij} \boldsymbol{R}(\boldsymbol{u}_j) \tag{5.10}$$

The multistage algorithm is then [71]

$$\begin{aligned} \boldsymbol{u}^0 &= \boldsymbol{u}^n \\ \boldsymbol{u}^s &= \boldsymbol{u}^n - \Delta t \sum_{j=1}^{i} a_{ij} \boldsymbol{M}^{-1} \boldsymbol{R}(\boldsymbol{u}^j) \\ \boldsymbol{u}^{n+1} &= \boldsymbol{u}_h^s \end{aligned} \tag{5.11}$$

For a detailed description of the Butcher tableau associated to this scheme the reader must refer to the appendix of [71]. The first stage is explicit as shown in Eq. (5.18) with the term $\boldsymbol{u}^0 = \boldsymbol{u}^n$. This is due to the fact that the term Butcher coefficient $a_{11} = 0$ in this methods. Conversely, the last stage updates the solution at the next time. Between these two terms, the scheme is composed of s non-linear problems that has to be solved numerically.

The system of s non-linear equations is solved using a classical Newton-Raphson approach [62]. If one considers the non-linear system $\boldsymbol{B}(\boldsymbol{u})$, such methods permit to solve numerically

$$\boldsymbol{B}(\boldsymbol{u}) = \boldsymbol{0} \tag{5.12}$$

by expanding $\boldsymbol{B}$ using a Taylor series around a certain value $\boldsymbol{u}_0$ (called *intial guess vector*) so that

$$\boldsymbol{B}(\boldsymbol{u}) \simeq \boldsymbol{u_0} + \frac{\partial \boldsymbol{B}}{\partial \boldsymbol{u}}(\boldsymbol{u}_0)\,(\boldsymbol{u} - \boldsymbol{u}_0) \tag{5.13}$$

For this method, the derivative $\frac{\partial \boldsymbol{B}}{\partial \boldsymbol{u}}(\boldsymbol{u}_0)$, called *Jacobian* formally needs computing for each stage. However, by design all diagonal coefficients a_{ii} are the same, such that the Jacobian is the same for all stages, and therefore usually computed only at the first stage. Only if the convergence rate of the Newton algorithm between stages j and $j+1$ is above a given tolerance, it is deemed that the solution has changed too much for the Jacobian still to be relevant. In practice, the Jacobian can even be kept over several time steps. Mathematically, the conditions for updating the Jacobian, used in ForDGe, read

$$\frac{\|\Delta \boldsymbol{u}_{j+1}\|_2}{\|\Delta \boldsymbol{u}_j\|_2} > tol_j \quad \text{and} \quad n\Delta t > 10 \tag{5.14}$$

As a result, one has to determine the jacobian $\frac{\partial \boldsymbol{B}}{\partial \boldsymbol{u}}(\boldsymbol{u}_0)$. In the present work, the nonlinear system to be solved is

$$\boldsymbol{B} \equiv \boldsymbol{u}^s - \boldsymbol{u}^n + \Delta t \sum_{k=1}^{i} a_{ik} \boldsymbol{M}^{-1} \boldsymbol{R}(\boldsymbol{u}^k) \tag{5.15}$$

where the residual vector $\boldsymbol{R}$ is expressed as

$$\boldsymbol{R}_i = \sum \int_e \partial_x \varphi_i \left(\boldsymbol{F}_h + \boldsymbol{D}_h\right) dV - \sum_e \int_e \varphi_i \boldsymbol{S}_h \, dV - \sum_f \int_f \gamma \left(\boldsymbol{u}^+, \boldsymbol{u}^-; \varphi_i^+, \varphi_i^-; \boldsymbol{n}\right) dS \tag{5.16}$$

This means that the jacobian of each term of Eq. (5.16) has to be computed.

5.3.1 Treatment of the potential equation

Due to the absence of temporal derivative in the Poisson's equation

$$\partial_{xx}\phi = \chi^{-1}\left(n_e - n_i\right) \tag{5.17}$$

the potential equation cannot formally be integrated in time along-with the transports equations using ESDIRK64, but would be solved separately at each subtime step. Usually, it is done using a two-step strategy, meaning that the temporal scheme first solves the system of transport equations and then solves the instantaneous Poisson's equation. Before passing to the next time, this back and forth resolution at a time t_i is kept until the convergence of the results.

A different approach is used in this work and consists in a modification of the classical ESDIRK64 scheme to solve both the time integration and the potential equation in a fully coupled fashion. It is done in practice by treating the potential equation in the same way as the particle equations, whilst deactivating the inertial term associated to the last unknown (ϕ) in the implicit integrator. Practically, it consists of reformulating Eq. (5.18) as

$$\begin{aligned} \boldsymbol{u}^0 &= \boldsymbol{\beta} \boldsymbol{u}^n \\ \boldsymbol{u}^s &= \boldsymbol{\beta} \boldsymbol{u}^n - \Delta t \sum_{j=1}^{i} a_{ij} \boldsymbol{R}(\boldsymbol{u}^j) \\ \boldsymbol{u}^{n+1} &= \boldsymbol{\beta} \boldsymbol{u}_h^s \end{aligned} \tag{5.18}$$

with

$$\boldsymbol{\beta} = \begin{pmatrix} 1 \\ 1 \\ 1 \\ 1 \\ 0 \end{pmatrix} \tag{5.19}$$

The same procedure is applied onto the diagonal elements of the jacobian matrix (*i.e.* $\boldsymbol{\beta}\,\mathrm{diag}\left(\frac{\partial \boldsymbol{B}}{\partial \boldsymbol{u}}\right)$).

This modification made onto the classical implementation of ESDIRK64 permits to treats the Poisson's equation alongside the particles equations during the Newton iterator, enhancing its convergence.

5.4 Linearisation

A linearisation of the Jacobian matrix is carried out to prevent the need of defining and encoding all the different analytical expressions of the Jacobian. A a result, the different first order derivatives that compose $\frac{\partial \boldsymbol{B}}{\partial \boldsymbol{u}}$ are evaluated following a central difference method

$$\frac{\partial \boldsymbol{B}}{\partial \boldsymbol{u}} \approx \frac{\boldsymbol{B}(\boldsymbol{u}+\epsilon) - \boldsymbol{B}(\boldsymbol{u}-\epsilon)}{2\epsilon} \tag{5.20}$$

where the perturbation parameter ϵ is chosen to be proportional to the $\mathbb{L}_2$ norm of the solution. In order to provide a perturbation halfway the precision of the computation, the square root of the machine precision is used (as given by the C++ `std::numeric_limits<FDTYPE>::epsilon`).

5.4.1 Treatment of the ionisation frequency

A particular attention is paid to the evaluation of the Jacobian associated to the Source term $\boldsymbol{S}$. Following the reasoning given in section 4.2.4, the Jacobian matrix $\boldsymbol{J}_S$ is split in two contributions: one from the ionisation $\boldsymbol{J}_{\boldsymbol{S}_\nu}$ and one from the potential interactions between the particles momenta and the Poisson's equation $\boldsymbol{J}_{\boldsymbol{S}_\phi}$. Mathematically, this means

$$\boldsymbol{J}_{\boldsymbol{S}} = \boldsymbol{J}_{\boldsymbol{S}_\nu} + \boldsymbol{J}_{\boldsymbol{S}_\phi} \tag{5.21}$$

For $\boldsymbol{J}_{\boldsymbol{S}_\phi}$ the linearisation procedure described in the previous section is used, while for $\boldsymbol{J}_{\boldsymbol{S}_\nu}$, the ionisation frequency ν is assumed to be constant at each time step. The latter prevents a global coupling of the system after passing into the linearisation. Indeed, since the ionisation frequency is computed via integrals on the whole domain ν, using an exact linearisation as before Eq. (2.7) will results in a full matrix, which would have significant impact on the practical implementation.

The analytical expression of $\boldsymbol{J}_{\boldsymbol{S}_\nu}$ is hence used for this contribution, this reads

$$\boldsymbol{J}_{\boldsymbol{S}_\nu} = \begin{pmatrix} \nu & 0 & 0 & 0 & 0 \\ 0 & \nu & 0 & 0 & 0 \\ 0 & 0 & 0 & 0 & 0 \\ 0 & 0 & 0 & 0 & 0 \\ 0 & 0 & 0 & 0 & 0 \end{pmatrix} \tag{5.22}$$

Part III

Results

Chapter 6

Preliminary work : the Burgers' equation

In this chapter, a brief detour from the theory of plasma is taken to present a preliminary study carried out onto the Burgers' equation. This chapter is therefore presented as a self-consistent chapter in which the unidimensional Burgers' model is developed from scratch.

As one of the few "canonical" nonlinear Partial Differential Equations (PDE) which can be solved analytically for an arbitrary initial condition [41], the Burgers' equation appears often as a *toy model* and a mandatory passage to understand some of the inside behaviour of general nonlinear systems. Indeed, it combines the effect of two prior topics namely: the nonlinear advection that tends to introduce discontinuous shocks and the diffusion law that tends to smooth them away. The former phenomenon occurs even if the initial condition is smooth making Burgers' equation a proper model for testing numerical algorithms in flows where severe gradients or shocks are anticipated [67, 58].

This chapter is segmented into three parts: first, the Burgers' model is described by considering both inviscid and complete formulation. Then, the discretisation using DG-FEM is briefly presented with a discussion on the numerical fluxes. Finally, three numerical experiments are considered to analyse its numerical solution.

6.1 Burgers model

The *one-dimensional Burgers' equation* as firstly introduced by J.M. Burgers [12] and H. Bateman [4] is the quasi-linear parabolic PDE

$$\partial_t u + u\,\partial_x - \nu\,\partial_{xx} u = 0 \tag{6.1}$$

in which the velocity $u(x,t)$ is the dependent variable and ν the fluid viscosity. The operators ∂_t and ∂_x denote, respectively, the temporal and spatial differentiation.

In the case of fluids with negligible viscosity, the last term of Eq. (6.1) vanishes leading to

$$\partial_t u + u\,\partial_x u = 0 \tag{6.2}$$

which corresponds to the *one-dimensional Inviscid Burgers' Equation.*

6.1.1 Inviscid case

The 1D inviscid Burgers equation is the scalar non-linear advection equation given by Eq. (6.2). This formulation without any viscosity-dispersion term represents a purely hyperbolic PDE [40].

The main feature of Eq. (6.2) is the formation of *shocks*, which are discontinuities that may appear after a certain finite time and then regularly propagate within the domain. This induces significant difficulties in the computation of Burgers' solution for which the Reynolds number $\mathrm{Re} = \frac{u\,L}{\nu} \to \infty$, corresponding to steep wavefronts. In many cases, the numerical solution produces results with large unphysical oscillations near the discontinuity.

Plenty of exact solution exist for the Burgers' equation depending on the method used (see *e.g.* [5]). One way is to use the Characteristics method which for an initial $u(\xi, 0) = F(\xi)$ gives the solution

$$\left.\begin{aligned} u(x,t) &= F(\xi) \\ \xi &= x - u\,t \end{aligned}\right\} \qquad t \geq 0 \tag{6.3}$$

In addition, the conservative form of Eq. (6.2) reads

$$\partial_t + \partial_x \left(\frac{u^2}{2}\right) = 0 \tag{6.4}$$

that can be reformulated in the following to highlight the scalar hyperbolic flux $f(u)$

$$\partial_t u + \partial_x \left[f(u)\right] = 0 \tag{6.5}$$

with $f(u) = \frac{u^2}{2}$ and appears as a quadratic function of u. A *weak solution* of the following equation can be defined. In other words, if $u(x,t)$ is a smooth solution of Eq. (6.4) in the domain Ω, and $\varphi(x,t)$ is a infinitely smooth function that vanishes on the boundary of Ω, then $\iint_\Omega \left[\partial_t + \left(\frac{u^2}{2}\right)_x\right] \varphi\, dx\, dt = 0$ becomes after integrating by parts

$$\iint_\Omega \left[u\,\partial_t\varphi + \tfrac{u^2}{2}\,\partial_x\varphi\right] dx\, dt = 0 \tag{6.6}$$

This equation admits a weak solution to Eq. (6.4) defined as a function of $u(x,t)$, not necessarily continuous, that satisfies Eq. (6.6) for all Ω and φ.

Suppose now that there is a discontinuity at the position $x = s(t)$ so that the left and right value follows $u_L(x,t) < \dot{s}(t) < u_R(x,t)$, one solution of Eq. (6.6) is the Rankine-Hugoniot jump condition [61, 42]

$$\dot{s} = \frac{f(u_R) - f(u_L)}{u_R - u_L} = \frac{\frac{{u_R}^2}{2} - \frac{{u_L}^2}{2}}{u_R - u_L} = \frac{1}{2}(u_L + u_R) \tag{6.7}$$

describing the speed of the propagating discontinuity.

Although Eq. (6.7) gives a solution to Eq. (6.6) in the presence of discontinuity, it does not guarantee the solution uniqueness. As a consequence, an additional condition must be imposed to eliminate non-physical weak solutions, called the *Entropy condition*. It yields that a discontinuity propagating with speed $\dot{s}$ is permitted only if $f'(u_R) > s > f'(u_L)$. This additional condition translates the fact that a fluid passing a shock or a discontinuity must increase in entropy.

6.1.2 Viscous case

When the fluid viscosity is non-negligible, the full one-dimensional Burgers' equation problem reads [41]

$$\begin{cases} \partial_t u + u\,\partial_x u - \nu\,\partial_{xx} u = 0 \\ u(x,0) = u_0(x) \end{cases} \tag{6.8}$$

representing one of the simplest non-linear advection-diffusion problem and a parabolic scheme [40].

Unlike the inviscid case, the last term introduces dispersion into the system so that the discontinuity that may appear is smoothed out. A smooth exact solution of the problem exposed in Eq. (6.8) is available and has been derived by Cole [23] and Hopf [41], giving the following expression:

$$u(x,t) = \frac{\displaystyle\int_{-\infty}^{+\infty} \frac{x-y}{t} \exp\left[-\frac{(x-y)^2}{4\nu t} - \frac{1}{2\nu}\int_0^y u(\xi,0)\,d\xi\right] dy}{\displaystyle\int_{-\infty}^{+\infty} \exp\left[-\frac{(x-y)^2}{4\nu t} - \frac{1}{2\nu}\int_0^y u(\xi,0)\,d\xi\right] dy} \tag{6.9}$$

6.2 Numerical implementation

This section presents the DG-FEM applied to the one-dimensional Burgers' equation. In its conservative form, the Burgers' convection-diffusion problem reduces to

$$\partial_t \boldsymbol{u} + \partial_x \boldsymbol{F} + \partial_x \boldsymbol{D} = 0 \tag{6.10}$$

where $\boldsymbol{F}(u,x,t)$ is the convective flux and $\boldsymbol{D}(u,\nabla u,x,t)$ is the diffusive flux. In the present case, no source terms were considered. Recalling section 4.1, a particular attention has to be paid on the definition of these two contributions. For example, one has to choose an appropriate numerical flux that accommodates the entropy stability of the system.

6.2.1 Convective term

As introduced in the previous section, the convective flux $\boldsymbol{F}$ is a quadratic function of u

$$\boldsymbol{F} = \frac{u^2}{2} \tag{6.11}$$

To ensure that the entropy condition of the solution is satisfied at the discontinuity, and hence the entropy stability, many techniques have been developed. They can be divided into two categories: the first one consists of adding some numerical diffusion operators in the expression of $\boldsymbol{F}$, by introducing Lax-Friedrichs type or Roe type fluxes to an entropy conservative flux [43, 16, 32, 13]. The second one uses the entropy stability of upwind numerical fluxes [19]. In this preliminary work, the former method is used following the work of Ismael & Roe [43], because it permits better control of the amount of entropy introduced in the system. The following formulation of the *entropy-stable* (ES) interface flux has been implemented

$$\mathcal{F}^* = \frac{1}{6}\left({u_L}^2 + u_L u_R + {u_R}^2\right) - \underbrace{\frac{1}{4}\left|u_L + u_R\right|\left(u_R - u_L\right)}_{\text{Lax-Friedrichs type flux}} \tag{6.12}$$

where $(\cdot)_L$ and $(\cdot)_R$ denote the value at the left and right position of the interface respectively. It provides a scheme that is entropy-conservative and has a net production of entropy using a Lax-Friedrichs type flux, ensuring the entropy stability.

However, it has been shown that the entropy produced by the Lax-Friedrichs flux is not large enough. At the position of the shock, it should be $O\left(\left[\frac{u_L+u_R}{2}\right]^3\right)$. Ismail & Roe [43] propose to add an entropy production term to equation (6.12) to obtain the *entropy-consistent* (EC) flux, yielding

$$\mathcal{F}^* = \frac{1}{6}\left({u_L}^2 + u_L u_R + {u_R}^2\right) - \frac{1}{4}\left|u_L + u_R\right|\left(u_R - u_L\right) - \frac{\left|u_R - u_L\right|\left(u_R - u_L\right)}{12} \tag{6.13}$$

The first term is therefore entropy conserving, the second term enforces entropy stability and the third term yields entropy production of $O\left(\left[\frac{u_L+u_R}{2}\right]^3\right)$.

6.2.2 Diffusive flux

The diffusion part of the Burger's equation can be treated as the classical linear-diffusion problem. The diffusion flux is then expressed as a function of the velocity gradient $\nabla u(x,t)$ using the Fick's laws of diffusion [31]. The diffusion volume flux $\boldsymbol{D}$ and interface flux $\gamma^{\boldsymbol{D}}$ are thereby

$$\mathbf{D} = -\nu\,\nabla u \quad \text{and} \quad \gamma^{\boldsymbol{D}} = -\nu\,\nabla u \tag{6.14}$$

6.3 Numerical experiments

In this section some numerical experiments specific to the Burgers equation are reported depicting the different behaviours of the Burgers' numerical solution. For all experiments, Gauss–Lobatto–Legendre (GLL) interpolating functions proposed in section 4.1.4 are used to limit as much as possible the appearance of numerical oscillations at discontinuity locations. Periodic boundary conditions are considered. A Fourth-order Runge Kutta integrator is used for all the expermients meaning that a CFL condition lower than 1 is imposed to ensure the numerical stability of the solution.

First, the inviscid case is investigated through the study of a sine wave propagation problem and a Riemann problem. The aim of this part will be the comparison of the different entropy fix strategy proposed in the previous section. After that, the complete Burgers (*i.e.* viscous) model is presented through a wave propagation test case.

6.3.1 Inviscid Wave propagation

Let us consider as first test case the smooth initial condition from [33]

$$u(x,0) = \frac{1}{2\pi\, t_s}\, \sin\left(2\pi\, x\right) \tag{6.15}$$

where t_s is the breaking time from which shock appears. With its contribution to Eq. (6.15) as a scaling parameter, this breaking time will permit to monitor the shock appearance. A value of $t_s = 1$ sec is used for this study. The associated exact solution is then computed using Characteristics method and is

$$u(x,t) = \frac{1}{2\pi\, t_s}\, \sin\Big(2\pi\, \left[x - u(x,t)\, t\right]\Big), \quad t > 0 \tag{6.16}$$

A comparison of the results found using ES and EC schemes in the case of 10 and 11 elements of order 6 are presented in Fig. 6.1 for a simulation time $t = 0.9$ sec and Fig. 6.2 for a time $t = 1.4$ sec.

In the case of smooth results (*i.e.* before the shock appearance), Fig. 6.1 shows a good fit of the results for both ES and EC schemes even if the number of elements is even or odd. In contrast, Fig. 6.2 exhibits a clear improvement of the solution by using EC flux on 10 elements. Spurious oscillations are seen for the ES scheme demonstrating insufficient production of entropy through the shock. This shows the benefit of adding entropy production term.

However, oscillations remain in the EC scheme when considering an odd number of elements (*i.e.* 11 elements). In this case, the centre of the domain is aligned with the centre of an element. These troubles come from the fully regular hypothesis of the shape function inside the element which can not handle a flow discontinuity at its centre. As a consequence, this function exhibits strong oscillations. This problematic can be solved by implementing shock capturing methods (see *e.g.* [72]). Because the purpose of this chapter is more to understand the inside behaviour of a nonlinear model, such techniques are not covered here. One may note some small oscillations starting in the smooth case

(see Fig. 6.1) around $x = 0.5$ which come from the same phenomenon. In Fig. 6.2, this phenomenon was not seen in the even configuration (at least, for the EC scheme) because the flow discontinuity coincides perfectly with an element's interface where it is allowed by the DG-FEM.

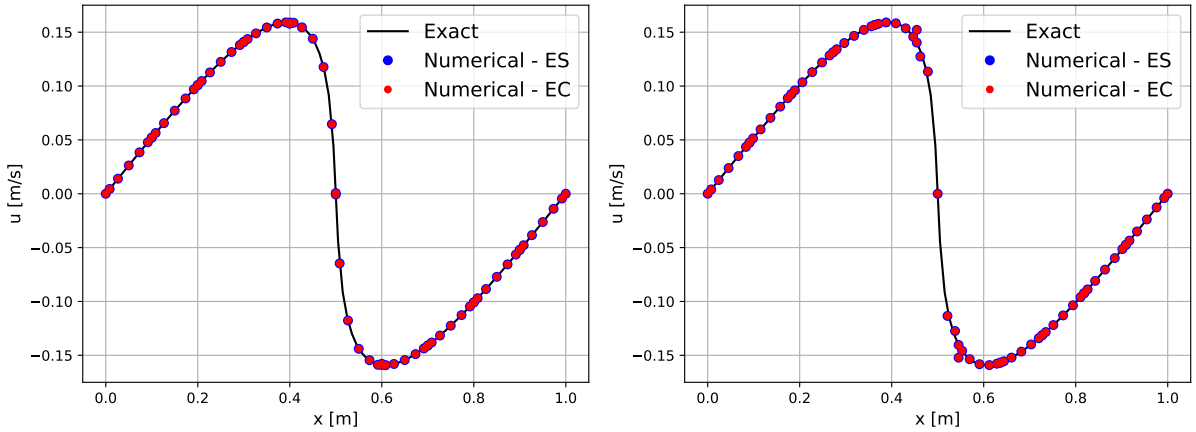

(a) 10 elements (b) 11 elements

Fig. 6.1: Solution at time $t = 0.9$ sec with ES flux (in blue) and EC flux (in red).

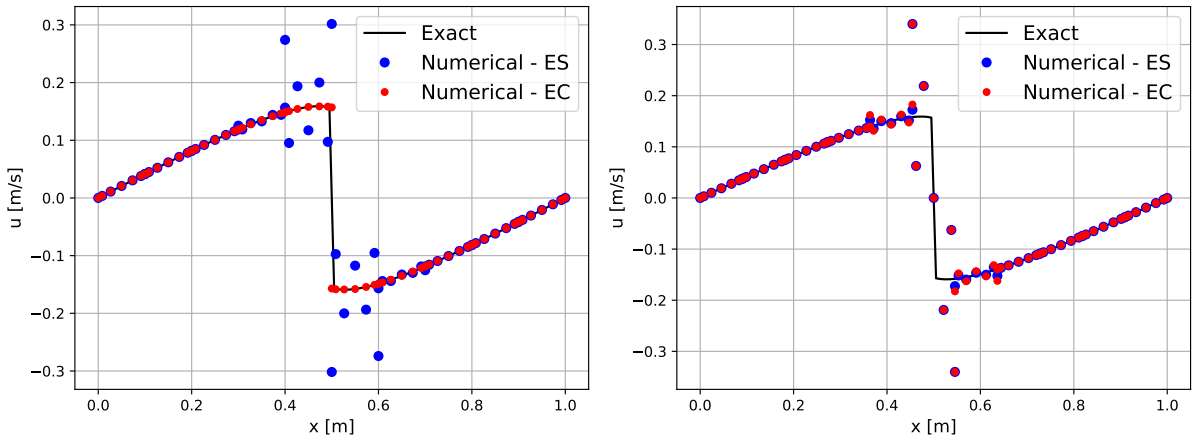

(a) 10 elements (b) 11 elements

Fig. 6.2: Solution at time $t = 1.4$ sec with ES flux (in blue) and EC flux (in red).

6.3.2 Inviscid Riemann problem - Rarefaction with stationary shock

Let us consider now the following initial value problem [43, 49]

$$u(x,0) = \begin{cases} -1 & \text{if } \frac{1}{3} \leq |x| \leq 1 \\ 1 & \text{if } |x| < \frac{1}{3} \end{cases} \tag{6.17}$$

which is computed until time $t = 0.32$ sec. This step-like initial condition will evolve into a rarefaction fan on the left side while on the right side will remain a stationary shock [43]. The exact solution to this problem is [49]

$$u(x,t) = \begin{cases} -1 & -\infty < x < b_1 \\ -1 + 2\frac{x-b_1}{b_2-b_1} & b_1 < x < b_2 \\ 1 & b_2 < x < b_{\text{shock}} \\ -1 & b_{\text{shock}} < x < +\infty \end{cases} \tag{6.18}$$

where

$$b_1 = -\frac{1}{3} - t, \quad b_2 = -\frac{1}{3} + t \quad \text{and} \quad b_{\text{shock}} = \frac{1}{3} \tag{6.19}$$

A comparison between the results obtained by Ismail & Roe [43] who uses a first-order Finite Volume Methods scheme, the exact solution and the proposed model is made in Fig 6.3, considering both ES flux (on the left) and EC flux (on the right). As in [43]. A domain composed of 40 equally spaced elements of order 1 with periodic boundary conditions is considered. The numerical solution is evaluated at time $t = 0.32$ sec for which a CFL number of 0.8 was prescribed.

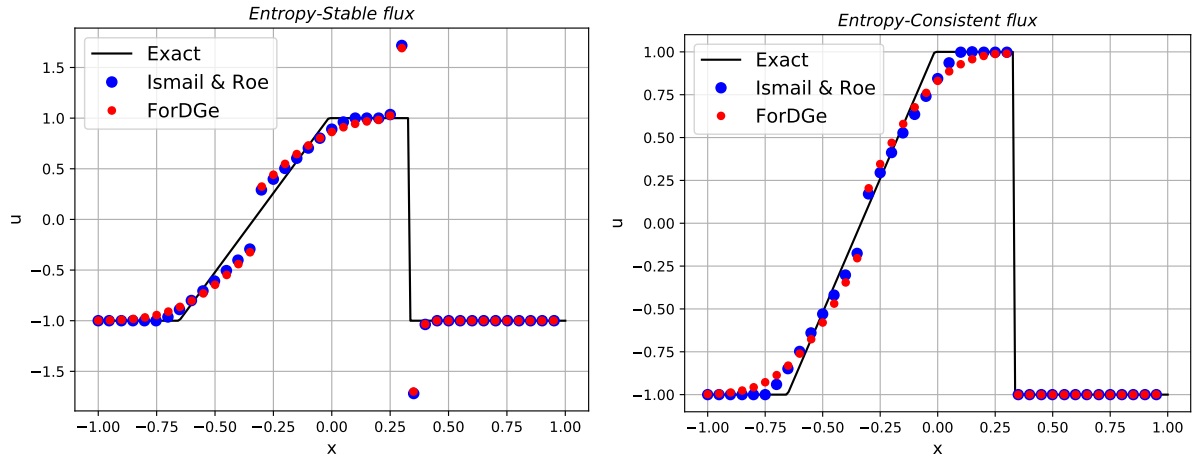

(a) Entropy stable flux

(b) Entropy consistent flux

Fig. 6.3: Rieman problem at time $t = 0.3$ sec, $N = 40$, order $k = 0$ and CFL $= 0.8$. The numerical results of ForDGe (in red) are compared with reference ones (in blue) [43].

Fig. 6.3 shows results that are very similar to those proposed by Ismail & Roe [43]. On the left, the same spurious oscillations are generated near the shock by the ES flux, demonstrating not enough entropy produced across the shock. On the right, it can be seen that adding the entropy consistency term removes these spurious oscillations and provides extra smoothing in the rarefaction fan. One may note some small discrepancies between the results at the extremities of this part. One may also note that the rarefaction remains under-resolved with the EC term. At order 0, one way of improvement is to use a second-order Total Variation Diminishing (TVD) method (see e.g. [43]). Another one is to go to higher-order as proposed in Fig. 6.4. Even if a better resolution of the rarefaction is seen, spurious oscillations appear again near the shock for both flux types and start to develop at the rarefaction extremities.

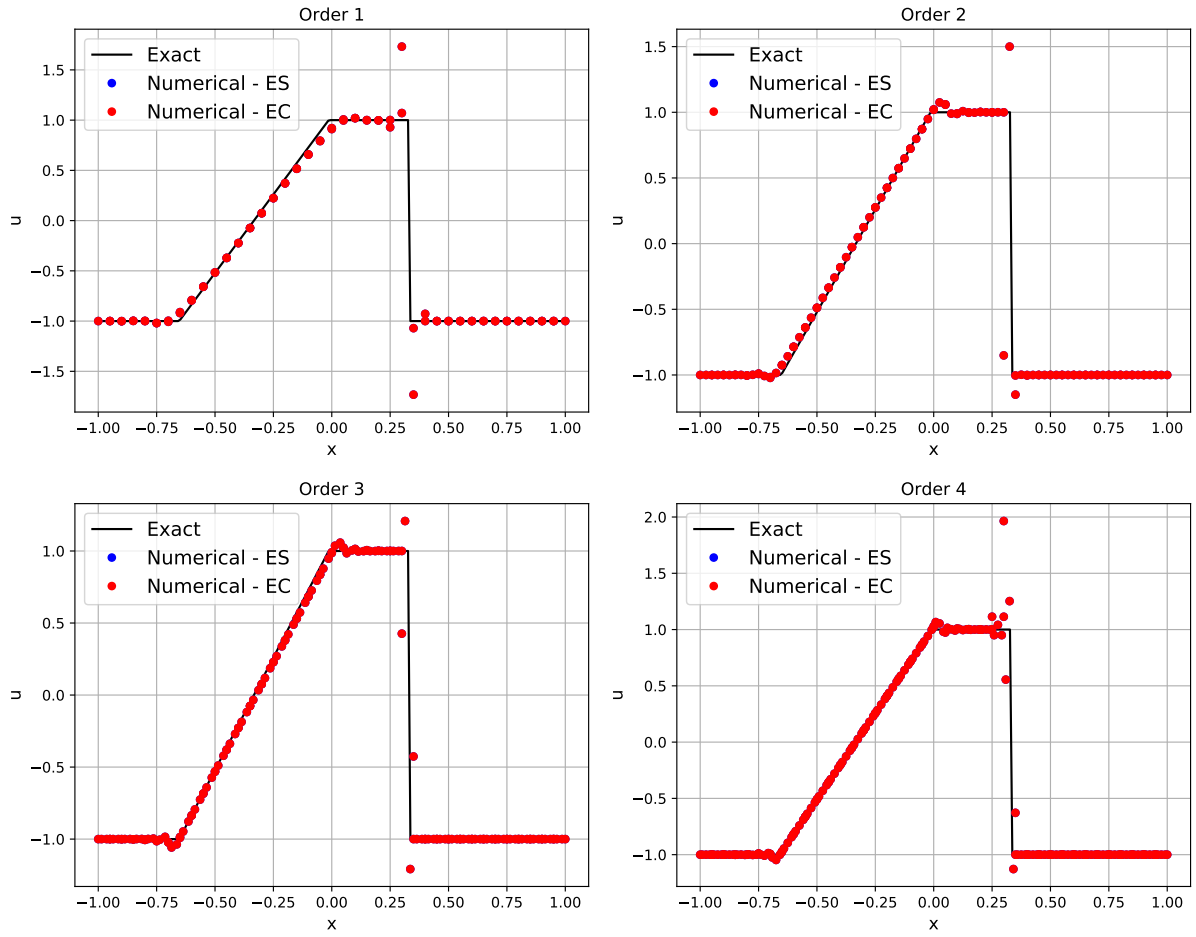

Fig. 6.4: Rieman problem at time $t = 0.32$ sec, $N = 40$ cells, order $k = 1, 2, 3, 4$ and CFL $= 0.8$. The results found with ES flux (in blue) are compared with those found with EC flux (in red)

6.3.3 Viscous Wave propagation

The full Burgers' equation is then tested using the same sine wave initial condition presented in Eq. (6.15) with a breaking time $t_s = 1$ sec. The exact solution is computed following Eq. (6.9) based on Cole-Hopf transformation [41]. Its expression is recalled here for convenience

$$u(x,t) = \frac{\int_{-\infty}^{+\infty} \frac{x-y}{t} \exp\left[-\frac{(x-y)^2}{4\nu t} - \frac{1}{2\nu}\int_0^y u(\xi,0)\,d\xi\right] dy}{\int_{-\infty}^{+\infty} \exp\left[-\frac{(x-y)^2}{4\nu t} - \frac{1}{2\nu}\int_0^y u(\xi,0)\,d\xi\right] dy} \tag{6.20}$$

The numerical solution obtained for this wave propagation is availabe in Fig. 6.5 for a simulation time $t = 0.9$ sec and in Fig. 6.6 for a simulation time $t = 1.4$ sec. In each of these figures, a comparison between the configuration with 10 equally spaced elements of order 6 and 11 equally spaced elements of order 6 is depicted in which *Entropy-consistent* (EC) fluxes are used. The fluid viscosity ν is also varied giving a comparison between the results for $\nu = 0.001$, 0.005 and 0.008.

As in the inviscid case, good fit of the exact solution is performed by the numerical results at $t = 0.9$ sec for both even and odd number of elements. On the other hand, the discontinuity encountered for the inviscid sine wave at time $t = 1.4$ sec (*cfr.* Fig. 6.2) is smoothed out by the adding viscosity. The spurious oscillations that were seen when considering an odd number of element (*i.e.* 11 elements) are also removed by the viscous term so that the results follow quite well the analytical one after the breaking time. However, one may notice that, for $\nu = 0.001$, some discrepancies are still observed between the numerical and exact solutions with some point grouped in "cluster" near $x = 0.5$.

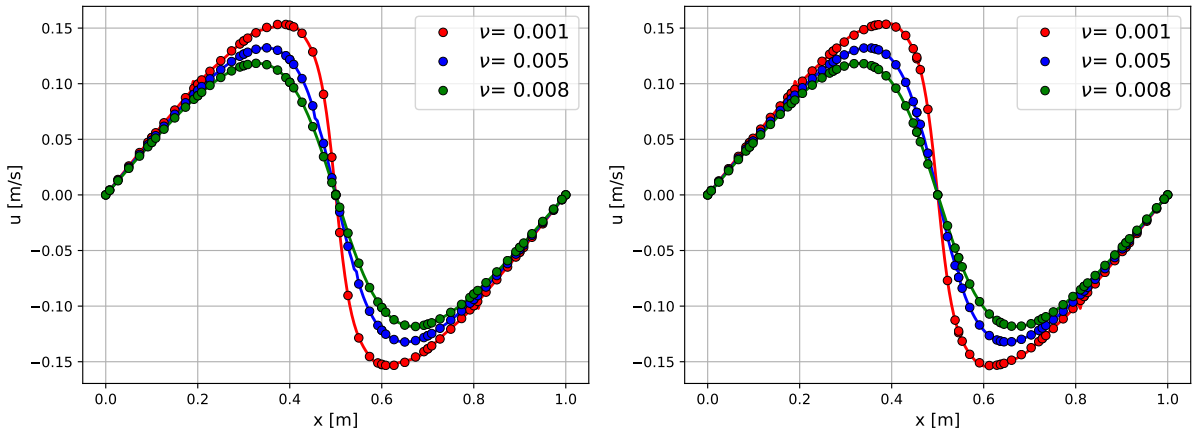

(a) 10 elements (b) 11 elements

Fig. 6.5: Viscous sine wave numerical results (dots) and analytical solutions (solid line) at time $t = 0.9$ sec, order 6, and fluid viscosity $\nu = 0.001, 0.005, 0.008$ using EC flux.

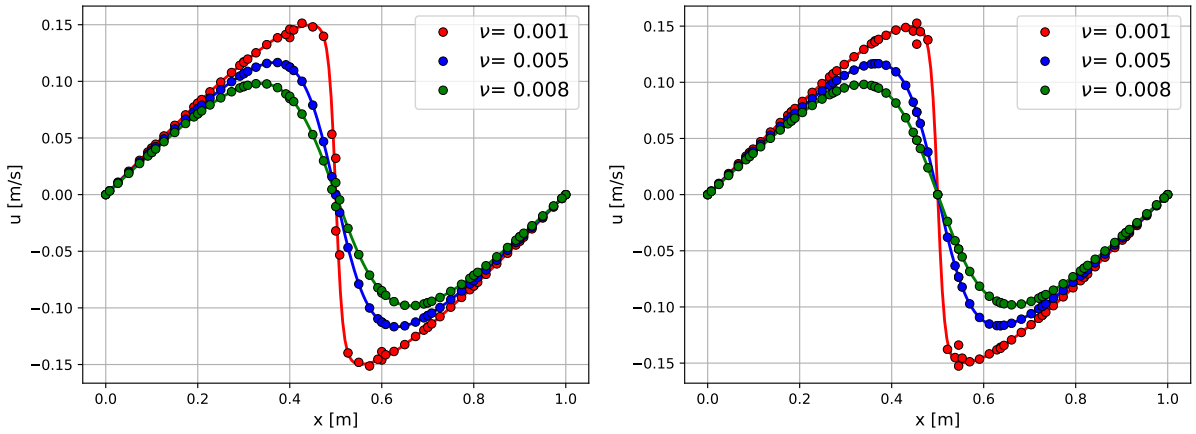

(a) 10 elements (b) 11 elements

Fig. 6.6: Viscous sine wave numerical results (dots) and exact solutions (solid line) at time $t = 1.4$ sec, order 6, and fluid viscosity $\nu = 0.001, 0.005, 0.008$ using EC flux.

Chapter 7

Propagation of a two-stream periodic perturbation

In order to prove that the discretisation has been properly done, the propagation of a two-stream instability in a low-temperature collisionless plasma is performed. This case has been widely used in the past for convergence study of the two-fluid plasma system as in the work of Crispel *et al.*[27, 26] which assumed the isentropic law, or the work of Alvarez Laguna *et al.* [2] for isothermal plasma as in the current work.

7.1 Problem set up

For this test case, the two-fluid Euler-Poisson equations given in Eq. (2.17) is used for the simulation where the ionisation processes involved in the density source terms are assumed to be negligible. However, the impact of the potential gradient is still considered for the momentum source terms. The following system of equations is then solved:

$$\begin{aligned}
&\partial_t n_e + \partial_x \left(n_e u_e\right) && = 0 \\
&\partial_t n_i + \partial_x \left(n_i u_i\right) && = 0 \\
&\partial_t \left(n_e u_e\right) + \partial_x \left(n_e {u_e}^2 + n_e \varepsilon^{-1}\right) && = n_e \varepsilon^{-1} \partial_x \phi \\
&\partial_t \left(n_i u_i\right) + \partial_x \left(n_i {u_i}^2 + n_i \kappa\right) && = -n_i \partial_x \phi \\
&\partial_{xx} \phi && = \chi^{-1} \left(n_e - n_i\right)
\end{aligned} \tag{7.1}$$

The goal of this case is to simulate a two stream instability that occurs in a uniform quasi-neutral plasma of density n_0 when there is a relative velocity u_0 between the electrons and the ions [18]. The advantage of the two-stream perturbation is that an analytical solution in the form of a sine wave is available [27, 26]. This solution takes the form of a sine wave of frequency ω and wavelength k. A detailed derivation of this analytical solution is available in Appendix C.

In this problem, thermal plasma is considered, so that $\kappa = 1$. The electron-to-mass ratio is $\varepsilon = 10^{-4}$. The domain length is set to 1 and contains 10^4 Debye lengths, *i.e.* $\lambda = \sqrt{\chi} = 10^{-4}$. Periodic boundary conditions are applied. The background plasma has a normalised density $n_0 = 1$ and an electrons velocity of $u_0 = 1$. The latter corresponds to the Bohm's speed at these conditions. Under these conditions, if the wavelength of the perturbation is fixed to $k = 2\pi$, the dispersion relation [14] (see Appendix C.1 for a derivation)

$$F(k,\omega) \equiv \alpha_4\omega^4 + \alpha_3\omega^3 + \alpha_2\omega^2 + \alpha_1\omega + \alpha_0 = 0 \tag{7.2}$$

with

$$\begin{gathered}\alpha_4 = \varepsilon\chi, \qquad \alpha_3 = -2\varepsilon\chi k u_0, \qquad \alpha_2 = \left(\varepsilon k^2\chi\left(u_0^2 - \kappa\right) - \varepsilon n_0 - k^2\chi - n_0\right) \\ \alpha_1 = 2\left(k^2\kappa\chi + n_0\right)\varepsilon k u_0 \quad \text{and} \quad \alpha_0 = -\varepsilon k^2 u_0^2 n_0 - \varepsilon\chi k^4\kappa u_0^2 + k^4\kappa\chi + k^2 n_0\left(\kappa + 1\right)\end{gathered} \tag{7.3}$$

reveals four real values, meaning the perturbation is stable [2]. For this problem, we choose the solution $\omega = 8.885726989$. From this result, the initial fields reads

$$\begin{aligned} n_e(x,0) &= 1 + 2.41425\times10^{-2}\sin\left(2\pi x\right) \\ n_i(x,0) &= 1 + 2.41425\times10^{-2}\sin\left(2\pi x\right) \\ n_e u_e(x,0) &= \left[1 + 2.41425\times10^{-2}\sin\left(2\pi x\right)\right]\left[1 + 10^{-2}\sin\left(2\pi x\right)\right] \\ n_i u_i(x,0) &= \left[1 + 2.41425\times10^{-2}\sin\left(2\pi x\right)\right]\left[3.41425\times10^{-2}\sin\left(2\pi x\right)\right] \\ \phi(x,0) &= 2.41421\times10^{-2}\sin\left(2\pi x\right) \end{aligned} \tag{7.4}$$

7.2 Numerical results

The solution obtained with the ESDIRK64 scheme on 20 equally spaced elements of order 4 and a $\Delta t = 7.0713\times10^{-7}$ sec, and compared with the analytical one is available in Fig. 7.1. The solution obtained with an explicit fourth-order Runge-Kutta (RK4) scheme is also provided (see Appendix B for more detail on the method). Since the latter does not solve for the Poisson's equation, the analytical solution of the potential gradient that reads

$$\partial_x\phi = 4.82842\pi\times10^{-2}\cos\left(2\pi x - 8.885726989t\right) \tag{7.5}$$

is imposed onto the momentum source terms at each time step. The solutions presented are in good agreement with the reference solution except the electron momentum in the explicit case. Several causes can be stated such as the lack of spatial resolution, the low-Mach regime of electrons that induces nonphysical results from the Roe numerical flux, or the fact that this oscillation might be a transient component of the flow which is damped in time.

For the first two causes, a solution with a higher spatial resolution may be helpful. Fig. 7.2 shows the solution obtained at $t = 1$ sec with 50, 100 and 300 elements of order 5, a $\Delta t = 7.0713\times10^{-7}$ sec and RK4 scheme. No matter how high the spatial resolution of the problem is, the same solution is obtained. Similarly, the solution obtained at 3 different higher time is depicted in Fig. 7.3. The spurious oscillation that travels the electron momentum is still visible at much larger time $t = 1$ sec.

N. Corthouts [24] encountered a similar problem in his M.Sc. thesis in which only the electrons/ions transport equations have been solved with the same analytical expression of the potential gradient as the one given in Eq. (7.5). From his results, he has concluded that it could come either from an instability of the system, nor from the very low-mach regime of the electrons. Since no correction for low-mach numbers was implement in the current implicit resolution, these oscillations can be addressed to the use of an explicit time integration that does not solve for the potential. Indeed, in the implicit resolution, the Fully coupled system is solved in one go. The potential can then adapt its value to counter act the electron momentum fluctuation leading to a results that follow better the reference.

The solution obtained after a large simulation time ($t = 0.7071$ sec) is available in Fig. 7.4. A discrepancy develops between the reference and the implicit results with the sine peaks that lightly come to each other. Several causes can be addressed:

1. A lack of consistency in the implementation of the Roe's numerical flux for low-mach regime may show difficulties in resolving the non-linear system of Euler-Poisson equations. The development of advanced numerical strategy that correct this features for low-mach conditions is then let for future work.

2. This nonlinear behaviour may have been simply ignored in the computation of the reference solution. Indeed, linear Fourier analysis was used for its determination (see Appendix C). In the future, one should develop new strategies to find this analytical solution that is consistent with the non-linear behaviour of the equations.

Fig. 7.5 shows simulation carried out with the ESDIRK64 scheme with a much larger time step, $\Delta t = 1.4142 \times 10^{-4}$ sec and 20 elements of order 4. Similar results as the one obtain in Fig. 7.1 are obtained despite not resolving the plasma electron period, $\Delta t \gg \omega_{p_e}^{-1} = 10^{-6}$. It shows therefore the increased stability of implicit schemes and the benefit in term of computation cost.

Finally, the convergence study of the $\mathbb{L}_2$ error norm is presented in Fig. 7.6. For this, the number of element as well as the interpolant order is varied and the $\mathbb{L}_2$ norm of the absolute error between the numerical and the analytical results are computed following

$$\mathbb{L}_2 = \sqrt{\sum_{j=1}^{N} \left|\left| \boldsymbol{u}_j - \boldsymbol{u}_j^* \right|\right|^2} \tag{7.6}$$

where $\boldsymbol{u}_j$ and $\boldsymbol{u}_j^*$ are respectively the numerical and reference solutions at point j, and N is the total number of points. The simuation is $t = 0.057$ sec and a time step of 1.4142×10^-7 sec is used. It can be seen that the $\mathbb{L}_2$ decreases as long as the domain is refined. Moreover, one can retrieve the interpolant order from the slope of this curve. However, all the values converge toward a constant error around 10^{-5}. One cause could be the non-linearity explained above. Indeed, this shifting of value tends to introduce a biase in the evaluation of the $\mathbb{L}_2$. An other cause would be the the fact that the error

associated to the time integration starts to be dominant again. As a result, one would have to decrease even more the time step.

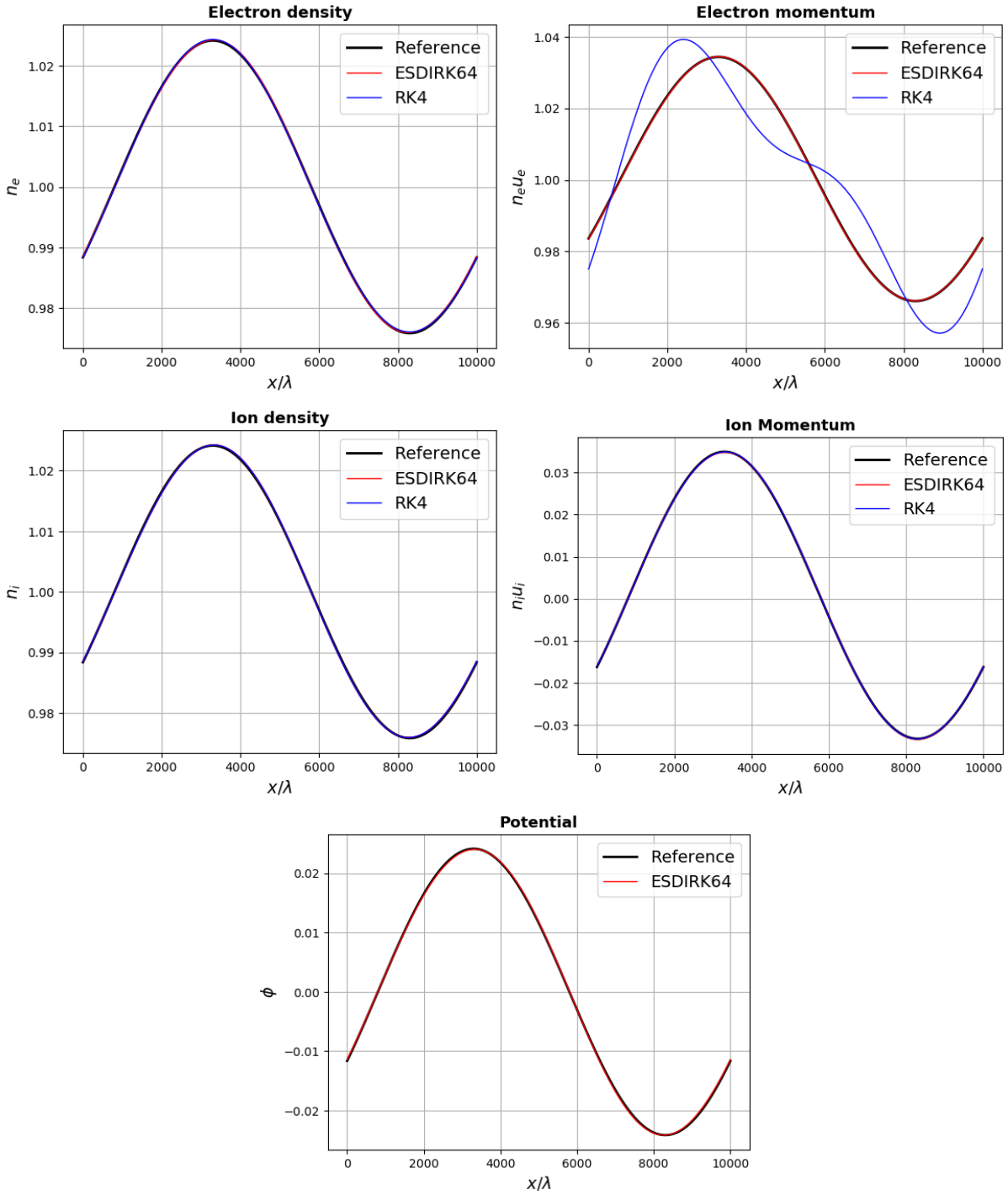

Fig. 7.1: Comparison of the analytical solution of the two-stream perturbation and the solution obtained with an explicit RK4 scheme and an fully implicit ESDIRK64 scheme at time $t = 0.057$sec using 20 equally spaced elements of order 4 and $\Delta t = 7.0713 \times 10^{-7}$sec. For the potential, only the solution provided by the ESDIRK64 method is presented since the RK4 does not solve for the potential.

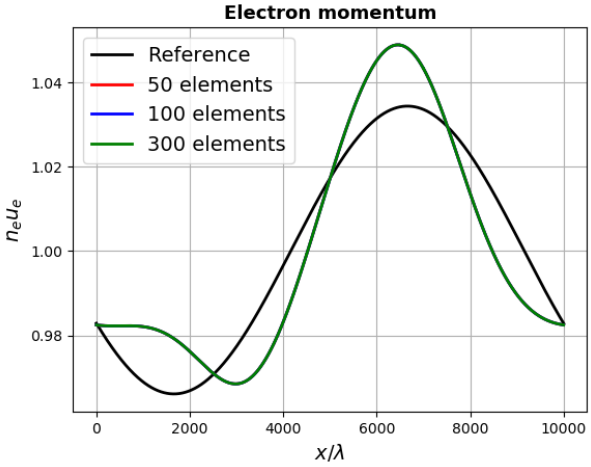

Fig. 7.2: Comparison of electron momenta obtained in the reference solution and with an explicit RK4 scheme at time $t = 1$ sec using 50, 100 and 300 equally spaced elements of order 5 for a $\Delta t = 7.0713 \times 10^{-7}$ sec. The solution does not change when increasing the spatial resolution.

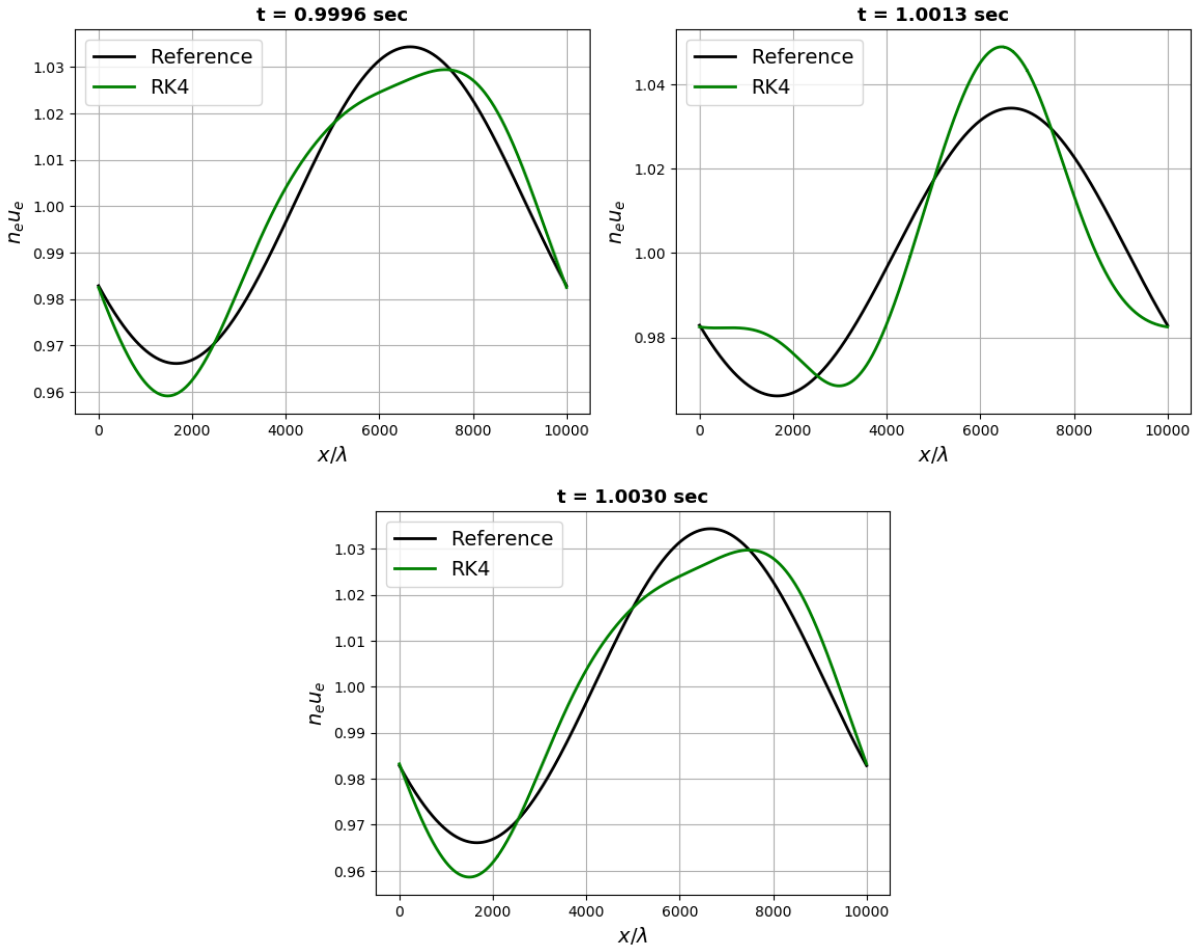

Fig. 7.3: Numerical electron momenta obtained with an explicit RK4 scheme, $\Delta t = 7.0713 \times 10^{-7}$ sec and 300 equally spaced elements of order 5 at three different times: $t = 0.996$ sec, $t = 1.0013$ sec and $t = 1.0030$. Spurious oscillations are still visible in the solution.

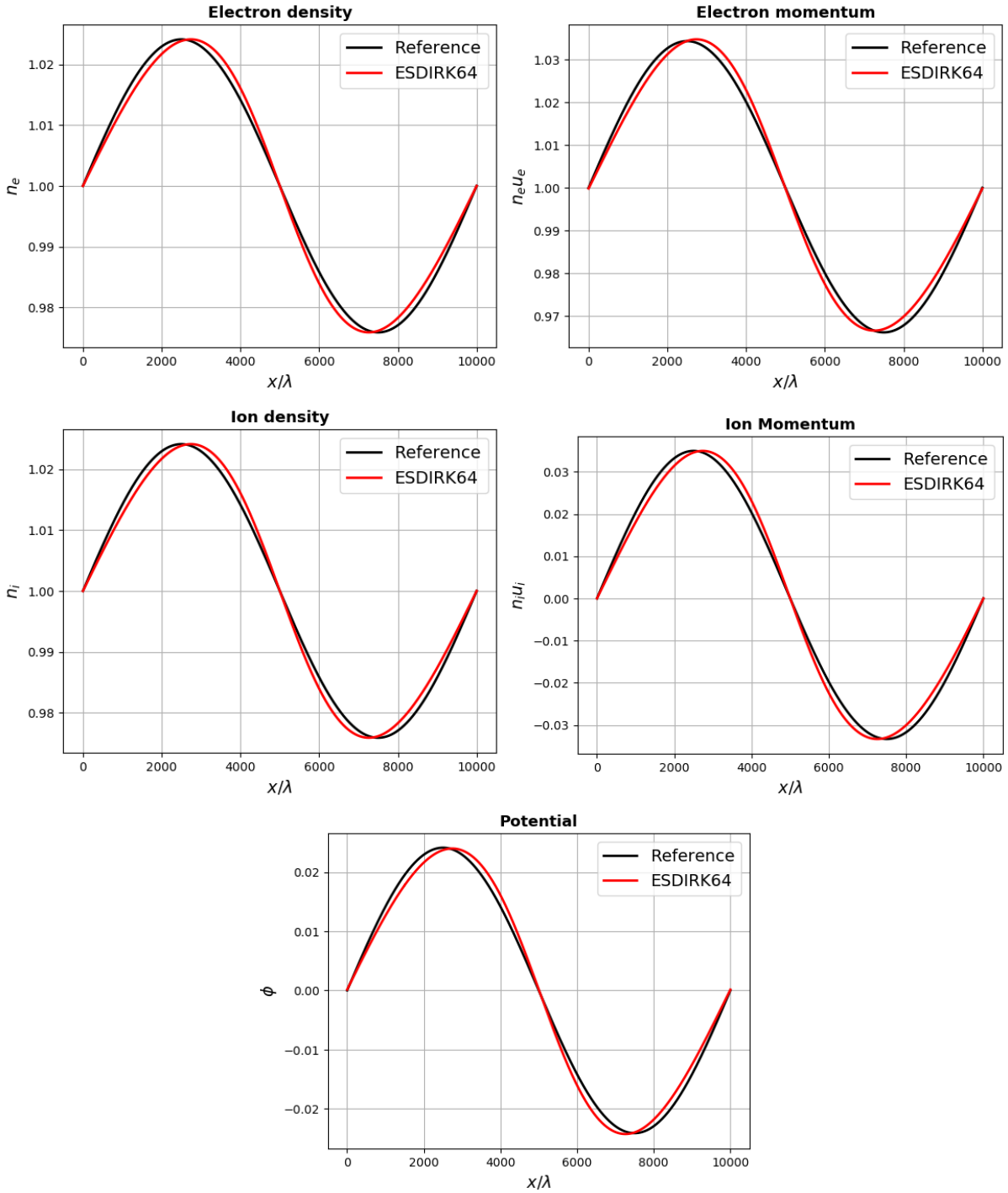

Fig. 7.4: Comparison of the analytical solution of the two-stream perturbation and the solution obtained with a fully implicit ESDIRK64 scheme at time $t = 0.7170$sec using 20 equally spaced elements of order 4 and $\Delta t = 7.0713 \times 10^{-7}$sec. A discrepancy appears between the two solutions with the peaks of the waves that come to each other.

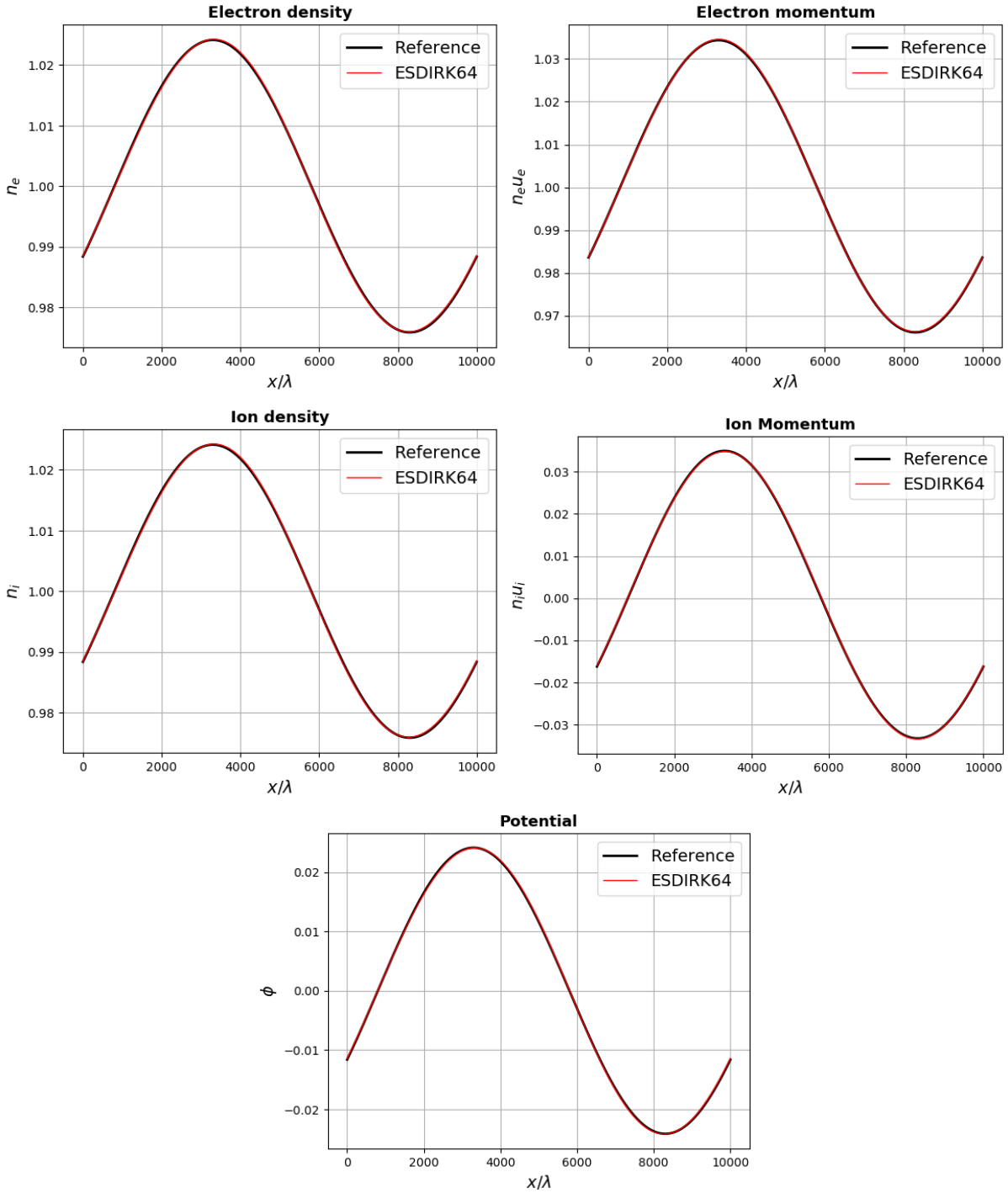

Fig. 7.5: Comparison of the analytical solution of the two-stream perturbation and the solution obtained with a fully implicit ESDIRK64 scheme at time $t = 0.057$ sec using 20 equally spaced elements of order 4 and $\Delta t = 7.0713 \times 10^{-4}$sec. Despite $\Delta t \gg \omega_{p_e} = 10^{-6}$, results are still in good agreement with the reference solution.

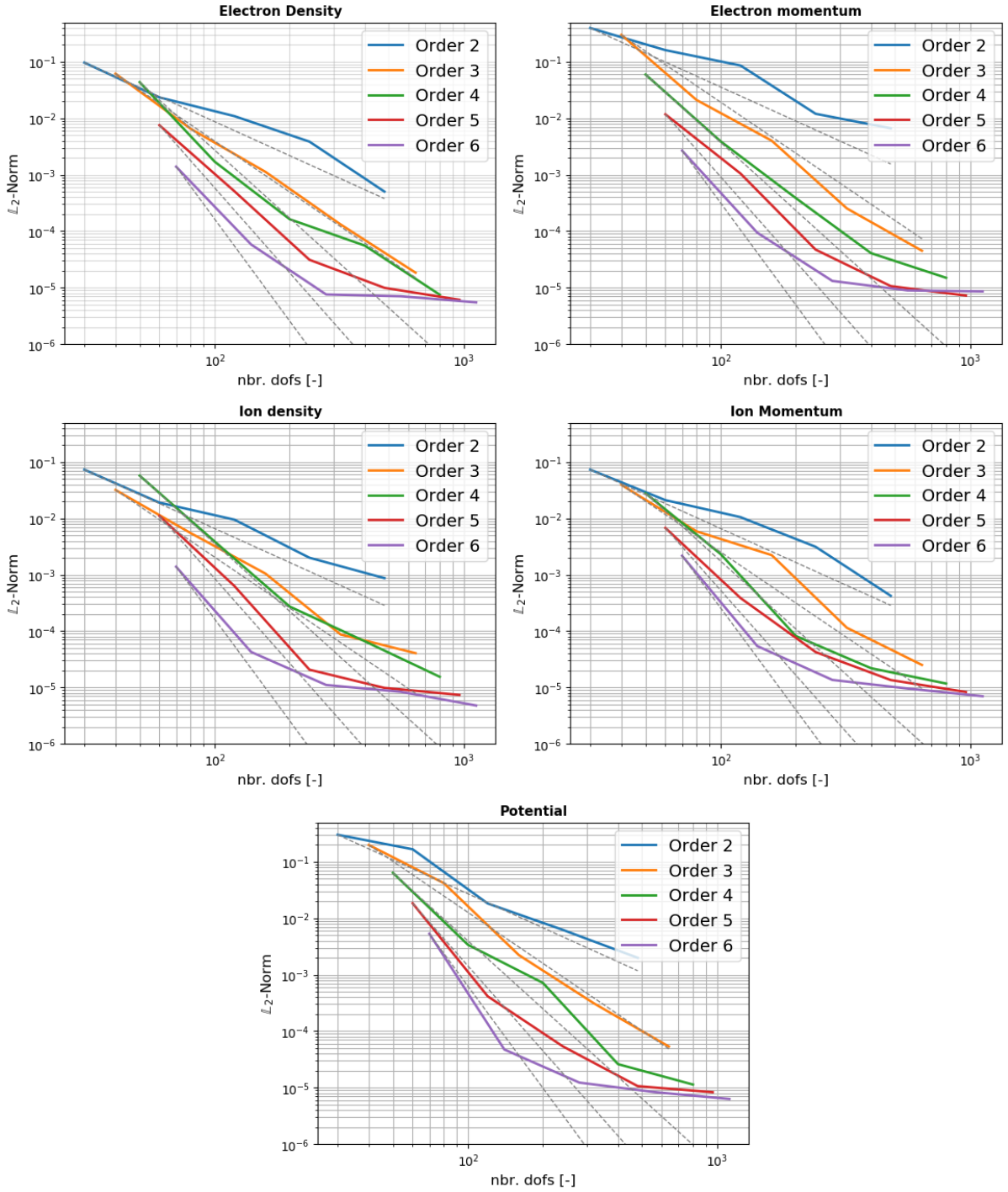

Fig. 7.6: Mesh convergence study of the numerical solution to the two-stream perturbation obtained with an implicit ESDIRK64 scheme and for different orders and 10, 20, 40, 80 and 160 equally spaced elements. The evolution of the $\mathbb{L}_2$ norm reflect relatively well the order of interpolant used. However, all the error seems to converge to a fixed value of $\sim 10^{-5}$.

Chapter 8

Plasma sheath problem

This chapter presents the results obtained during the simulation of the complete plasma sheath model. The problem set up is recalled and the different numerical results are discussed.

8.1 Problem set up

The problem consists of a one-dimensional low-temperature isothermal plasma confined inside a cylinder with equipotential walls. The equations to be solved here are the complete two-Fluid model, whose formulation is given by

$$\begin{aligned}
\partial_t n_e + \partial_x \left(n_e u_e\right) &= n_e\, \nu \\
\partial_t n_i + \partial_x \left(n_i u_i\right) &= n_e\, \nu \\
\partial_t \left(n_e u_e\right) + \partial_x \left(n_e {u_e}^2 + n_e \varepsilon^{-1}\right) &= n_e \varepsilon^{-1} \partial_x \phi \\
\partial_t \left(n_i u_i\right) + \partial_x \left(n_i {u_i}^2 + n_i \kappa\right) &= -\, n_i \partial_x \phi \\
\partial_{xx} \phi &= \chi^{-1} \left(n_e - n_i\right)
\end{aligned} \tag{8.1}$$

The boundary conditions described in section 2.3 are chosen and an ionisation rate ν that counter balance the ions flux that leaves the domain is computed at each time step following [2]

$$\nu = \frac{|n_i u_i(x=0,t)| + |n_i u_i(x=L,0)|}{\int_0^L n_e(x,t)\, dx} \tag{8.2}$$

A collisionless Argon+ plasma discharge that has the properties described in table 2.2 is considered here [14]. Its electron-to-ion mass ratio is $\varepsilon = 1.36 \times 10^{-5}$, its ion-to-electron temperature ratio is $\kappa = 0.025$ and the non-dimensional Debye length is set to $\lambda = \sqrt{\chi} = 10^{-2}$. At the beginning, a quasi-neutral plasma of number density n_0 at rest and with no potential is assumed in the discharge leading to the following initial field

$$\begin{cases} n_e(x,0) = n_i(x,0) = n_0 \\ n_e u_e(x,0) = n_i u_i(x,0) = \phi(x,0) = 0 \end{cases} \tag{8.3}$$

The idea is then to let run the simulation until a steady state is reached. In this work, this steady state solutions will be assessed when the relative difference in the solution $\mathbb{L}_2$ norm is under a given tolerance. In this work, an arbitrary relative tolerance of 10^{-5} is considered. Mathematically, these stopping conditions reads

$$\frac{\left|\mathbb{L}_2\left[\boldsymbol{u}_j^{n+1}\right] - \mathbb{L}_2\left[\boldsymbol{u}_j^{n}\right]\right|}{\mathbb{L}_2\left[\boldsymbol{u}_j^{n}\right]} < 10^{-5} \tag{8.4}$$

where the $\boldsymbol{u}_j^n$ and $\boldsymbol{u}_j^{n+1}$ are respectively the solution obtained at two successive times t_n and t_{n+1}.

8.2 Numerical results

A comparison between the reference solution of Alvarez Laguna *et al.*[2] and the solution obtained with the current implementation is available in Fig. 8.1. A simulation carried out on 100 equally spaced elements of order 4 with the modified ESDIRK64 time intregator for a time step $\Delta t = 1.5 \times 10^{-5}$ sec is then presented. The final time is $t = 2$ sec and is steady regarding Eq. (8.4). The obtained results are in strong agreement with the references ones, and capture perfectly the formation of the sheath. The quasi-neutrality violation is observed within it as well as the steep potential gradient at the beginning of the presheath. Moreover, the value of the potential drop at the presheath ϕ_p and from the presheath to the wall ϕ_W must follow the expression derived by Lieberman *et al.*[54] (given in dimensional units)

$$\phi_p = -\frac{\mathrm{k_B} T_e}{2e} \qquad \phi_W = -\frac{\mathrm{k_B} T_e}{e} \ln\left(\frac{m_i}{2\pi m_e}\right)^{1/2} \tag{8.5}$$

This gives the following expression for the total drop from the bulk to the wall

$$\Delta\phi = \phi_p + \phi_W \simeq -5.187 \tag{8.6}$$

in the case of Argon+ discharge. As shown in Fig. 8.1, this value is well estimated by the numerical solver.

To assess that the proposed solution has reached a steady state, the time evolution of the relative difference of the solution $\mathbb{L}_2$ norm between two successive time is presented in Fig. 8.2 for the same conditions. Regarding the condition established in Eq. (8.4), the steady state can be ensure. However, this steady solution required a subsequent computational effort to be reached by classical time integration. To give an example, to reach the current solution more than 133333 time iterations have been needed. One must keep in mind that, for each of these iteration, a set of nonlinear equations is solved several times and multiple loops are conducted to ensure the convergence of the Newton methods. As a consequence, a proper alternative that can be the base for future works, would be to solve directly the coupled plasma system in steady state solution through a steady Newton method. This would help to save a lot of computation effort.

Finally, the sheath width is determined by the use of the Bohm criterion [8] which states that ions must enters the sheath at given velocity u_B, called the Bohm speed, whose expression is recalled:

$$u_B = \sqrt{\frac{\mathrm{k_B} T_e}{m_i}} \tag{8.7}$$

For this purpose, the velocity scaled by u_B is displayed in Fig. 8.2. Following convention the sheath edge extends till the distance at which this scaled velocity is equal to 1. From this criterion, a sheath width of $8.09\lambda$is found for the current configuration, which follows quite well the theoretical results [64, 65]. Indeed, if one consider the density left wall of Fig. 8.1, below a distance $x \approx 8\lambda$ the electrons and ions starts to have different number densities violating the quasi-neutrality

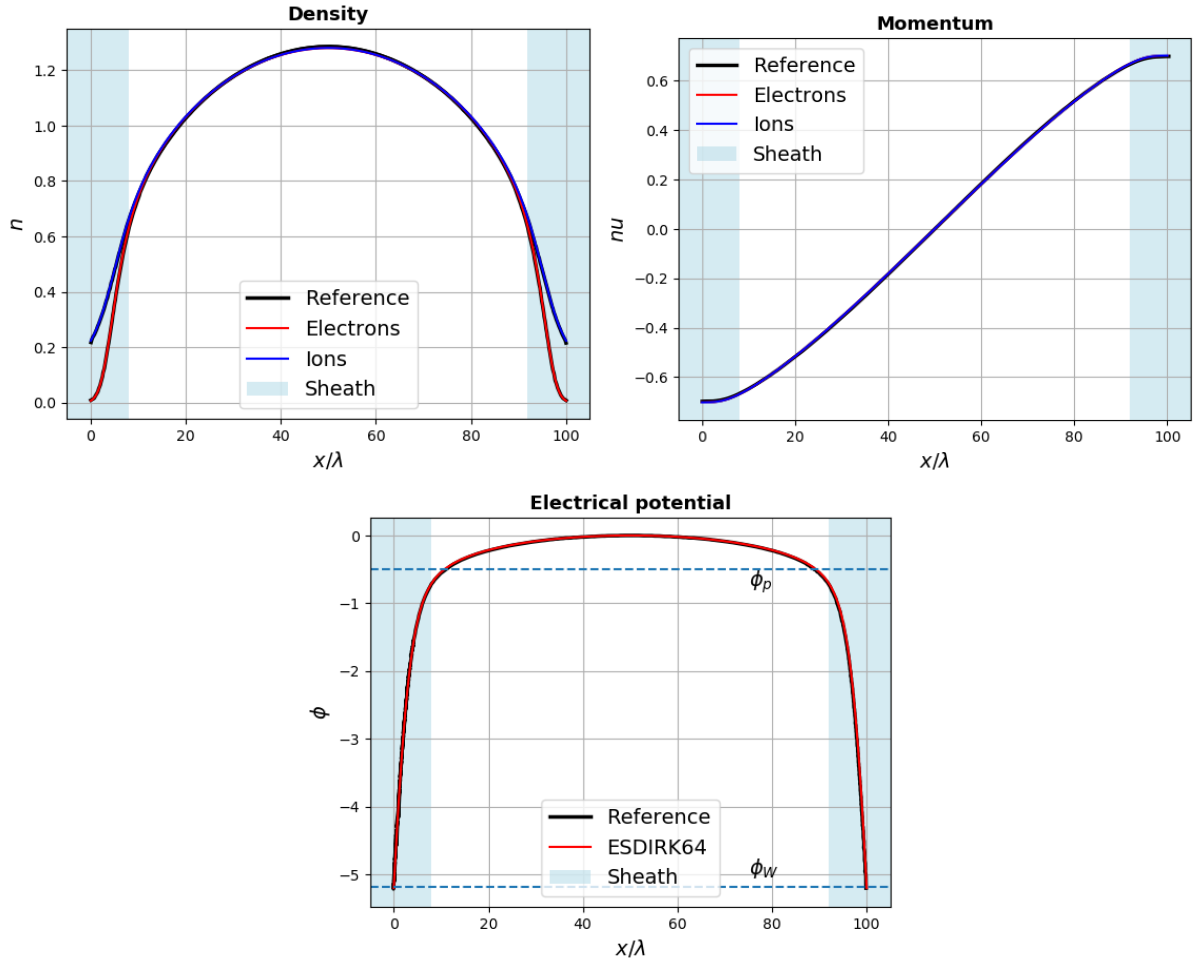

Fig. 8.1: Comparison of the reference and the numerical solution obtained with 100 equally spaced element of order 4 and $\Delta t = 1.5 \times 10^{-5}$sec. The final time is $t = 2$ sec. A steady state is achieved and gives results that are in very good agreement with the reference ones. The potential at the wall ϕ_W derived by Lieberman *et al.*[54] is also very well estimated by the current simulation.

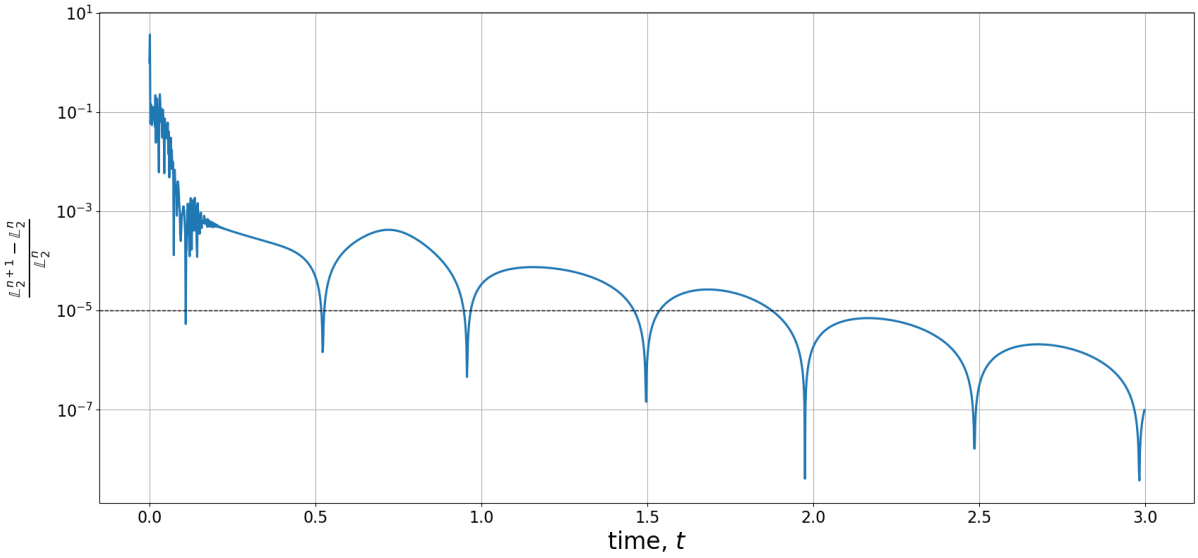

Fig. 8.2: Time evolution of the $\mathbb{L}_2$ norm relative difference described in Eq. (8.4). 100 equally spaced element of order 4 and a time step $\Delta t = 1.5 \times 10^{-5}$ are considered. Following our criterion, a steady state is assessed for simulation time bigger than $t \approx 1.9$ sec.

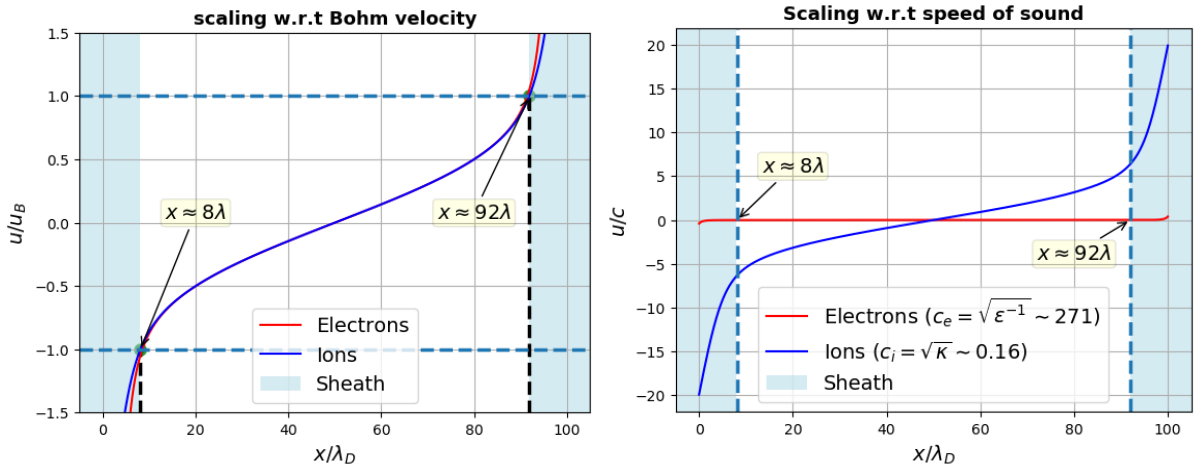

Fig. 8.3: Scaled velocities obtained for a simulation with 100 equally spaced elements of order 4, ESDIRK64 integration and a time step $\Delta t = 1.5 \times 10^{-5}$ sec. These are scaled with respect to the Bohm velocity (left) and the particle speed of sound (right). A normalised sheath thickness of 8 is found after applying the Bohm criterion [8]. In addition, ions are supersonic when entering the sheath, while the electrons are highly subsonic. Ambipolar flow is also achieved in the bulk, meaning that both particles have the same velocity there ("they move together"), while it is not the case in the sheath. The latter justifies the need of the Poisson's equation in this region.

Conclusions and future work

In this work, a numerical model for the simulation of low-temperature collisionless plasma has been developed. The common features of plasma mixture such as the large mass disparity between the electrons and the other particles was introduced. This paved the way for the derivation of the two-fluid model, a system composed of electrons and ions transport equations coupled with a Poisson's equation for the electrical potential.

In the second part of this work, the development of the DG-FEM numerical method has been extensively developed. The numerical aspect of the coupled hyperbolic-elliptic system has been addressed with the implementation of specific strategies: first, a Roe numerical flux corrected with an Harten entropy fix has been proposed for the convective formulation; then, an incomplete internal penalty methods has been developed to treat the diffusive interface flux. And since this diffusive terms only affect the equation for the potential, the penalty terms associated to the particles motions are deactivated. Finally, an extension to the classical formulation of the implicit ESDIRK scheme was provided. Indeed, the inertia terms associates to the potential were deactivated by the introduction of a Boolean parameter β which is equal to 1 for all the parameters excepts for the potential. As a result, this modification of the implicit method permits to treat the Poisson's equation alongside the particles equations during the Newton iterator, enhancing then its convergence. An automatic evaluation of the Jacobian matrix using first order central difference was also described with a specific treatment made onto the linearisation of the ionisation contributions. The dependence over the whole domain for this last parameters may results in a matrix that is full. To avoid that a constant value for the ionisation frequency was assumed at each time step. All of these strategies were implemented in the ForDGe solver, an immersed boundary Cartesian DG-FEM solver developed at the University of Liege.

A preliminary work based on the study of the unidimensional Burgers' equation has been carried out. Although this work has served for the handling of the methods and the ForDGe solver, it has shown the impact of bad entropy conditioning to the solution. As a results, the entropy-consistent flux developed by Ismail & Roe has been applied to higher order resolution.

These methods have been tested on two practical cases: the two-stream periodic perturbation and the sheath problem. It has been shown that the current fully-coupled

implicit DG-FEM solver is able to tackle accurately the physics of low-temperature collionsionless plasma. Besides, the use of implicit solver has demonstrated its increased stability being able to solve the two-stream instability with a time step that is more than two order of magnitude bigger than electron plasma frequency. This overcomes totally one of the most stringent stability constraints for plasma flows.

Despite these very good results, a non-linearity is encountered for longer simulation. To address this phenomena two possible explanations were proposed: the first one came from a possible lack of consistency of the Roe flux at low-mach regime which may introduce unexpected non-linear behaviour [2].The second one concerned the derivation of the analytical solution which lies on linear Fourier simplifications.

Regarding the case of confined plasma, the ForDGe solver allowed us to reach a steady state solution that is in very good agreement with the reference solution, but also gives a well representation of the physics of the sheath. The main drawback of the methods is that classical integration is used to let the solution reach step by step the steady state. This direct approach needs a computational effort that is considerable.

8.3 Future work and perspectives

Regarding the two-stream instabilities, a natural way of future improvement of the method is the implementation of advanced strategies for the evaluation of the Roe numerical flux in the case of low-Mach regime. In this topics, one can refer to the method suggested by Chalons *et al.*[15] which proposes to multiply the stabilisation part of the numerical flux by a function $f(M_e)$ that depends on the electron Mach number. In parallel, Liou [55] has proposed a formulation for $f(M_e)$ that introduce a user defined cut-off parameter. The reader will then choose a value for this parameter that avoid having a null numerical dissipation when the electrons have zero velocity [2]. For more advance strategy, the reader can refer to Boniface [9, 10] which has derived a low-Mach fix specific for the Roe's Riemann flux.

On the other hand, one may develop a steady Newton method for the plasma sheath test case instead of the classical time integration. This would save a lot of computational effort as it will solve directly for the steady state solution. Moreover, since the current implementation has shown quite good results for the fully bounded plasma, the next step would be to move onto the Langmuir probe configuration by removing one of the floating walls. In this situation, one could refer to the work of Guittienne [35] and Merlino [57].

Regarding the plasma solver, despite going to multidimensional computation, a good perspective is the integration of the multi-component formulation of plasma. In the multi-fluid formulation, for a number N of different species, a system composed of $2N+1$ equations is solved. These equations account for the moment transports equations of each species and a closure one for the potential. Conversely, in multi-component formulation, the plasma is seen as a single fluid. This means that the contributions of the different

species are seen as a new term of these equations, keeping the number of equations constant. As a result, this formulation allows the the possibility of simulation of large and very heterogeneous mixtures.

Appendices

Appendix A

Jump and average operators

Following the convention presented in section 4.1.1, one can define the jump operator $[[\cdot]]$ as

$$[[a]] = a^+ \boldsymbol{n}^+ + a^- \boldsymbol{n}^- \tag{A.1}$$

$$[[\boldsymbol{a}]] = \boldsymbol{a}^+ \cdot \boldsymbol{n}^+ + \boldsymbol{a}^- \cdot \boldsymbol{n}^- \tag{A.2}$$

$$[[\boldsymbol{a}]]_\otimes = \boldsymbol{a}^+ \boldsymbol{n}^+ + \boldsymbol{a}^- \boldsymbol{n}^- \tag{A.3}$$

It can be noticed that the jump of a scalar results in a vector, whereas for vectors quantities the jump can be defined as an inner product, resulting in a scalar, and as an outer product resulting in a second order tensor.

In addition, the average operator $\{\{\cdot\}\}$ is defined following

$$\{\{a\}\} = \frac{a^+ + a^-}{2} \tag{A.4}$$

$$\{\{\boldsymbol{a}\}\} = \frac{\boldsymbol{a}^+ + \boldsymbol{a}^-}{2} \tag{A.5}$$

From all these definition, one can prove the following identity

$$[[a\boldsymbol{b}]] = \{\{a\}\}\,[[\boldsymbol{b}]] + [[a]] \cdot \{\{\boldsymbol{b}\}\} \tag{A.6}$$

Appendix B

Explicit Fourth-order Runge-Kutta integrator

In this chapter, the implementation of the explicit fourth-order Runge-Kutta (RK4) methods is provided. As shown in section 5.2, RK integrators are based on the compact formulation of the residual vector $\boldsymbol{R}(\boldsymbol{u})$

$$\partial_t \boldsymbol{u} = \boldsymbol{R}(\boldsymbol{u}) \tag{B.1}$$

Then, the explicit RK4 scheme integrates $\boldsymbol{u}$ from time t_{n-1} to t_n with a time step Δt and N intermediate stages following

$$(u_j)^n = (u_j)^{n-1} + \Delta t \sum_{i=1}^{N} b_i \, \underset{\cdot}{\mathrm{k}}_i \tag{B.2}$$

where

$$k_i = f\left(t_{n-1} + c_i \, \Delta t, y_i\right) \tag{B.3}$$

$$y_i = (u_j)^{n-1} + \Delta t \sum_{s=1}^{N-1} a_{is} \, k_s \tag{B.4}$$

and the values of the coefficients a_{ij}, b_i and c_i are stored in the Butcher tableau $\mathcal{B}$ given in Eq. (5.9). In the case of the RK4 method, one obtains the following Butcher tableau

$$\begin{array}{c|cccc} 0 & & & & \\ 1/2 & 1/2 & & & \\ 1/2 & 0 & 1/2 & & \\ 1 & 0 & 0 & 1 & \\ \hline & 1/6 & 1/3 & 1/3 & 1/6 \end{array} \tag{B.5}$$

so that Eq. (B.2) simplifies to

$$(u_j)^{n+1} = (u_j)^n + \frac{\Delta t}{6}\left[k_1 + 2k_2 + 2k_3 + k_4\right] \tag{B.6}$$

where t_n corresponds to the time at the n^{th} iteration, Δt is the time step, and

$$\begin{cases} k_1 &= f\Big(t_{n-1}\,,\, u_j^{n-1}\Big) \\ k_2 &= f\Big(t_{n-1} + \dfrac{\Delta t}{2}\,,\, u_j^{n-1} + \dfrac{\Delta t}{2} k_1\Big) \\ k_3 &= f\Big(t_{n-1} + \dfrac{\Delta t}{2}\,,\, u_j^{n-1} + \dfrac{\Delta t}{2} k_2\Big) \\ k_4 &= f\Big(t_{n-1} + \Delta t\,,\, u_j^{n-1} + \Delta t k_3)\Big) \end{cases} \tag{B.7}$$

The implementation of the RK4 methods is then very straightforward and is explicit, meaning that it allows a relatively fast resolution of the problem in comparison to implicit RK methods. This method is used as time integrator for the Burgers equations developed in Chapter 6. It is also used in the frame of the two-stream instability test case to procure a comparison of the obtained values when the Poisson's equation is solved or not with the rest of the system.

Appendix C

Two-stream perturbation problem

This part details the derivation of the analytical solution of the two-stream perturbation test case presented in section 7.1 for the validation of the numerical discretisation. The methodology used here is the one developped by Chabert & Braithwaite [14] and reused in the work of Crispel *et al.* [27, 26] and Alvarez Laguna *et al.* [2]. It linearised Eq. (2.1) for small perturbations with the following assumptions

- The background electron pressure gradient is negligible, though the perturbation to the electron thermal energy density plays a key role;
- The background electric field gradients of particle drift speed are negligible, meaning that the perturbation to the electric field E plays a key role;
- The ionisation is negligible.

Then, if one considers an harmonic perturbation $\tilde{\boldsymbol{u}}(x,t)$ to the steady solution $\boldsymbol{u}_0(x)$, the solution is

$$\boldsymbol{u}(x,t) = \boldsymbol{u}_0(x) + \tilde{\boldsymbol{u}}(x) \tag{C.1}$$

such that

$$n_e(x,t) = n_{e0} + \tilde{n}_e \sin\Big(\omega t - kx\Big) \tag{C.2}$$
$$n_i(x,t) = n_{i0} + \tilde{n}_i \sin\Big(\omega t - kx\Big) \tag{C.3}$$
$$u_e(x,) = u_{e0} + \tilde{u}_e \sin\Big(\omega t - kx\Big) \tag{C.4}$$
$$u_i(x,t) = u_{i0} + \tilde{u}_i \sin\Big(\omega t - kx\Big) \tag{C.5}$$
$$E(x,t) = E_0 + \tilde{E} \sin\Big(\omega t - kx\Big) \tag{C.6}$$

where ω is the wave frequency and k is the wave number. The steady values are found from the initial conditions of the problem set up since these values does not vary with time. However, in order to find the amplitudes of the perturbed values, one has to solve the system of equations given in Eq. (7.1) for the perturbed variables.

After linearisation, the equations for the perturbations in collisionless plasma are given by

$$\begin{aligned}
-\mathrm{i}\left(\omega - k\,u_{e0}\right)\,\tilde{n}_e + \mathrm{i}k n_{e0}\tilde{u}_e &= 0\\
-\mathrm{i}\left(\omega - k\,u_{i0}\right)\,\tilde{n}_i + \mathrm{i}k n_{i0}\tilde{u}_i &= 0\\
-\mathrm{i}n_{e0}m_e\left(\omega - k\,u_{e0}\right)\,\tilde{n}_e + \mathrm{i}\mathrm{k_B}T_e k\tilde{n}_e &= -n_{e0}e\tilde{E}\\
-\mathrm{i}n_{i0}m_i\left(\omega - k\,u_{i0}\right)\,\tilde{n}_i + \mathrm{i}\mathrm{k_B}T_i k\tilde{n}_i &= n_{i0}e\tilde{E}\\
\mathrm{i}k\tilde{E} &= \frac{e}{\epsilon_0}\left(\tilde{n}_i - \tilde{n}_e\right)
\end{aligned} \tag{C.7}$$

with $\mathrm{i} = \sqrt{-1}$ being the imaginary unit. The last equation can be solved directly, yielding

$$\tilde{E} = \frac{e}{\mathrm{i}k\epsilon_0}\left(\tilde{n}_i - \tilde{n}_e\right) \Rightarrow \tilde{\phi} = \frac{e}{k^2\epsilon_0}\left(\tilde{n}_e - \tilde{n}_i\right) \tag{C.8}$$

Injecting these results in Eq. (C.7) leads to

$$\begin{aligned}
-\left(\omega - k\,u_{e0}\right)\,\tilde{n}_e + k n_{e0}\tilde{u}_e &= 0\\
-\left(\omega - k\,u_{i0}\right)\,\tilde{n}_i + k n_{i0}\tilde{u}_i &= 0\\
-n_{e0}\left(\omega - k\,u_{e0}\right)\,\tilde{n}_e + k{v_{th,e}}^2\tilde{n}_e &= \frac{{\omega_{pe}}^2}{k}\left(\tilde{n}_i - \tilde{n}_e\right)\\
-n_{i0}\left(\omega - k\,u_{i0}\right)\,\tilde{n}_i + k{v_{th,i}}^2\tilde{n}_i &= -\frac{{\omega_{pi}}^2}{k}\left(\tilde{n}_i - \tilde{n}_e\right)\\
\tilde{\phi} &= \frac{e}{k^2\epsilon_0}\left(\tilde{n}_e - \tilde{n}_i\right)
\end{aligned} \tag{C.9}$$

where

$$v_{th,e} = \sqrt{\frac{\mathrm{k_B}T_e}{m_e}} \qquad \text{and} \qquad v_{th,i} = \sqrt{\frac{\mathrm{k_B}T_i}{m_i}} \tag{C.10}$$

are respectively the thermal velocity of electrons and ions, and

$$\omega_{pe} = \sqrt{\frac{n_{e0}e^2}{\epsilon_0 m_e}} \qquad \text{and} \qquad \omega_{pi} = \sqrt{\frac{n_{i0}e^2}{\epsilon_0 m_i}} \tag{C.11}$$

the electrons and ions plasma frequencies.

At the condition proposed by Alvarez Laguna *et al.* [2] for the case of ions initially at rest, *i.e.*

$$n_{e0} = n_{i0} = n_0, \quad u_{e0} = u_0 = u_B, \quad u_{i0} = 0, \quad v_{th,i} = u_0 \tag{C.12}$$

the non-dimensional version of Eq. (C.7) is then

$$\begin{aligned}
-\left(\omega - k\,u_0\right)\,\tilde{n}_e + k n_0\tilde{u}_e &= 0\\
-\omega\,\tilde{n}_i + k n_0\tilde{u}_i &= 0\\
-n_0\left(\omega - k\,u_0\right)\,\tilde{n}_e + k\frac{{u_0}^2}{\varepsilon}\tilde{n}_e &= \frac{n_0}{k\chi\varepsilon}\left(\tilde{n}_i - \tilde{n}_e\right)\\
-n_0\omega\,\tilde{n}_i + k{u_0}^2\tilde{n}_i &= -\frac{n_0}{k\chi}\left(\tilde{n}_i - \tilde{n}_e\right)\\
\tilde{\phi} &= \frac{\left(\tilde{n}_i - \tilde{n}_e\right)}{k\chi}
\end{aligned} \tag{C.13}$$

with $\varepsilon = \frac{m_e}{m_i}$, $\kappa = \frac{T_i}{T_e}$ and $\chi = $. This system can be written in matrix form like

$$\begin{pmatrix} ku_0 - \omega & 0 & kn_0 & 0 & 0 \\ 0 & -\omega & 0 & kn_0 & 0 \\ \frac{k\chi}{\varepsilon} + \frac{n_0}{\varepsilon k} & -\frac{n_0}{\varepsilon k} & k\chi n_0 u_0 - \chi n_0 \omega & 0 & 0 \\ -\frac{n_0}{k} & k\kappa\chi + \frac{n_0}{k} & 0 & -\chi n_0 \omega & 0 \\ \frac{1}{k\chi} & -\frac{1}{k\chi} & 0 & 0 & 1 \end{pmatrix} \begin{pmatrix} \tilde{n}_e \\ \tilde{n}_i \\ \tilde{u}_e \\ \tilde{u}_i \\ \tilde{\phi} \end{pmatrix} = \mathbf{0} \tag{C.14}$$

To have non zero results, one has to fix one of the values (in this case $\tilde{u}_e \sim c_e = \sqrt{\varepsilon^{-1}}$) and then solve the obtained $\boldsymbol{A}\,\tilde{\boldsymbol{x}} = \boldsymbol{b}$ system.

As a consequence, for the condition presented in section 7.1, *i.e.* $\kappa = 1$, $\varepsilon = 10^{-4}$ and $\chi = 10^4$, the solution to Eq. (C.14) is

$$\begin{cases} \tilde{n}_e = 2.41425 \times 10^{-2} \\ \tilde{n}_i = 2.41425 \times 10^{-2} \\ \tilde{u}_e = 10^{-2} \\ \tilde{u}_i = 3.41425 \times 10^{-2} \\ \tilde{\phi} = 2.41421 \times 10^{-2} \end{cases} \tag{C.15}$$

C.1 Dispersion relation

A dispersion relation in the form of a fourth-order equation $F(k, \omega) = 0$ can be found from Eq. (C.14) when the potential is not considered (*i.e.* without taking its last row and column). It corresponds to the resolution of the characteristics equations $\det(\boldsymbol{A}) = 0$, where

$$\boldsymbol{A} = \begin{pmatrix} ku_0 - \omega & 0 & kn_0 & 0 \\ 0 & -\omega & 0 & kn_0 \\ \frac{k\chi}{\varepsilon} + \frac{n_0}{\varepsilon k} & -\frac{n_0}{\varepsilon k} & k\chi n_0 u_0 - \chi n_0 \omega & 0 \\ -\frac{n_0}{k} & k\kappa\chi + \frac{n_0}{k} & 0 & -\chi n_0 \omega \end{pmatrix} \tag{C.16}$$

so that

$$\begin{aligned} \det(\boldsymbol{A}) = \frac{{n_0}^2}{\varepsilon\chi} \Big[& \varepsilon k u_0 \left(-k n_0 u_0 + 2\omega \left(k^2 \kappa\chi + n_0 \right) \right) \\ & + \varepsilon\chi \left(-k^4 \kappa u_0^2 - 2k\omega^3 u_0 + \omega^4 \right) + k^4 \kappa\chi + k^2 n_0 (\kappa + 1) \\ & + \omega^2 \left(\varepsilon k^2 \chi \left(-\kappa + u_0^2 \right) - \varepsilon n_0 - k^2 \chi n_0 \right) \Big] \end{aligned} \tag{C.17}$$

The characteristic equation $\det(\boldsymbol{A}) = 0$ is then in the form of a fourth-order equation in ω express as

$$F(k, \omega) = \alpha_4 \omega^4 + \alpha_3 \omega^3 + \alpha_2 \omega^2 + \alpha_1 \omega + \alpha_0 = 0 \tag{C.18}$$

where

$$\alpha_4 = \varepsilon\chi, \qquad \alpha_3 = -2\varepsilon\chi k u_0, \qquad \alpha_2 = \left(\varepsilon k^2\chi\left(u_0^2 - \kappa\right) - \varepsilon n_0 - k^2\chi - n_0\right)$$
$$\alpha_1 = 2\left(k^2\kappa\chi + n_0\right)\varepsilon k u_0, \qquad \alpha_0 = -\varepsilon k^2 u_0^2 n_0 - \varepsilon\chi k^4\kappa u_0^2 + k^4\kappa\chi + k^2 n_0\left(\kappa + 1\right). \tag{C.19}$$

Consequently, in order to find a value for ω, one has to solve Eq. (C.18) for a given value of k. In the case of the condition stated in section 7.1, the solutions found are

$$\begin{cases} \omega_0 \approx 10^6 \\ \omega_1 \approx -10^6 \\ \omega_2 = 8.88572689 \\ \omega_3 = -8.88447038 \end{cases} \tag{C.20}$$

which are found real values. Here, the value of $\omega = 8.885726989$ is chosen.

Bibliography

[1] *9-kW MAGNETICALLY-SHIELDED Hall Thruster (H9).* https://pepl.engin.umich.edu/project/9-kw-magnetically-shielded-hall-thruster/ (cit. on p. 1).

[2] A. Alvarez-Laguna et al. "An asymptotic preserving well-balanced scheme for the isothermal fluid equations in low-temperature plasma applications". In: *Journal of Computational Physics* 419 (2020), p. 109634 (cit. on pp. 2, 3, 12, 14–16, 36, 51, 52, 60, 61, 65, 71, 72).

[3] F. Bassi et al. "Investigation of high-order temporal schemes for the discontinuous Galerkin solution of the Navier–Stokes equations". In: *Proceedings of the 11th world congress on computational mechanics, WCCM 2014, 5th European conference on computational mechanics, ECCM 2014 and 6th European conference on computational fluid dynamics, ECFD 2014*. 2014, pp. 5651–5662 (cit. on p. 35).

[4] H. Bateman. "Some recent researches on the motion of fluids". In: *Monthly Weather Review* 43.4 (1915), pp. 163–170 (cit. on p. 42).

[5] E. R. Benton and G. W. Platzman. "A table of solutions of the one-dimensional Burgers equation". In: *Quarterly of Applied Mathematics* 30.2 (1972), pp. 195–212 (cit. on p. 43).

[6] A. Bermudez and M. E. Vazquez. "Upwind methods for hyperbolic conservation laws with source terms". In: *Computers & Fluids* 23.8 (1994), pp. 1049–1071 (cit. on p. 3).

[7] J. Boeuf. "Plasma display panels: physics, recent developments and key issues". In: *Journal of physics D: Applied physics* 36.6 (2003), R53 (cit. on p. 1).

[8] D. Bohm. "The characteristics of electrical discharges in magnetic fields". In: *Qualitative Description of the Arc Plasma in a Magnetic Field* (1949) (cit. on pp. 14, 62, 63).

[9] J.-C. Boniface. "Rescaling of the Roe Scheme in Low Mach-Number Flow Regions". In: *Journal of Computational Physics* 328 (Oct. 2016). DOI: 10.1016/j.jcp.2016.10.011 (cit. on p. 65).

[10] J.-C. Boniface. "Rescaling of the Roe Scheme in Low Mach-Number Flow Regions II: Artificial Speed of Sound and Low Mach Number Fix". In: (2019) (cit. on p. 65).

[11] S. Braginskii. "Transport processes in a plasma". In: *Reviews of plasma physics* 1 (1965), p. 205 (cit. on p. 8).

[12] J. M. Burgers. "A mathematical model illustrating the theory of turbulence". In: *Advances in applied mechanics*. Vol. 1. Elsevier, 1948, pp. 171–199 (cit. on p. 42).

[13] M. H. Carpenter et al. “Entropy stable spectral collocation schemes for the Navier–Stokes equations: Discontinuous interfaces”. In: *SIAM Journal on Scientific Computing* 36.5 (2014), B835–B867 (cit. on p. 45).

[14] P. Chabert and N. Braithwaite. *Physics of radio-frequency plasmas*. Cambridge University Press, 2011 (cit. on pp. 2, 5, 7, 13, 15, 20, 52, 60, 71).

[15] C. Chalons, M. Girardin, and S. Kokh. “An all-regime Lagrange-Projection like scheme for the gas dynamics equations on unstructured meshes”. In: *Communications in Computational Physics* 20.1 (2016), pp. 188–233 (cit. on p. 65).

[16] P. Chandrashekar. “Kinetic energy preserving and entropy stable finite volume schemes for compressible Euler and Navier-Stokes equations”. In: *Communications in Computational Physics* 14.5 (2013), pp. 1252–1286 (cit. on p. 45).

[17] S. Chapman and T. Cowling. “The Mathematical Theory of Nonuniform Gases (Cambridge University Press, Cambridge)”. In: (1970) (cit. on p. 7).

[18] F. F. Chen et al. *Introduction to plasma physics and controlled fusion*. Vol. 1. Springer, 1984 (cit. on pp. 12, 51).

[19] T. Chen and C.-W. Shu. “Entropy stable high order discontinuous Galerkin methods with suitable quadrature rules for hyperbolic conservation laws”. In: *Journal of Computational Physics* 345 (2017), pp. 427–461 (cit. on p. 45).

[20] C. Child. “Discharge from hot CaO”. In: *Physical Review Letters* 32.1 (1911), pp. 492–511 (cit. on p. 14).

[21] B. Cockburn, G. E. Karniadakis, and C.-W. Shu. *Discontinuous Galerkin methods: theory, computation and applications*. Vol. 11. Springer Science & Business Media, 2012 (cit. on pp. 22, 24).

[22] B. Cockburn and C.-W. Shu. “Runge–Kutta discontinuous Galerkin methods for convection-dominated problems”. In: *Journal of scientific computing* 16.3 (2001), pp. 173–261 (cit. on p. 35).

[23] J. D. Cole. “On a quasi-linear parabolic equation occurring in aerodynamics”. In: *Quarterly of applied mathematics* 9.3 (1951), pp. 225–236 (cit. on p. 44).

[24] N. Corthouts et al. *Travail de Fin d’Etudes: Discontinuous Galerkin Finite Element Method Applied to Plasma Flows*. Université de Liège, Liège, Belgique, 2020. https://matheo.uliege.be/handle/2268.2/10171 (cit. on pp. 3, 53).

[25] P. Crispel, P. Degond, and M.-H. Vignal. “An asymptotic preserving scheme for the two-fluid Euler–Poisson model in the quasineutral limit”. In: *Journal of Computational Physics* 223.1 (2007), pp. 208–234 (cit. on pp. 2, 13, 35).

[26] P. Crispel, P. Degond, and M.-H. Vignal. “Quasi-neutral fluid models for current-carrying plasmas”. In: *Journal of Computational Physics* 205.2 (2005), pp. 408–438 (cit. on pp. 2, 12, 51, 71).

[27] P. Crispel et al. “Trois formulations d’un modèle de plasma quasi-neutre avec courant non nul”. In: *Comptes Rendus Mathematique* 338.4 (2004), pp. 327–332 (cit. on pp. 2, 12, 13, 51, 71).

[28] P. Degond. “Asymptotic-preserving schemes for fluid models of plasmas”. In: *arXiv preprint arXiv:1104.1869* (2011) (cit. on pp. 2, 35).

[29] P. Degond, J.-G. Liu, and M.-H. Vignal. “Analysis of an asymptotic preserving scheme for the Euler–Poisson system in the quasineutral limit”. In: *SIAM Journal on Numerical Analysis* 46.3 (2008), pp. 1298–1322 (cit. on pp. 2, 36).

[30] D. A. Di Pietro and A. Ern. *Mathematical aspects of discontinuous Galerkin methods*. Vol. 69. Springer Science & Business Media, 2011 (cit. on p. 24).

[31] A. Fick. “Ueber diffusion”. In: *Annalen der Physik* 170.1 (1855), pp. 59–86 (cit. on p. 45).

[32] U. S. Fjordholm, S. Mishra, and E. Tadmor. “Arbitrarily high-order accurate entropy stable essentially nonoscillatory schemes for systems of conservation laws”. In: *SIAM Journal on Numerical Analysis* 50.2 (2012), pp. 544–573 (cit. on p. 45).

[33] D. Ghosh and J. D. Baeder. “Compact reconstruction schemes with weighted ENO limiting for hyperbolic conservation laws”. In: *SIAM Journal on Scientific Computing* 34.3 (2012), A1678–A1706 (cit. on p. 46).

[34] D. M. Goebel and I. Katz. *Fundamentals of electric propulsion: ion and Hall thrusters*. Vol. 1. John Wiley & Sons, 2008 (cit. on p. 1).

[35] P. Guittienne, A. Howling, and I. Furno. “Two-fluid solutions for Langmuir probes in collisionless and isothermal plasma, over all space and bias potential”. In: *Physics of Plasmas* 25.9 (2018), p. 093519 (cit. on p. 65).

[36] G. Hagelaar. “Modelling methods for low-temperature plasmas”. PhD thesis. Université Toulouse III Paul Sabatier (UT3 Paul Sabatier), 2008 (cit. on p. 14).

[37] K. Hara, I. D. Boyd, and V. I. Kolobov. “One-dimensional hybrid-direct kinetic simulation of the discharge plasma in a Hall thruster”. In: *Physics of Plasmas* 19.11 (2012), p. 113508 (cit. on p. 1).

[38] A. Harten. “High resolution schemes for hyperbolic conservation laws”. In: *Journal of computational physics* 135.2 (1997), pp. 260–278 (cit. on p. 31).

[39] K. Hillewaert. *Development of the discontinuous Galerkin method for high-resolution, large scale CFD and acoustics in industrial geometries*. Presses univ. de Louvain, 2013 (cit. on pp. 22–26, 34).

[40] C. Hirsch. *Numerical computation of internal and external flows: The fundamentals of computational fluid dynamics*. Elsevier, 2007 (cit. on pp. 43, 44).

[41] E. Hopf. “The partial differential equation $u_t + u\,u_x = \mu\,u_{xx}$”. In: *Communications on Pure and Applied mathematics* 3.3 (1950), pp. 201–230 (cit. on pp. 42, 44, 49).

[42] H. Hugoniot. “Mémoire sur la propagation du mouvement dans un fluide indéfini (seconde Partie)”. In: *Journal de Mathématiques Pures et Appliquées* 4 (1888), pp. 153–168 (cit. on p. 44).

[43] F. Ismail and P. L. Roe. “Affordable, entropy-consistent Euler flux functions II: Entropy production at shocks”. In: *Journal of Computational Physics* 228.15 (2009), pp. 5410–5436 (cit. on pp. 45, 47, 48).

[44] S. Jin. “Efficient asymptotic-preserving (AP) schemes for some multiscale kinetic equations”. In: *SIAM Journal on Scientific Computing* 21.2 (1999), pp. 441–454 (cit. on p. 2).

[45] M. Keidar, I. Boyd, and I. Beilis. “Plasma flow and plasma–wall transition in Hall thruster channel”. In: *Physics of Plasmas* 8.12 (2001), pp. 5315–5322 (cit. on p. 1).

[46] M. J. Kushner. “Hybrid modelling of low temperature plasmas for fundamental investigations and equipment design”. In: *Journal of Physics D: Applied Physics* 42.19 (2009), p. 194013 (cit. on p. 1).

[47] A. A. Laguna et al. “A versatile numerical method for the multi-fluid plasma model in partially-and fully-ionized plasmas”. In: *Journal of Physics: Conference Series*. Vol. 1031. 1. IOP publishing. 2018, p. 012015 (cit. on p. 2).

[48] A. A. Laguna et al. “Fully-implicit finite volume method for the ideal two-fluid plasma model”. In: *Computer Physics Communications* 231 (2018), pp. 31–44 (cit. on p. 2).

[49] C. B. Laney. *Computational gasdynamics*. Cambridge university press, 1998 (cit. on pp. 47, 48).

[50] I. Langmuir. “The interaction of electron and positive ion space charges in cathode sheaths”. In: *Physical Review Letters* 33.1 (1929), pp. 954–989 (cit. on p. 14).

[51] M. Laroussi. “Cold Plasma in Medicine and Healthcare: The New Frontier in Low Temperature Plasma Applications”. In: *Frontiers in Physics* 8 (2020), p. 74. ISSN: 2296-424X. DOI: 10.3389/fphy.2020.00074. https://www.frontiersin.org/article/10.3389/fphy.2020.00074 (cit. on p. 1).

[52] R. J. LeVeque and R. J. Leveque. *Numerical methods for conservation laws*. Vol. 132. Springer, 1992 (cit. on p. 29).

[53] R. J. LeVeque and H. C. Yee. “A study of numerical methods for hyperbolic conservation laws with stiff source terms”. In: *Journal of computational physics* 86.1 (1990), pp. 187–210 (cit. on p. 3).

[54] M. A. Lieberman and A. J. Lichtenberg. *Principles of plasma discharges and materials processing*. John Wiley & Sons, 2005 (cit. on pp. 61, 62).

[55] M.-S. Liou. “A sequel to AUSM, Part II: AUSM+-up for all speeds”. In: *Journal of Computational Physics* 214.1 (2006), pp. 137–170. ISSN: 0021-9991. DOI: https://doi.org/10.1016/j.jcp.2005.09.020. https://www.sciencedirect.com/science/article/pii/S0021999105004274 (cit. on p. 65).

[56] J. Loverich, A. Hakim, and U. Shumlak. “A discontinuous Galerkin method for ideal two-fluid plasma equations”. In: *Communications in Computational Physics* 9.2 (2011), pp. 240–268 (cit. on pp. 2, 3).

[57] R. L. Merlino. “Understanding Langmuir probe current-voltage characteristics”. In: *American Journal of Physics* 75.12 (2007), pp. 1078–1085 (cit. on p. 65).

[58] P. Orlandi. “The Burgers equation”. In: *Fluid Flow Phenomena*. Springer, 2000, pp. 40–50 (cit. on p. 42).

[59] M. Pelanti, L. Quartapelle, and L. Vigevano. “A review of entropy fixes as applied to Roe’s linearization”. In: *Teaching material of the Aerospace and Aeronautics Department of Politecnico di Milano* (2001) (cit. on p. 31).

[60] A. Piel. *Plasma physics: an introduction to laboratory, space, and fusion plasmas*. Springer, 2017 (cit. on p. 14).

[61] W. J. M. Rankine. “XV. On the thermodynamic theory of waves of finite longitudinal disturbance”. In: *Philosophical Transactions of the Royal Society of London* 160 (1870), pp. 277–288 (cit. on p. 44).

[62] J. Raphson. *Analysis aequationum universalis: seu ad aequationes algebraicas resolvendas methodus generalis, & expedita, ex nova infinitarum serierum methodo, deducta ac demonstrata*. Vol. 1. Typis TB prostant venales apud A. & I. Churchill, 1702 (cit. on p. 37).

[63] W. H. Reed and T. R. Hill. *Triangular mesh methods for the neutron transport equation*. Tech. rep. Los Alamos Scientific Lab., N. Mex.(USA), 1973 (cit. on p. 22).

[64] K.-U. Riemann. “The Bohm criterion and sheath formation”. In: *Journal of Physics D: Applied Physics* 24.4 (1991), p. 493 (cit. on p. 62).

[65] K. Riemann et al. “The plasma–sheath matching problem”. In: *Plasma physics and controlled fusion* 47.11 (2005), p. 1949 (cit. on pp. 14, 15, 62).

[66] P. L. Roe. “Approximate Riemann solvers, parameter vectors, and difference schemes”. In: *Journal of computational physics* 43.2 (1981), pp. 357–372 (cit. on pp. 29, 30).

[67] A. Samokhin. “Gradient catastrophes and sawtooth solutions for a generalized Burgers equation on an interval”. In: *Journal of Geometry and Physics* 85 (2014), pp. 177–184 (cit. on p. 42).

[68] U. Shumlak and J. Loverich. “Approximate Riemann solver for the two-fluid plasma model”. In: *Journal of Computational Physics* 187.2 (2003), pp. 620–638 (cit. on pp. 2, 3).

[69] U. Shumlak et al. “Advanced physics calculations using a multi-fluid plasma model”. In: *Computer Physics Communications* 182.9 (2011), pp. 1767–1770 (cit. on pp. 2, 3).

[70] E. Turkel. “Preconditioned methods for solving the incompressible and low speed compressible equations”. In: *Journal of computational physics* 72.2 (1987), pp. 277–298 (cit. on p. 2).

[71] V. Vatsa. “Time Integration Schemes for the Unsteady Navier-Stokes Equations”. In: *AIAA Paper* 2612 (2001) (cit. on pp. 36, 37).

[72] H. Q. Yang and A. Przekwas. “A comparative study of advanced shock-capturing shcemes applied to Burgers’ equation”. In: *Journal of Computational Physics* 102 (1992), pp. 139–159 (cit. on p. 46).